

MICROCOPY RESOLUTION TEST CHART
NATIONAL BUREAU OF STANDARDS-1963-A

2

AD-A184 663

NAVAL POSTGRADUATE SCHOOL Monterey, California



DTIC
ELECTE
SEP 24 1987
S D

THESIS

SURFACE POLARITON RESONANCES
AND REFLECTANCE ON A BIGRATING

by

John Gary Melendez

June 1987

Thesis Advisor: Nathaniel E. Glass

Approved for public release; distribution is unlimited.

AD 4124 632

REPORT DOCUMENTATION PAGE

1a REPORT SECURITY CLASSIFICATION UNCLASSIFIED		1b RESTRICTIVE MARKINGS	
2a SECURITY CLASSIFICATION AUTHORITY		3 DISTRIBUTION/AVAILABILITY OF REPORT Approved for public release; distribution is unlimited.	
2b DECLASSIFICATION/DOWNGRADING SCHEDULE		5 MONITORING ORGANIZATION REPORT NUMBER(S)	
4 PERFORMING ORGANIZATION REPORT NUMBER(S)		7a NAME OF MONITORING ORGANIZATION Naval Postgraduate School	
6a NAME OF PERFORMING ORGANIZATION Naval Postgraduate School	6b OFFICE SYMBOL (If applicable) 61	7b ADDRESS (City, State, and ZIP Code) Monterey, California 93943-5000	
6c ADDRESS (City, State, and ZIP Code) Monterey, California 93943-5000		9 PROCUREMENT INSTRUMENT IDENTIFICATION NUMBER	
8a NAME OF FUNDING/SPONSORING ORGANIZATION	8b OFFICE SYMBOL (If applicable)	10 SOURCE OF FUNDING NUMBERS	
8c ADDRESS (City, State, and ZIP Code)		PROGRAM ELEMENT NO	PROJECT NO
		TASK NO	WORK UNIT ACCESSION NO
11 TITLE (Include Security Classification) SURFACE POLARITON RESONANCES AND REFLECTANCE ON A BIGRATING			
12 PERSONAL AUTHOR(S) Melendez, J. Gary			
13a TYPE OF REPORT Master's Thesis	13b TIME COVERED FROM _____ TO _____	14 DATE OF REPORT (Year, Month, Day) 1987 June	15 PAGE COUNT 128
16 SUPPLEMENTARY NOTATION			
17 COSATI CODES		18 SUBJECT TERMS (Continue on reverse if necessary and identify by block number)	
FIELD	GROUP	Surface Polaritons, Plasmon-Polaritons, Diffraction Grating, Reflectance, Enhancement	
19 ABSTRACT (Continue on reverse if necessary and identify by block number)			
<p>A first order perturbation theory for treatment of the diffraction of light with surface polariton resonances on a bigrating has previously been developed and implemented. A modification has since been developed to include simultaneous resonant coupling to four surface polaritons. This work implements the modification and compares the results against exact theory.</p> <p>Results for reflectance versus angle of incidence were obtained for a sinusoidal bigrating of silver with a period of 615.47 nm and an incident wavelength of 633.00 nm. The perturbation theory is found to be valid at off-normal incidence for grating height to period ratios of 0.024 and less. For the geometry investigated, second order effects strongly influence the reflectance versus incidence angle near normal</p> <p style="text-align: right;">(cont'd)</p>			
20 DISTRIBUTION/AVAILABILITY OF ABSTRACT <input checked="" type="checkbox"/> UNCLASSIFIED/UNLIMITED <input type="checkbox"/> SAME AS RPT <input type="checkbox"/> DTIC USERS		21 ABSTRACT SECURITY CLASSIFICATION UNCLASSIFIED	
22a NAME OF RESPONSIBLE INDIVIDUAL Nathaniel E. Glass		22b TELEPHONE (Include Area Code) (408) 646-3227	22c OFFICE SYMBOL 61Gc

Block 19. (cont'd)

incidence, and the perturbation theory thus has only limited usefulness. Results for reflectance versus incident frequency at normal incidence, however, are reliably predicted by the perturbation theory.



Accession For	
NTIS CRA&I	<input checked="" type="checkbox"/>
DTIC TAB	<input type="checkbox"/>
Unannounced	<input type="checkbox"/>
Justification	
By	
Distribution/	
Availability Codes	
Dist	Avail and/or Special
A-1	

Approved for public release; distribution is unlimited.

Surface Polariton Resonances and
Reflectance on a Bigrating

by

John Gary Melendez
Lieutenant, United States Navy
B.S., University of Alabama in Birmingham, 1978

Submitted in partial fulfillment of the
requirements for the degree of

MASTER OF SCIENCE IN PHYSICS

from the


NAVAL POSTGRADUATE SCHOOL
June 1987

Author:




John Gary Melendez

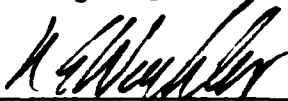
Approved by:




Nathaniel E. Glass, Thesis Advisor



John R. Neighbors, Second Reader



Karlheinz E. Woehler, Chairman,
Department of Physics



Gordon E. Schacher, Dean of Science and
Engineering

ABSTRACT

A first order perturbation theory for treatment of the diffraction of light with surface polariton resonances on a bigrating has previously been developed and implemented. A modification has since been developed to include simultaneous resonant coupling to four surface polaritons. This work implements the modification and compares the results against exact theory.

Results for reflectance versus angle of incidence were obtained for a sinusoidal bigrating of silver with a period of 615.47 nm and an incident wavelength of 633.00 nm. The perturbation theory is found to be valid at off-normal incidence for grating height to period ratios of 0.024 and less. For the geometry investigated, second order effects strongly influence the reflectance versus incidence angle near normal incidence, and the perturbation theory thus has only limited usefulness. Results for reflectance versus incident frequency at normal incidence, however, are reliably predicted by the perturbation theory.

TABLE OF CONTENTS

I.	INTRODUCTION	13
	A. BACKGROUND	13
	B. PROBLEM STATEMENT	17
II.	THEORY	20
	A. MECHANISMS	20
	B. ANALYTICAL METHODS	21
	1. Exact Theory	22
	2. Perturbation Theory	30
III.	NUMERICAL IMPLEMENTATION	38
	A. QUANTITIES AND GEOMETRY INVESTIGATED	38
	B. EXACT THEORY IMPLEMENTATION	40
	C. PERTURBATION THEORY IMPLEMENTATION	43
	D. SELECTION OF PARAMETERS	44
IV.	VALIDATION AT OFF-NORMAL INCIDENCE	47
	A. RESULTS AT OFF-NORMAL INCIDENCE	48
	B. CONVERGENCE OF EXACT THEORY CALCULATIONS	65
V.	VALIDATION NEAR NORMAL INCIDENCE	68
	A. RESULTS NEAR NORMAL INCIDENCE VERSUS ANGLE OF INCIDENCE	68
	B. RESULTS AT NORMAL INCIDENCE VERSUS FREQUENCY	89
	C. CONVERGENCE OF EXACT THEORY CALCULATIONS	93

VI. CONCLUSIONS AND RECOMMENDATIONS	96
APPENDIX A: DEFINITIONS OF PERTURBATION MATRIX ELEMENTS	101
APPENDIX B: ENHANCEMENT CURVES FOR CASES INVESTIGATED	104
LIST OF REFERENCES	124
INITIAL DISTRIBUTION LIST	127

LIST OF TABLES

1.	PERCENTAGE DIFFERENCES OF EXACT AND PERTURBATION RESULTS FOR $\phi = 5^\circ$ AZIMUTH	57
2.	PERCENTAGE DIFFERENCES OF EXACT AND PERTURBATION RESULTS FOR $\phi = 25^\circ$ AZIMUTH	61
3.	SUMMARY OF CONVERGENCE CHECK RESULTS FOR REFLECTANCES AT OFF-NORMAL INCIDENCE	66
4.	SUMMARY OF CONVERGENCE CHECK RESULTS FOR ENHANCEMENTS AT OFF-NORMAL INCIDENCE	67
5.	PERCENTAGE DIFFERENCES OF EXACT AND PERTURBATION RESULTS FOR $h_1 = 7.4$ nm NEAR NORMAL INCIDENCE	70
6.	PERCENTAGE DIFFERENCES OF EXACT AND PERTURBATION RESULTS FOR CROSS TERM RUNS AT $\phi = 0^\circ$ AZIMUTH	89
7.	PERCENTAGE DIFFERENCES OF EXACT AND PERTURBATION RESULTS VERSUS INCIDENT PHOTON ENERGY	90
8.	SUMMARY OF CONVERGENCE CHECK RESULTS FOR REFLECTANCES NEAR NORMAL INCIDENCE	94
9.	SUMMARY OF CONVERGENCE CHECK RESULTS FOR ENHANCEMENTS NEAR NORMAL INCIDENCE	95

LIST OF FIGURES

1.	Schematic of Bigrating and Incidence Geometry	23
2.	Schematic of Wavevector Coupling	34
3.	Reflectance Curves for 5° Azimuth with h_1 at 2.5 nm	50
4.	Reflectance Curves for 5° Azimuth with h_1 at 3.7 nm	51
5.	Reflectance Curves for S Polarized Light at 5° Azimuth and h_1 at 7.4 nm	52
6.	Reflectance Curves for 5° Azimuth with h_1 at 14.8 nm	53
7.	Reflectance Curves for P Polarized Light at 5° Azimuth and h_1 at 7.4 nm	54
8.	Schematic of Wavevector Coupling at 5° Azimuth	59
9.	Reflectance Curves for S Polarized Light at 25° Azimuth and h_1 at 7.4 nm	62
10.	Reflectance Curves for P Polarized Light at 25° Azimuth and h_1 at 7.4 nm	63
11.	Schematic of Wavevector Coupling at 25° Azimuth	64
12.	Reflectance Curves for $h_1 = 7.4$ nm Near Normal Incidence with 0° Azimuth and S Polarization	71
13.	Reflectance Curves for $h_1 = 7.4$ nm Near Normal Incidence with 0° Azimuth and P Polarization	72

14.	Reflectance Curves for $h_1 = 7.4$ nm Near Normal Incidence with 90° Azimuth and S Polarization	73
15.	Reflectance Curves for $h_1 = 7.4$ nm Near Normal Incidence with 90° Azimuth and P Polarization	74
16.	Schematic of Wavevector Coupling for S Polarization Near Normal Incidence	76
17.	Schematic of Wavevector Coupling for P Polarization Near Normal Incidence	78
18.	Reflectance Curves for $h_1 = 6.0$ nm and $h_{11} = 2.5$ nm with S Polarization	83
19.	Reflectance Curves for $h_1 = 6.0$ nm and $h_{11} = 2.5$ nm with P Polarization	84
20.	Reflectance Curves for $h_1 = 4.5$ nm and $h_{11} = 2.5$ nm with S Polarization	85
21.	Reflectance Curves for $h_1 = 4.5$ nm and $h_{11} = 2.5$ nm with P Polarization	86
22.	Reflectance Curves for $h_1 = 4.5$ nm and $h_{11} = 0$ nm with S Polarization	87
23.	Reflectance Curves for $h_1 = 4.5$ nm and $h_{11} = 0$ nm with P Polarization	88
24.	Reflectance Curves Versus Incident Photon Energy for S Polarization	91
25.	Reflectance Curves Versus Incident Photon Energy for P Polarization	92
26.	Reflectance Curve Comparisons for S and P Polarizations Versus Angle of Incidence	98
27.	Reflectance Curve Comparisons for S and P Polarizations Versus Incident Photon Energy	99

28.	Enhancement Curves for 5° Azimuth with h_1 at 2.5 nm	105
29.	Enhancement Curves for 5° Azimuth with h_1 at 3.7 nm	106
30.	Enhancement Curves for S Polarized Light at 5° Azimuth and h_1 at 7.4 nm	107
31.	Enhancement Curves for 5° Azimuth with h_1 at 14.8 nm	108
32.	Enhancement Curves for P Polarized Light at 5° Azimuth and h_1 at 7.4 nm	109
33.	Enhancement Curves for S Polarized Light at 25° Azimuth and h_1 at 7.4 nm	110
34.	Enhancement Curves for P Polarized Light at 25° Azimuth and h_1 at 7.4 nm	111
35.	Enhancement Curves for $h_1 = 7.4$ nm Near Normal Incidence with 0° Azimuth and S Polarization	112
36.	Enhancement Curves for $h_1 = 7.4$ nm Near Normal Incidence with 0° Azimuth and P Polarization	113
37.	Enhancement Curves for $h_1 = 7.4$ nm Near Normal Incidence with 90° Azimuth and S Polarization	114
38.	Enhancement Curves for $h_1 = 7.4$ nm Near Normal Incidence with 90° Azimuth and P Polarization	115
39.	Enhancement Curves for $h_1 = 6.0$ nm and $h_{11} = 2.5$ nm with S Polarization	116
40.	Enhancement Curves for $h_1 = 6.0$ nm and $h_{11} = 2.5$ nm with P Polarization	117

41.	Enhancement Curves for $h_1 = 4.5$ nm and $h_{11} = 2.5$ nm with S Polarization	118
42.	Enhancement Curves for $h_1 = 4.5$ nm and $h_{11} = 2.5$ nm with P Polarization	119
43.	Enhancement Curves for $h_1 = 4.5$ nm and $h_{11} = 0$ nm with S Polarization	120
44.	Enhancement Curves for $h_1 = 4.5$ nm and $h_{11} = 0$ nm with P Polarization	121
45.	Enhancement Curves Versus Incident Photon Energy for S Polarization	122
46.	Enhancement Curves Versus Incident Photon Energy for P Polarization.	123

ACKNOWLEDGEMENT

The author wishes to express his appreciation to Professor Nathaniel E. Glass for his ability to share his considerable store of knowledge without undue mystery, for his willingness to do so and, above all, for his herculean patience in guiding me through this labyrinthine subject matter.

I. INTRODUCTION

A. BACKGROUND

Interest in the enhanced absorption of light by a rough metallic surface can be traced back to 1902 when Wood first noted abrupt losses of approximately 90% in the intensity of light reflected from a metallic grating for a narrow band of frequencies at a given angle of incidence [Ref. 1:p. 661]. These reflectance 'dips' were unexplained by contemporary theories and came to be known as Wood's anomalies. In his paper to the Journal of the Optical Society of America in 1941 [Ref. 2], Fano first postulated the theory that the loss in the energy of the beam during reflection was due to the generation of what he termed "polarized quasi-stationary waves" which propagated along the surface of the metal. In 1976 Maystre and Petit presented theoretical arguments that total absorption of the incident electromagnetic energy was possible with metallic gratings [Ref. 3]. Hutley and Maystre presented experimental evidence of such total absorption later that same year [Ref. 4].

Concurrent with the more recent work in the absorption of electromagnetic energy by metallic gratings, there has been a great deal of interest and investigation of surface electromagnetic enhancement phenomena such as surface enhanced Raman scattering and enhanced second harmonic

generation [Ref. 5:p. 1240; Ref. 6:pp. 366-367]. Electric field enhancements on the order of 10^2 have been noted in the literature [Ref. 5:pp. 1244-1247]. The increases in field enhancement occur under the same conditions as the increases in absorption for metallic gratings [Ref. 5:p. 1241].

This phenomenon of energy absorption and electromagnetic field enhancement is due mainly to the coupling of the incident electromagnetic waves into surface electromagnetic waves in the electron plasma of the metal in the form of surface plasmon polaritons propagating parallel to the interface of the media [Ref. 1:p. 683; Ref. 6:pp. 362-368]. A surface electromagnetic wave is characterized by the exponential decay of its associated fields in the directions normal to the surface of the medium. Since the electron plasma on the surface of a metal constitutes a polarizable medium against the background of the lattice ions, an electromagnetic wave incident on the surface will induce a polarization in the medium and will in turn be modified by the polarization¹. In such a medium, this coupled excitation mode is termed a surface plasmon polariton [Ref. 7:p. 1]. Under certain conditions of grating surface profile and incident frequency and polarization geometry,

¹The details of this mechanism and the role played by the grating in causing resonance coupling are explained more fully in the following chapter on theory.

the coupling is resonant and a significant fraction of the incident energy is transferred to surface plasmon polaritons. This interpretation of the electromagnetic interactions at the grating surface has much theoretical and experimental support [Ref. 8:pp. 69-73].

Besides its obvious use in surface science in the study of surface electromagnetic interactions, the capability of the grating to couple an incident bulk light wave into a surface wave has given rise to a host of practical applications [Ref. 8:pp. 74-75]. Grating couplers can be used to couple a light wave into a surface wave or a guided wave in electro-optical devices. The dependence of the resonant coupling condition on the frequency of the incident light and on the periodicity of the grating corrugations also make grating couplers useful elements in filters and reflectors for solid state lasers and other integrated optics applications. These couplers can couple a laser beam into and out of an optical waveguide (as a guided wave) [Ref. 1:pp. 701-702]. This capability could conceivably be exploited for high efficiency coupling in optical communications systems, some of which are presently under development for use as military communications systems. The enhancement effects available with gratings find application in surface catalysis in electrochemistry, in advanced dielectric breakdown due to surface roughness in high energy lasers, and in the production of radiation from a

non-relativistic charged particle beam interacting with a surface grating [Ref. 8:pp. 72-73; Ref. 9:p. 3; Ref. 10; Ref. 11].

Until the middle 1970's investigations in this area focused almost exclusively on classical gratings, i.e. gratings with periodic corrugations along a single dimension. The most significant absorption and enhancement effects have been observed using gratings of highly conducting materials such as gold, silver and copper with periods on the order of the incident wavelength and corrugation depths on the order of one to fifty nanometers [Ref. 8:pp. 88-89]. These effects are highly dependent on the orientation of the incident electromagnetic field. For total absorption in classical metallic gratings, it is necessary for the plane of incidence to be perpendicular to the grating corrugations and for the incident wave to be linearly polarized with the magnetic field vector transverse to the plane of incidence.

The dependence of the grating coupler efficiency upon the polarization and orientation of the incident light can theoretically be reduced through the use of bigratings, i.e. gratings with periodic corrugations along both surface dimensions [Ref 9:p. 2]. Within the last decade there has been a significant amount of theoretical work with bigratings [Ref. 12:pp. 227, 275-276, 279]. In comparison to that accomplished for classical gratings, experimental

investigations of absorption and enhancement using bigratings is as yet somewhat scarce.

Although the degree of coupling is generally very sensitive to the angle of incidence, even in bigratings, the restriction on the incident polarization would effectively be removed. The use of bigratings, then, would allow many applications to be pursued in which the requirement for linear polarization would be impractical, such as the absorption and storage of sunlight as an energy source [Ref. 9:p. 2].

B. PROBLEM STATEMENT

Analysis of electromagnetic interactions at the interface of a grating with an air or vacuum medium is extremely complicated due to the geometry of the grating. The analysis is performed for the purpose of investigating surface excitations and for designing gratings. The approaches taken to perform the analysis nonperturbatively have taken two basic forms, differential and integral [Ref. 13:pp. 15-40]. Both use the complex dielectric function as a frequency dependent quantity allowing extension of the theory to any dielectric medium. The differential approaches numerically integrate Maxwell's equations across the grating surface boundary. The integral approaches use the Rayleigh method or Green's theorem.

The one common factor in all of these approaches is that, though they give results which accurately conform to the observed experimental results, they are extremely lengthy and can only be accomplished through the use of considerable amounts of computer resources [Ref. 9:pp. 3-4]. The nonperturbative analysis of the bigrating is even more complex than for the classical grating due to the added dimension of the boundary conditions. For this reason several schemes have been proposed for perturbative analysis of the interface problem for a classical grating to provide more readily realizable results. Among these are the methods developed by Kröger and Kretschmann [Ref. 14], Toigo *et al.* [Ref. 15], Mills [Ref. 16], Elson and Sung [Ref. 17], and Glass, Weber and Mills [Ref. 18].

The perturbative technique advanced by Glass, Weber and Mills used an approximation to first order in the surface profile amplitude. The perturbation results for the dispersion curve were compared favorably to that obtained using an integral method of nonperturbative analysis employed by Toigo *et al.* Glass, Maradudin and Celli extended the nonperturbative analysis method for application to bigratings [Ref. 5]. Glass and Maradudin [Ref. 19] compared results from this nonperturbative technique to the experimental results of Inagaki *et al.* [Ref. 20] for total absorption on a bigrating with favorable conclusions. Glass [Ref. 21] modified and extended the perturbation technique

of Glass, Weber and Mills for use with a bigrating, allowing for arbitrary polarization, plane of incidence, and simultaneous stimulation of two surface polaritons propagating in non-collinear directions. The results from this perturbation theory for reflectance and enhancement versus angle of incidence were compared with results from the nonperturbative analysis technique of Glass, Maradudin, and Celli for bigratings. The results compared favorably within the limits of the approximations upon which the theory was based².

Glass further modified his perturbation technique to allow for the simultaneous excitation of four surface polaritons and to increase its facility in treating cases of normal incidence on a bigrating [Ref. 9]. The generalization also allows for determination of the complex dispersion relation for surface polaritons in cases where there may be wavevectors at the intersection of two Brillouin zone boundaries. The implementation of the latest perturbation theory advanced by Glass and comparison with results from the nonperturbative analysis technique of Glass, Maradudin and Celli is the present concern.

²The approximations and their limits are discussed in more detail in the following chapter on theory.

II. THEORY

A. MECHANISMS

The conduction electrons near the surface of a good conductor, such as silver or gold, may be considered as a plasma of nearly free electrons [Ref. 22:pp. 160-161]. Wave-like longitudinal oscillations in the charge density of the electron gas exist as normal modes of the classical system or as elementary excitations in the quantum mechanical system [Ref. 22:pp. 260-262; Ref. 23:pp. 200-202]. Such quanta, consisting of a coupled longitudinal charge oscillation and electric wave, are termed bulk plasmons, or simply plasmons. When localized to a surface, as an evanescent wave, the charge density oscillation, with its accompanying macroscopic polarization and electromagnetic wave, has a component transverse to the direction of propagation (and hence, transverse to the surface). Such a surface electromagnetic wave coupled to collective oscillations of the conduction electrons is called a surface plasmon polariton. Henceforth, the use of the term surface polariton will be understood to mean surface plasmon polariton.

Surface electromagnetic waves may be stimulated by incident electromagnetic radiation in the form of a bulk light wave only in the presence of a grating. Consideration

here is restricted to the case of a linearly polarized incident light wave. The periodicity of the grating surface profile defines a reciprocal lattice [Ref. 21:p 2648]. As a consequence of the Bloch theorem, a grating reciprocal lattice vector may add to the component of the incident wavevector parallel to the surface to equal the wavevector of the evanescent wave at a given frequency [Ref. 22:pp. 163-164; Ref. 24:pp. 2-26; Ref. 5:p. 1241]. The resonance condition is achieved when the frequency of the evanescent wave and that of the incident light wave are equal. The amount of energy transferred to the surface polariton through this coupling can reach significant proportions.

B. ANALYTICAL METHODS

Since the wavelength of the surface polariton in the optical region is much greater than the Fermi wavelength for the materials of interest, the surface waves may be treated by classical, macroscopic, electromagnetic theory.

The term exact theory will be used henceforth in lieu of the term nonperturbative analysis. The development and the equations used in both the exact theory and in the perturbation theory are taken directly from the paper by Glass, Maradudin, and Celli [Ref. 5] and, to a greater extent, from the paper [Ref. 21] and the technical report [Ref. 9] by Glass. The exact theory is well summarized in Maradudin's review article [Ref. 25:pp. 423-469]. Although

the developments in both of the following subsections (II.B.1. and II.B.2.) should be taken as summaries of the analyses given in these papers, the references will not be explicitly cited within the subsections to avoid excessive repetition.

The overwhelming majority of the literature in this area employs the Gaussian, or CGS, system of units. This convention will be adhered to for uniformity and comparison.

1. Exact Theory

A schematic representation of the physical geometry is shown in Figure 1. The coordinate system, shown elevated in the figure for clarity, is located with the $x_3 = 0$ plane as the average position of the surface in the vertical direction. The x_1 and x_2 axes are coincident with the orthogonal dimensions of periodicity of the bigrating surface. The surface profile is defined by

$$x_3 = \zeta(\vec{x}_{\parallel}) \quad \text{where} \quad \vec{x}_{\parallel} \equiv x_1 \hat{x}_1 + x_2 \hat{x}_2 .$$

The region above the bigrating, $x_3 > \zeta(\vec{x}_{\parallel})$, is a vacuum and the region $x_3 < \zeta(\vec{x}_{\parallel})$ is the dielectric characterized by the frequency dependent complex dielectric function

$$\epsilon(\omega) = \epsilon_R(\omega) + i \epsilon_I(\omega).$$

The periodicity of the bigrating is described by the lattice vectors $\vec{a}_1 = a_1 \hat{x}_1$ and $\vec{a}_2 = a_2 \hat{x}_2$ where a_1 and a_2 are the periods of the grating corrugations along each of the two surface dimensions. The surface profile function is periodic in two directions and one may therefore write

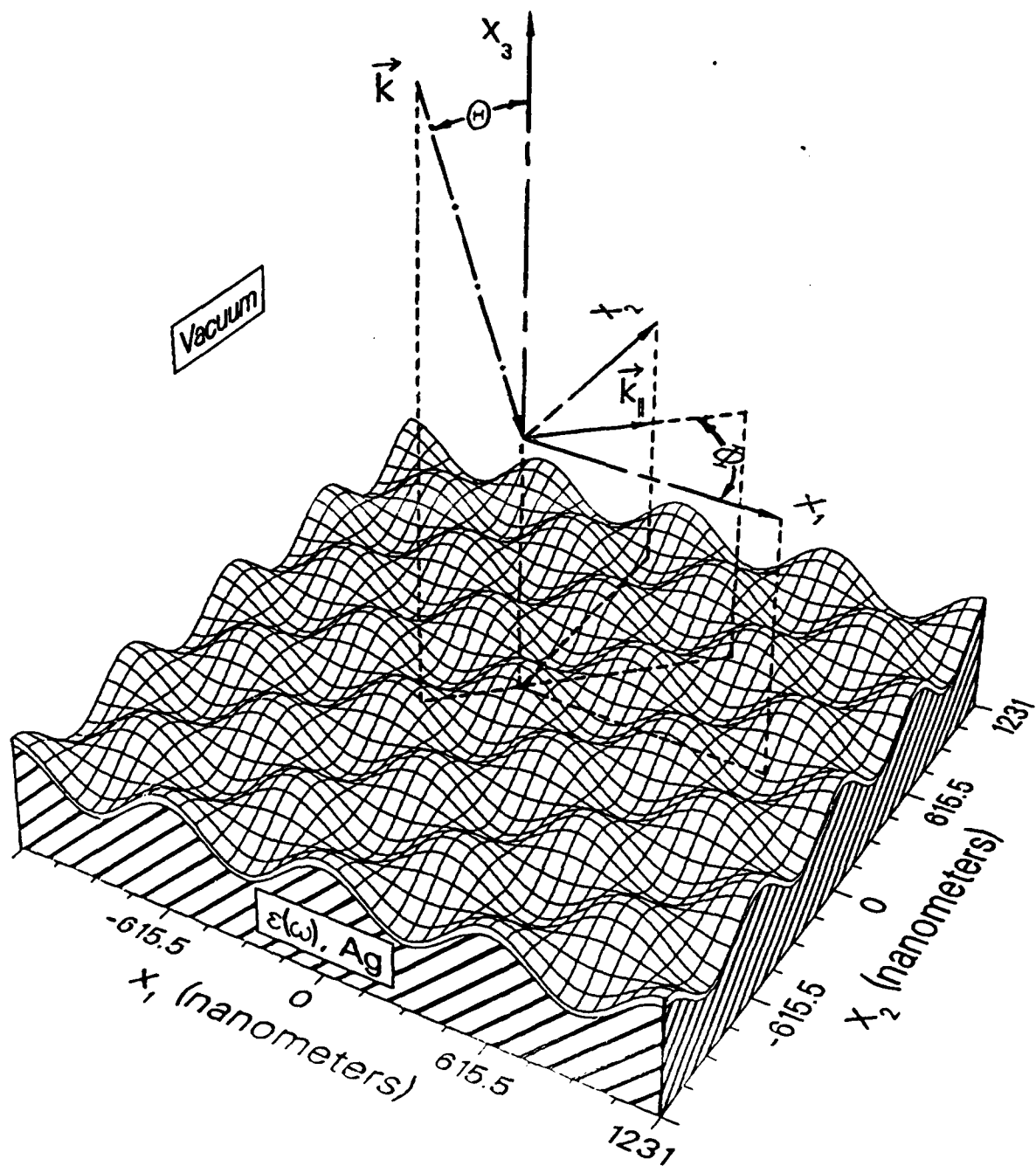


Figure 1. Schematic of Bigrating and Incidence Geometry.

$$\zeta(\vec{x}_{\parallel}) = \zeta(\vec{x}_{\parallel} + n \vec{a}_1 + m \vec{a}_2),$$

where n and m are integers. The restriction to the specific case of the square bigrating, where $a_1 = a_2 = a$, will be imposed later.

Light of angular frequency ω is incident on the bigrating from the vacuum with wavevector \vec{k} at an angle θ from the normal. The plane of incidence is rotated from the axis x_1 by the azimuthal angle ϕ and contains the unit normal \hat{x}_3 . The projection of the incident wavevector \vec{k} onto the $x_3 = 0$ plane is given by

$$\vec{k}_{\parallel} = \frac{\omega}{c} [\sin\theta \cos\phi \hat{x}_1 + \sin\theta \sin\phi \hat{x}_2], \quad (1)$$

since $|\vec{k}| = \frac{\omega}{c}$.

It is convenient at this point to define some terms for use in describing the polarization of the incident electromagnetic wave, in referring to specific regions in the area of the grating surface, and in characterizing the grating surface. The case of the linearly polarized incident wave with the electric field vector perpendicular or transverse to the plane of incidence (TE) will be denoted by the term *s* polarized. The case of the linearly polarized incident wave with the magnetic field vector transverse to the plane of incidence (TM) will be denoted by the term *p* polarized. The ratio of the maximum height of the surface profile above the $x_3 = 0$ plane, ζ_{\max} , to the period of the grating corrugations, a , (in either direction for the

square bigrating) is defined as the corrugation strength of the grating. The region between the maximum and minimum heights of the surface profile, $\zeta_{\min} \leq x_3 \leq \zeta_{\max}$, where $\zeta_{\min} = -\zeta_{\max}$, is termed the selvedge region.

The cornerstone of the analysis is the use of the Rayleigh hypothesis. The assumption here is that expressions for the fields that are valid above the selvedge region in the vacuum and those that are valid below the selvedge region in the dielectric medium may be extended into the surface itself. This assumption places a limitation on the validity of the analysis and this limitation applies to the perturbative analysis as well. If the corrugation strength becomes large enough, field components backscattered from the sides of the corrugations down into the corrugation troughs become significant and the analysis breaks down. As noted by Glass, Maradudin and Celli, however, the hypothesis has been shown to be valid outside its normal limits for periodic surface profiles which are analytic.

In the Rayleigh method, an exact expression is written for the electric field above the selvedge region which satisfies Maxwell's equations in the vacuum and satisfies the Bloch condition for the doubly periodic geometry of the bigrating. This expression is written as a Rayleigh expansion in terms of the incident and scattered fields. Through the use of the vectorial equivalent of the

Kirchoff Integral for diffraction, coupled with the extinction theorem, the expression for the field in the dielectric medium below the selvedge region is eliminated by rewriting it in terms of that above the selvedge region. This halves the number of unknowns in the problem and is termed the reduced Rayleigh method. The boundary conditions associated with Maxwell's equations are then applied at the interface using the expression for the fields above the selvedge region, which is an implicit application of the Rayleigh hypothesis. The results are two sets of linear algebraic equations, of infinite extent, with the Rayleigh coefficients as the unknowns. The Rayleigh coefficients determine the magnitudes of the scattered field components for both the diffracted waves and the evanescent waves.

To solve these equations numerically, the matrices must of course be truncated to some degree. The procedure in the calculations is to truncate the equations to a given finite dimension and solve them numerically. The equations are then truncated to some larger finite dimension and the numerical solution is repeated. Iterations of this procedure are carried out until convergence of results is either confirmed, in which case the validity of the Rayleigh hypothesis for the particular case being investigated is taken to be established, or until divergence becomes apparent. In the latter instance some other analysis technique must be attempted in order to investigate the case

of interest. For cases where convergence is apparent, a suitable dimension for the matrix equations is chosen dependent upon the degree of accuracy required.

The quantitative analysis is initiated by writing the electric field in the vacuum above the selvedge region in the form.

$$\vec{E}(\omega, \vec{x}) = \vec{E}^i(\omega, \vec{k}_{\parallel}) \exp[i\vec{k}_{\parallel} \cdot \vec{x}_{\parallel} - i\alpha_0(\omega, k_{\parallel}) x_3] + \sum_{\vec{G}} \vec{E}^s(\omega, \vec{k}_{\vec{G}}) \exp[i\vec{k}_{\vec{G}} \cdot \vec{x}_{\parallel} + i\alpha_0(\omega, k_{\vec{G}}) x_3]. \quad (2)$$

The summation in the second term is over all the translation vectors, \vec{G} , of the reciprocal to the lattice defined by the geometry of the square bigrating. The reciprocal lattice vector, then, can be obtained with the expression

$$\vec{G} \equiv \frac{2\pi}{a} (m_1 \hat{x}_1 + m_2 \hat{x}_2) \quad \text{for } m_j = 0, \pm 1, \pm 2, \dots \quad (3)$$

In equation (2), the wavevectors for the incident wave, \vec{k} , and for each of the scattered waves, $\vec{k}_{\vec{G}}$, are used in the forms given by

$$\vec{k} = \vec{k}_{\parallel} - \alpha_0(\omega, k_{\parallel}), \quad (4a)$$

and

$$\vec{k}_{\vec{G}} = \vec{k}_{\vec{G}} + \alpha_0(\omega, k_{\vec{G}}), \quad (4b)$$

where

$$\vec{k}_{\vec{G}} \equiv \vec{k}_{\parallel} + \vec{G}. \quad (4c)$$

The quantity $\alpha_0(\omega, k_{\vec{G}})$ is then given by the expression

$$\alpha_0(\omega, k_{\vec{G}}) = \begin{cases} \left[\omega^2/c^2 - k_{\vec{G}}^2 \right]^{1/2}, & \text{for } k_{\vec{G}}^2 < \omega^2/c^2, & (5a) \\ i \left[k_{\vec{G}}^2 - \omega^2/c^2 \right]^{1/2}, & \text{for } k_{\vec{G}}^2 > \omega^2/c^2, & (5b) \end{cases}$$

and the quantity $\alpha_0(\omega, k_{\parallel})$ may be obtained by evaluating equation (5) for the case where $\vec{C} = 0$ and $\vec{K}_{\vec{C}} = \vec{k}_{\parallel}$,

$$\alpha_0(\omega, k_{\parallel}) = \alpha_0(\omega, \vec{K}_{\vec{C}}) \Big|_{\vec{C}=0} = \frac{\omega}{c} \cos\theta . \quad (6)$$

The quantities \vec{E}^i and \vec{E}^s in equation (2) denote the vector amplitudes of the incident and scattered fields, respectively. The vector amplitude of the incident field is given by

$$\vec{E}^i(\omega, \vec{k}_{\parallel}) = \left[\hat{k}_{\parallel} + \hat{x}_3 \frac{k_{\parallel}}{\alpha_0(\omega, k_{\parallel})} \right] B_{\parallel} + \left[\hat{x}_3 \times \hat{k}_{\parallel} \right] B_{\perp} , \quad (7)$$

where B_{\parallel} and B_{\perp} determine the magnitudes of the p and s components of the incident field, respectively. The vector amplitude of the scattered field is given by

$$\begin{aligned} \vec{E}^s(\omega, \vec{K}_{\vec{C}}) = & \left[\hat{K}_{\vec{C}} - \hat{x}_3 \frac{K_{\vec{C}}}{\alpha_0(\omega, K_{\vec{C}})} \right] A_{\parallel}(\omega, \vec{K}_{\vec{C}}) \\ & + \left[\hat{x}_3 \times \hat{K}_{\vec{C}} \right] A_{\perp}(\omega, \vec{K}_{\vec{C}}) , \end{aligned} \quad (8)$$

where the A_{\parallel} and A_{\perp} determine the magnitudes of the p and s components of the scattered field, respectively. These are the Rayleigh coefficients which are the unknowns in the problem. Each term in the summation in equation (2), i. e. each scattered field, represents either a diffracted beam, when $K_{\vec{C}} < \frac{\omega}{c}$, or an evanescent wave, when $K_{\vec{C}} > \frac{\omega}{c}$.

Glass, Maradudin and Celli are quite detailed in their method of quantitative elimination of the expression for the field within the dielectric medium and derivation of the final set of linear equations for the Rayleigh

coefficients. The vectorial Kirchoff integral provides an effective boundary condition for the field in the vacuum. As an application of the Rayleigh hypothesis, the expression for the field above the selvedge region, equation (2), is then used in the boundary condition equation.

At this point Fourier expansions in terms of the surface profile are introduced with the intention of rewriting the vector integral as a set of linear equations. One of these expansions is critical to the development of the perturbation theory and is therefore stated here:

$$\exp[-i\alpha\zeta(\vec{x}_{\parallel})] = \sum_{\vec{G}} \mathcal{F}(\alpha|\vec{G}) \exp[i\vec{G} \cdot \vec{x}_{\parallel}]. \quad (9)$$

In this expansion, \mathcal{F} is defined by the integral expression

$$\mathcal{F}(\alpha|\vec{G}) \equiv \frac{1}{a_c} \iint_{a_c} dx_1 dx_2 \exp[-i\{\vec{G} \cdot \vec{x}_{\parallel} + \alpha\zeta(\vec{x}_{\parallel})\}], \quad (10)$$

where a_c is the area of a unit cell of the bigrating surface. The quantity α inside the dielectric must be distinguished from the quantity α_0 in the vacuum, due to the complex dielectric function, $\epsilon(\omega)$, of the medium, and is given by

$$\alpha(\omega, K_{\vec{G}}) = \left[\epsilon(\omega) \frac{\omega^2}{c^2} - K_{\vec{G}}^2 \right]^{1/2}. \quad (11)$$

Glass, Maradudin and Celli use the Fourier expansions to write the Kirchoff integral equation as a doubly infinite set of simultaneous, linear, inhomogeneous equations for $A_{\parallel}(\omega, \vec{K}_{\vec{G}})$ and $A_{\perp}(\omega, \vec{K}_{\vec{G}})$. Using the abbreviations of $A_{\parallel}(\vec{G})$ for $A_{\parallel}(\omega, \vec{K}_{\vec{G}})$ and $A_{\perp}(\vec{G})$ for $A_{\perp}(\omega, \vec{K}_{\vec{G}})$,

the linear equations are given by

$$\sum_{\vec{k}} \frac{\mathcal{I}[\alpha_{\vec{k}}, | \vec{k} - \vec{k}']}{\alpha_{\vec{k}}} \left[a_{\vec{k}}, A_{\parallel}(\vec{k}') + b_{\vec{k}}, A_{\perp}(\vec{k}') \right] \\ = - \frac{\mathcal{I}[\beta_{\vec{k}} | \vec{k}]}{\beta_{\vec{k}}} \left[a_{\vec{k}0} B_{\parallel} + b_{\vec{k}0} B_{\perp} \right], \quad (12a)$$

and

$$\sum_{\vec{k}} \frac{\mathcal{I}[\alpha_{\vec{k}}, | \vec{k} - \vec{k}']}{\alpha_{\vec{k}}} \left[c_{\vec{k}}, A_{\parallel}(\vec{k}') - a_{\vec{k}}, A_{\perp}(\vec{k}') \right] \\ = - \frac{\mathcal{I}[\beta_{\vec{k}} | \vec{k}]}{\beta_{\vec{k}}} \left[e_{\vec{k}} B_{\parallel} - a_{\vec{k}0} B_{\perp} \right], \quad (12b)$$

with the following definitions of terms:

$$\alpha_{\vec{k}}, \equiv \alpha(\omega, K_{\vec{k}}) - \alpha_0(\omega, K_{\vec{k}}), \quad (13a)$$

$$\beta_{\vec{k}} \equiv \alpha(\omega, K_{\vec{k}}) + \alpha_0(\omega, k_{\parallel}), \quad (13b)$$

$$a_{\vec{k}}, \equiv \hat{x}_3 \cdot \left[\hat{K}_{\vec{k}} \times \hat{K}_{\vec{k}}' \right], \quad (13c)$$

$$b_{\vec{k}}, \equiv \hat{K}_{\vec{k}} \cdot \hat{K}_{\vec{k}}', \quad (13d)$$

$$c_{\vec{k}}, \equiv b_{\vec{k}}, + \frac{K_{\vec{k}} K_{\vec{k}}'}{\alpha(\omega, K_{\vec{k}}) \alpha_0(\omega, K_{\vec{k}})}, \quad (13e)$$

and

$$e_{\vec{k}} \equiv \hat{K}_{\vec{k}} \cdot \hat{k}_{\parallel} - \frac{K_{\vec{k}} k_{\parallel}}{\alpha(\omega, K_{\vec{k}}) \alpha_0(\omega, k_{\parallel})}. \quad (13f)$$

2. Perturbation Theory

The essence of the perturbation theory is to reduce all expressions to first order results in terms of the surface profile ζ . This process is begun by expanding the integral \mathcal{I} to first order in ζ yielding the result

$$\mathcal{F}(\alpha|\vec{G}) \approx \delta_{\vec{G},0} - i\alpha\tilde{\zeta}(\vec{G}), \quad (14)$$

where

$$\tilde{\zeta}(\vec{G}) \equiv \frac{1}{a_c} \iint_{a_c} dx_1 dx_2 \zeta(\vec{x}_{\parallel}) \exp[-i\vec{G} \cdot \vec{x}_{\parallel}]. \quad (15)$$

The use of the Kronecker delta function is introduced into the notation in equation (14). With the assumption that the dimensionless parameter $\alpha\zeta$ is small, the expression for \mathcal{F} given by equation (14) may be used in the equations (12) for the Rayleigh coefficients. With the further assumption that $\tilde{\zeta}(0) = 0$, the resulting first order approximations for A_{\parallel} and A_{\perp} are given by

$$\begin{aligned} A_{\parallel}(\vec{G}) = & i \frac{\alpha\vec{G}\vec{G}}{c\vec{G}\vec{G}} \sum_{\vec{G}'} (1 - \delta_{\vec{G},\vec{G}'}) \left[\tilde{\zeta}(\vec{G} - \vec{G}') \left\{ c_{\vec{G}\vec{G}', A_{\parallel}}(\vec{G}') - a_{\vec{G}\vec{G}', A_{\perp}}(\vec{G}') \right\} \right] \\ & - \frac{\alpha\vec{G}\vec{G}}{c\vec{G}\vec{G}} \left[\frac{\delta_{\vec{G},0} - i\beta_{\vec{G}} \tilde{\zeta}(\vec{G})}{\beta_{\vec{G}}} \right] \left[e_{\vec{G}} B_{\parallel} - a_{\vec{G}0} B_{\perp} \right], \quad (16a) \end{aligned}$$

and

$$\begin{aligned} A_{\perp}(\vec{G}) = & i\alpha\vec{G}\vec{G} \sum_{\vec{G}'} (1 - \delta_{\vec{G},\vec{G}'}) \left[\tilde{\zeta}(\vec{G} - \vec{G}') \left\{ a_{\vec{G}\vec{G}', A_{\parallel}}(\vec{G}') - b_{\vec{G}\vec{G}', A_{\perp}}(\vec{G}') \right\} \right] \\ & - \alpha\vec{G}\vec{G} \left[\frac{\delta_{\vec{G},0} - i\beta_{\vec{G}} \tilde{\zeta}(\vec{G})}{\beta_{\vec{G}}} \right] \left[a_{\vec{G}0} B_{\parallel} + b_{\vec{G}0} B_{\perp} \right]. \quad (16b) \end{aligned}$$

The assumption is then made that the Rayleigh coefficients of the specularly diffracted beam, $A_{\parallel}(0)$ and $A_{\perp}(0)$, are of a magnitude such that the amplitude of the specular beam is much greater than any other diffracted beam. The second assumption made here is that there is a possibility of up to four evanescent waves in a condition of

resonance corresponding to four resonantly stimulated surface polaritons. The amplitudes of a resonant evanescent wave will be much greater than that of any of the nonresonant terms. The wavevector for such an evanescent wave is given by

$$\vec{k}_{\vec{G}_r} = \vec{k}_{\parallel} + \vec{G}_r = \vec{k}_{sp}(\omega) \quad \text{for } r = 1, 2, 3, 4, \quad (17)$$

where $\vec{k}_{sp}(\omega)$ is the wavevector of the resonantly excited surface polariton of frequency ω , and where ω is equal to the frequency of the incident light.

Since treatment is limited to only small deviations from the flat surface³, it is beneficial to discuss the limiting case of $\zeta(\vec{x}_{\parallel}) \equiv 0$ to gain some insights to the physical situation. In the flat surface limit, which is zeroth order in the surface profile, the dispersion relation for the surface polariton is given by

$$\alpha(\omega, K_{sp}) + \epsilon(\omega) \alpha_0(\omega, K_{sp}) = 0. \quad (18)$$

The dielectric medium is assumed to be isotropic so that to zeroth order in ζ , the dispersion relation depends only on the magnitude of the surface polariton wavevector, K_{sp} . For a given frequency, then, K_{sp} will describe a circle in k -space on the $k_3 = 0$ plane. Figure 2 is a schematic of this situation with the solid circle representing a circle of radius K_{sp} . The wavevector, $\vec{k}_{\vec{G}_r}$, of a resonantly

³This limitation has been imposed with the use of the Rayleigh hypothesis. See pages 25 and 26 in the exact theory section for a discussion of this limitation.

excited evanescent wave will have its tip at this circle and will satisfy the dispersion relation given by

$$\alpha(\omega, \vec{k}_{\vec{G}_r}) + \epsilon(\omega) \alpha_0(\omega, \vec{k}_{\vec{G}_r}) = 0. \quad (19)$$

The present formulation allows for the possibility of four different reciprocal lattice vectors (\vec{G}_1 through \vec{G}_4 in Figure 2) coupling to \vec{k}_{\parallel} with the resulting evanescent waves satisfying equation (19). The particular situation depicted in Figure 2 shows a case where only one of the resulting evanescent waves, $\vec{k}_{\vec{G}_4}$, satisfies the resonance condition.

The limitation of this schematic representation is that the reciprocal lattice vectors for the bigrating exist only if the surface is not flat, in which case the constant frequency circle for k_{sp} is distorted to some extent by the bigrating corrugations.

Since surface polaritons on a flat surface are p polarized, only the A_{\parallel} coefficients (not the A_{\perp} coefficients) of the resonant evanescent waves need be considered as large with respect to the nonresonant terms. Thus the assumption is that the Rayleigh coefficients $A_{\parallel}(0)$, $A_{\perp}(0)$, $A_{\parallel}(\vec{G}_1)$, $A_{\parallel}(\vec{G}_2)$, $A_{\parallel}(\vec{G}_3)$, and $A_{\parallel}(\vec{G}_4)$, may be larger than all others and should therefore be treated differently. This treatment must allow for the possibility that there may be no resonantly excited evanescent waves and the corresponding Rayleigh coefficients would then be of the same magnitude for the specially treated terms as for all the others.

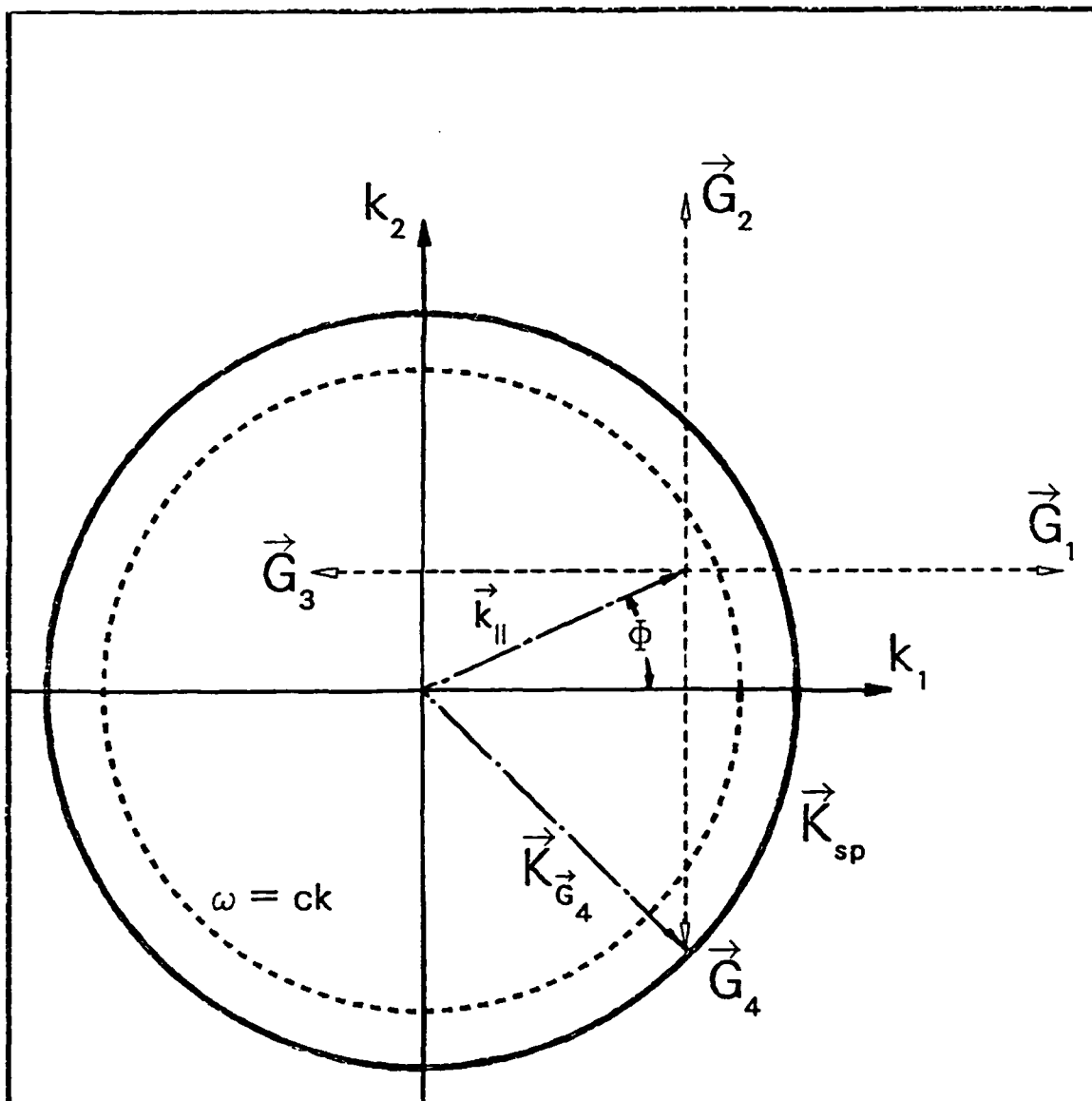


Figure 2. Schematic of Wavevector Coupling.

Having reviewed the basic premise of the perturbation theory, a descriptive summary of the rest of the development advanced by Glass will now be employed. A statement of the final results will be given at the end of this summary.

A further abbreviation is introduced into the notation at this point and mention is made of it here since it is used in the statement of the final results. In this abbreviation, \vec{G}_j is replaced everywhere with its subscript alone, so that $\alpha_{\vec{G}_1 \vec{G}_2}$ is now written as α_{12} , $A_{\parallel}(\vec{G}_3)$ as $A_{\parallel}(3)$, and so forth.

Equation (16) is used to write an explicit expression for each of the six important terms. Each important term is thus written in terms of the other five and also of a sum over the nonresonant terms. Each given nonresonant coefficient can in turn be expressed, by equation (16), in terms of the six important coefficients and all the other nonresonant coefficients. The latter are dropped: each given nonresonant coefficient is expressed only in terms of the six important coefficients. These equations for the nonresonant coefficients are then substituted into the expressions for the resonant and specular beam coefficients.

Within the development of the perturbation theory, an equation arises for the frequency of the surface polariton to zeroth order in ζ . This expression, which is the solution of equation (18), will be useful in later discussions and is stated here as

$$\omega_r^2 = \left[\frac{1 + \epsilon}{\epsilon} \right] c^2 k_r^2 . \quad (20)$$

The final result is a set of six linear algebraic equations for the resonant and specular beam coefficients in terms of the amplitude coefficients, B_{\parallel} and B_{\perp} , of the incident beam. These equations are given in matrix form as

$$\begin{bmatrix}
 (\Omega^2 - \tilde{\Omega}_1^2) & L_{12} & L_{13} & L_{14} & M_1 & N_1 \\
 L_{21} & (\Omega^2 - \tilde{\Omega}_2^2) & L_{23} & L_{24} & M_2 & N_2 \\
 L_{31} & L_{32} & (\Omega^2 - \tilde{\Omega}_3^2) & L_{34} & M_3 & N_3 \\
 L_{41} & L_{42} & L_{43} & (\Omega^2 - \tilde{\Omega}_4^2) & M_4 & N_4 \\
 O_1 & O_2 & O_3 & O_4 & (1+P) & Q \\
 R_1 & R_2 & R_3 & R_4 & S & (1+T)
 \end{bmatrix}
 \begin{bmatrix}
 A_{\parallel}(1) \\
 A_{\parallel}(2) \\
 A_{\parallel}(3) \\
 A_{\parallel}(4) \\
 A_{\parallel}(0) \\
 A_{\perp}(0)
 \end{bmatrix}
 =
 \begin{bmatrix}
 (U_1 - M_1)B_{\parallel} - N_1 B_{\perp} \\
 (U_2 - M_2)B_{\parallel} - N_2 B_{\perp} \\
 (U_3 - M_3)B_{\parallel} - N_3 B_{\perp} \\
 (U_4 - M_4)B_{\parallel} - N_4 B_{\perp} \\
 (W+V-P)B_{\parallel} - QB_{\perp} \\
 (X-S)B_{\parallel} - (T + \frac{\alpha_{00}}{\beta_0})B_{\perp}
 \end{bmatrix} . \quad (21)$$

It should be noted that the quantity Ω , defined by

$$\Omega \equiv \frac{\omega}{2\pi c/a} = \frac{a}{\lambda} , \quad (22)$$

is merely the incident wave frequency expressed as a dimensionless quantity. Also note that the quantity $\tilde{\Omega}_r$ is defined by

$$\tilde{\Omega}_r \equiv \frac{\tilde{\omega}_r}{2\pi c/a} , \quad (23)$$

where $\tilde{\omega}_r$ is just the surface polariton frequency for the flat surface, ω_r from equation (20), renormalized by the nonresonant terms, which were kept in the theory. An explicit definition for $\tilde{\omega}_r$ is given in equation A.1 of Appendix A. The other terms appearing here are defined explicitly in Appendix A taken from the technical report by Glass.

The procedure of calculation, then, is to solve this set of six equations numerically for the resonant and specular beam coefficients. These results are then used in the equations for the nonresonant coefficients to obtain their values.

III. NUMERICAL IMPLEMENTATION

The numerical implementations here are, for purposes of comparison, exactly analogous to those performed by Glass [Ref. 21] in instituting the perturbation theory with simultaneous excitation of two resonant surface polaritons. In his quantitative evaluations employing the exact theory, Glass parallels those conducted by Glass, Maradudin and Celli [Ref. 5]. The exact method here duplicates that employed by Glass but for a somewhat different geometry. The implementation of the four-polariton perturbation theory will parallel the method used by Glass in the implementation of his original perturbation theory.

A. QUANTITIES AND GEOMETRY INVESTIGATED

In the numerical investigation of the theory, normalized values are chosen for the incident amplitude coefficients, B_{\parallel} and B_{\perp} . In the cases investigated, either total p polarization, $B_{\parallel} = 1$ and $B_{\perp} = 0$, or total s polarization, $B_{\parallel} = 0$ and $B_{\perp} = 1$, was chosen for the incident beam. The resulting Rayleigh coefficients, then, will be some fraction of unity indicating the magnitudes of the p and s components of the evanescent waves and the diffracted beams relative to the magnitude of the incident beam.

The surface profile used for the investigations duplicates the one employed by Glass [Ref. 21]. It describes a square sinusoidal bigrating with a profile symmetric along x_1 and x_2 with periodicity a . The bigrating surface is depicted schematically in Figure 1 in Chapter II. The surface profile function is given by

$$\begin{aligned} \zeta(\vec{x}_{\parallel}) \equiv & h_1 \left\{ \cos\left[\frac{2\pi}{a} x_1\right] + \cos\left[\frac{2\pi}{a} x_2\right] \right\} \\ & + h_2 \left\{ \cos\left[\frac{4\pi}{a} x_1\right] + \cos\left[\frac{4\pi}{a} x_2\right] \right\} \\ & + h_{11} \left\{ \cos\left[\frac{2\pi}{a} x_1\right] \cos\left[\frac{2\pi}{a} x_2\right] \right\} \end{aligned} \quad (24)$$

The reciprocal lattice vectors for this square bigrating are given by

$$\vec{G}(l, m) = \frac{2\pi}{a} \left[l \hat{x}_1 + m \hat{x}_2 \right], \quad l, m = 0, \pm 1, \pm 2, \dots \quad (25)$$

Thus one may refer to $\vec{G}(l, m)$ as the (l, m) reciprocal lattice vector. Similarly, a particular scattered beam, corresponding to the (l, m) lattice vector, may be referred to as the (l, m) diffracted beam or the (l, m) evanescent wave. With this reference scheme, the wavevector of a scattered beam projected onto the surface is written as

$$\vec{K}(l, m) = \vec{K}_{\parallel} + \vec{G}(l, m) = \vec{K}_{\parallel} + \frac{2\pi l}{a} \hat{x}_1 + \frac{2\pi m}{a} \hat{x}_2. \quad (26)$$

Once numerical results for the Rayleigh coefficients are obtained, equation (8) is used to find the amplitude of the scattered field. The amplitude of the incident field is obtained with equation (7) using the known amplitude coefficients B_{\parallel} and B_{\perp} . The reflectance of the (l, m)

diffracted beam [Ref. 21:p. 2653] is then given by

$$\mathfrak{R}(l, m) = \frac{|\vec{E}^S[\omega, \vec{K}(l, m)]|^2 \alpha_o[\omega, K(l, m)]}{|\vec{E}^I[\omega, \vec{K}_{||}]|^2 \alpha_o[\omega, k_{||}]}, \quad (27a)$$

with the total reflectance given by the expression

$$\mathfrak{R} = \sum_{l'} \sum_{m'} \mathfrak{R}(l', m'), \quad (27b)$$

where the primes on the indices indicate summations are carried out only for l' and m' such that $K^2(l', m') < \omega^2/c^2$, thereby excluding evanescent wave terms. Using the amplitudes of the scattered and incident fields, the amplitude for the total field may be obtained by evaluating equation (2). The electric field enhancement is defined [Ref. 21:p. 2653] as

$$\xi \equiv \frac{|\vec{E}(\omega, \vec{x})|^2}{|\vec{E}^I[\omega, \vec{K}_{||}]|^2} \Bigg|_{x_3 = \zeta_{\max}^+}, \quad (28)$$

where ζ_{\max}^+ indicates a point just above the selvedge region.

B. EXACT THEORY IMPLEMENTATION

The method of exact theory implementation described here is a summary of the procedure outlined by Glass [Ref. 21:pp. 2653-2654]. This reference will not be cited further within this section.

In determining the Rayleigh coefficient values using the exact analysis, the integral \mathfrak{R} given in equation (10) must

be evaluated for all possible reciprocal lattice vectors. There is, in general, no analytic expression for \mathcal{F} and numerical calculations thus require performance of a fast Fourier transform (FFT) for each possible \vec{G} . The surface profile function term with the height coefficient h_{11} , the cross term, would require the use of a two dimensional Fourier transform in direct application. Expansion of the exponential of the cross term may be used to circumvent the use of a two dimensional Fourier transform. With this method the expression for the integral \mathcal{F} for the cross term case may be rewritten as

$$\mathcal{F}(\alpha|\vec{G}) = \sum_{n=0}^{\infty} \frac{[-i\alpha h_{11}]^n}{n!} \mathcal{F}^{(n)}(\alpha|G_1) \mathcal{F}^{(n)}(\alpha|G_2), \quad (29a)$$

where

$$\vec{G} = G_1 \hat{x}_1 + G_2 \hat{x}_2, \quad (29b)$$

and

$$\begin{aligned} \mathcal{F}(\alpha|G_v) \equiv \frac{1}{a} \int_{-a/2}^{+a/2} \cos^n \left[\frac{2\pi x}{a} \right] \exp[-iG_v x] \\ + \exp \left[-i\alpha \left\{ h_1 \cos \left[\frac{2\pi x}{a} \right] + h_2 \cos \left[\frac{4\pi x}{a} \right] \right\} \right] dx. \end{aligned} \quad (29c)$$

This integral can then be evaluated using a one dimensional FFT and a numerical result may be obtained for $\mathcal{F}(\alpha|\vec{G})$ by truncating the summation in equation (29a) to as many terms as is required to achieve the desired degree of accuracy.

Using this numerical result for $\mathcal{F}(\alpha|\vec{G})$, equation (9) is then solved as a set of linear equations in matrix form in

order to determine the values for the Rayleigh coefficients. To do this, as previously indicated, the resulting doubly infinite matrix equation must be truncated to some degree. The dimensions of the matrix determine the reciprocal lattice vectors that are retained in the numerical calculation. For truncation to a matrix of dimensions $2N^2 \times 2N^2$, the lattice vectors $\vec{G}(l,m)$ retained in the calculation are those where l and m satisfy the condition

$$-\frac{N-1}{2} \leq l, m \leq +\frac{N-1}{2} . \quad (30)$$

Thus the diffracted beams and evanescent waves corresponding to reciprocal lattice vectors with either index outside these limits is ignored in determination of numerical results. For the limitation of both l and m to the range from -2 to $+2$, the resulting N is 5 and the matrix to be solved is then of 50×50 dimension; for the range -3 to $+3$, $N = 7$ and the matrix is 98×98 ; for -4 to $+4$, $N = 9$ with a 162×162 matrix to be solved. Should accuracy require extension of the limits for l and m to -5 to $+5$, N is then 11 and the matrix dimensions are 242×242 .

The elements of the matrix are complex, as are the required FFT's. Using the full (double) precision available with a 32 bit machine⁴ is desirable to obtain the necessary accuracy, particularly in the larger matrix calculations.

⁴The machine employed here was an IBM 3033 system and a 32 point mesh was used in the FFT's for the exact calculations.

With such requirements in computational resources for numerical determinations based on the exact analysis, the need for reliable perturbation schemes is clearly evident.

The Fortran code employed in calculations here is the same as that used by Glass in his exact calculations for comparison with the two-polariton perturbation theory.

C. PERTURBATION THEORY IMPLEMENTATION

Since the integral $\oint(\alpha|\vec{G})$ has been eliminated from the calculations in the perturbative analysis, no FFT's need be performed. The quantity $\tilde{\zeta}(\vec{G})$, defined by equation (15), is all that is required and, for the surface profile defined by equation (24), is written [Ref. 21:p.2654] as

$$\begin{aligned} \tilde{\zeta}(l,m) = & \frac{1}{2} \delta_{l,0} \left[h_1 \delta_{|m|,1} + h_2 \delta_{|m|,2} \right] \\ & + \frac{1}{2} \delta_{m,0} \left[h_1 \delta_{|l|,1} + h_2 \delta_{|l|,2} \right] \\ & + \frac{1}{4} h_{11} \delta_{|l|,1} \delta_{|m|,1} \end{aligned} \quad (31)$$

The set of linear equations defined by the 6×6 matrix equation (21) are then solved to determine the values for the Rayleigh coefficients.

The numerical calculations here still involve complex quantities and full (double) precision was also employed. The calculations, however, by excluding FFT's and reducing the linear equation solution to a 6×6 problem, require

computational resources that are orders of magnitude less than the exact calculation requirements.

The Fortran code employed for the perturbation calculations is a modification to that used by Glass for the two polariton perturbation code. Necessary changes were carried out and the results tested against exact results for identical cases in order to correct program errors.

D. SELECTION OF PARAMETERS

To conform with the experimental work of Inagaki *et al.* [Ref. 20] and with the theoretical work of Glass and Maradudin [Ref. 19] and that of Glass [Ref. 21], the wavelength of the incident light was chosen as 633.0 nm. In order to test the possibility of four-fold resonance advanced by Glass [Ref. 9:p. 13], it was desirable to choose the geometry so as to have resonant absorption at normal incidence. In this manner, resonance effects would be dramatic, *i. e.*, approximately total absorption of light at normal incidence, and any qualitative trends in resonance conditions would be readily apparent.

For normal incidence, the projection of the incident wavevector is zero and the resonance condition, from equation (17), is then

$$\vec{k}_r = 0 + \vec{G} = \vec{k}_{sp}(\omega). \quad (32)$$

Choosing the (1,0) lattice point for convenience, the

resulting reciprocal lattice vector from equation (25) is given by

$$\vec{G}(1,0) = \frac{2\pi}{a} \hat{x}_1. \quad (33)$$

Combining these, the resulting resonance condition is

$$K_{sp}^2 = K_r^2 = G^2(1,0) = \left[\frac{2\pi}{a}\right]^2. \quad (34)$$

Using a zeroth order approximation in ζ , equation (20) may be employed with the result from equation (34) yielding

$$\omega_r^2 = \left[\frac{1 + \epsilon}{\epsilon}\right] c^2 \left[\frac{2\pi}{a}\right]^2. \quad (35)$$

Assuming that the frequency of the incident light equals the frequency of the surface polariton at $K_{sp} = 2\pi/a$, and assuming that this surface polariton frequency is approximately equal to the flat surface polariton frequency, then ω_r can be replaced by ω in equation (35). Then one may write

$$a^2 = \left[\frac{2\pi c}{\omega}\right]^2 \left[\frac{\epsilon}{1 + \epsilon}\right]. \quad (36)$$

Substituting the wavelength of the incident light in vacuum, λ_0 , into this equation, the final result is obtained for the approximate periodicity for resonance at normal incidence as

$$a = \lambda_0 \left[\frac{\epsilon}{1 + \epsilon}\right]^{1/2}. \quad (37)$$

As in the work of Inagaki et al., Glass and Maradudin, and Glass, the material chosen for the bigrating was silver. Interpolating from the data measured by Johnson and Christy [Ref. 26] for Ag, the value of the dielectric function at

the incident wavelength of 633.0 nm is $\epsilon = -18.3 + i 0.479$. Taking the real part of this value the resulting value for a from equation (37) is 615.47 nm.

Although the projection of the incident wavevector onto the surface is zero for the case of normal incidence, some finite non-zero value must be used for $|\vec{k}_{\parallel}|$ in the numerical calculations in order to define the unit vectors in equation (17). In executing a computational run, the value for k_{\parallel} is not defined as an explicit input parameter but is derived from the specification of the angle of incidence, θ . For this reason θ was specified as 10^{-5} degrees for computational runs in cases of normal incidence.

Taking the values of $a = 614.47$ nm and $\lambda_0 = 633.00$ nm, numerical calculations of exact theory were performed for p polarized light at normal incidence and zero azimuth with the surface profile height coefficients h_2 and h_{11} as zero. This case was repeated for several choices of h_1 in order to establish an optimum value for maximum absorptance at normal incidence. This resulted in the choice for the optimum coupling value of h_1 as 7.4 nm. The results of these calculations are not formally presented here as their sole purpose was to establish this optimum coupling value.

IV. VALIDATION AT OFF-NORMAL INCIDENCE

Within the literature there has been considerable use of two types of scans in the numerical search for the resonance condition of a particular case [Ref. 27]. In the first method the reflectance is scanned for a resonance dip by variation of the angle of incidence, θ . Referring to Figure 1 in subsection B.1 of Chapter II, it is apparent that this is an implicit variation of the value of k_{\parallel} ⁵. As the value of k_{\parallel} is changed, the resonant coupling condition is approached, met, and then passed and the reflectance is scanned through the resonance dip. A second method is to vary the incident frequency. Referring to Figure 2 in subsection B.2 of Chapter II, this has the effect of changing the radius of the constant frequency circle at the tip of the resonant surface polariton. Here, k_{\parallel} is held fixed and the resonant coupling condition changes, thereby scanning the reflectance as a function of frequency. For cases of off-normal incidence, only scans versus the angle of incidence have been executed.

Along with the scans for reflectance, the concomitant enhancement peaks were also obtained. These results are not

⁵See equation (1) in subsection II.B.1.

central to the present discussions and are therefore relegated to Appendix B as Figures 28 through 46.

A. RESULTS AT OFF-NORMAL INCIDENCE

As discussed in section D of Chapter III, the values of $\lambda = 633.00$ nm and $a = 615.47$ nm were chosen for the incident wavelength and grating period and then the optimum coupling value of 7.4 nm for h_1 was established at normal incidence. A value of 5 degrees was arbitrarily chosen for the azimuthal angle, ϕ , and scans of reflectance versus the angle of incidence, θ , were carried out for several values of h_1 . The primary purpose in these calculations was to establish the limits of validity for the perturbation theory in cases of off-normal incidence. The values of h_1 used were multiplicative factors of the baseline value: one-third, 2.5 nm; one-half, 3.7 nm; unity, 7.4 nm; and twice, 14.8 nm. For all of these calculations, the values of h_2 and h_{11} were held at zero. From equation (24), the resulting values for ζ_{\max} may be calculated and the corresponding corrugation strengths⁶ are 0.008, 0.012, 0.024, and 0.048, respectively. The incident light was specified as s polarized for all cases, with the $h_1 = 7.4$ nm case repeated using p polarization. The results of the scans for reflectance for each of these cases are

⁶See equations (34) and (36) in section III.D.

graphically depicted in Figures 3 through 7 on the following five pages. Within these figures, as with all of the figures to be presented, the results for exact theory calculations are shown as a dashed curve and the results for perturbation calculations are shown as a solid curve.

As can be seen from a comparison of the figures, the perturbation theory is the most reliable at the weakest corrugation. Minimum reflectance for this case is approximately 0.8. Fair agreement is held between exact and perturbation results for increases in h_1 to 3.7 nm and 7.4 nm as shown in Figures 4, 5 and 7. In the latter case, the reflectance minimum falls to approximately 0.13 for s polarization. With the increase in h_1 to 14.8 nm, the perturbation theory breaks down and is unable to predict the results, as can be seen in Figure 6.

Some definitions for use in quantitative comparison of exact theory and perturbation theory results need to be established at this point. The departures which are to be quantitatively characterized are the difference in the magnitude of the reflectance dip and the difference in the θ location of the dip. The differences should be normalized with an appropriate quantity so that they may be considered as a type of percentage error.

For the reflectance minimum, the difference in the maximum absorptances for exact and perturbation results will be used. This quantity will then be normalized with the

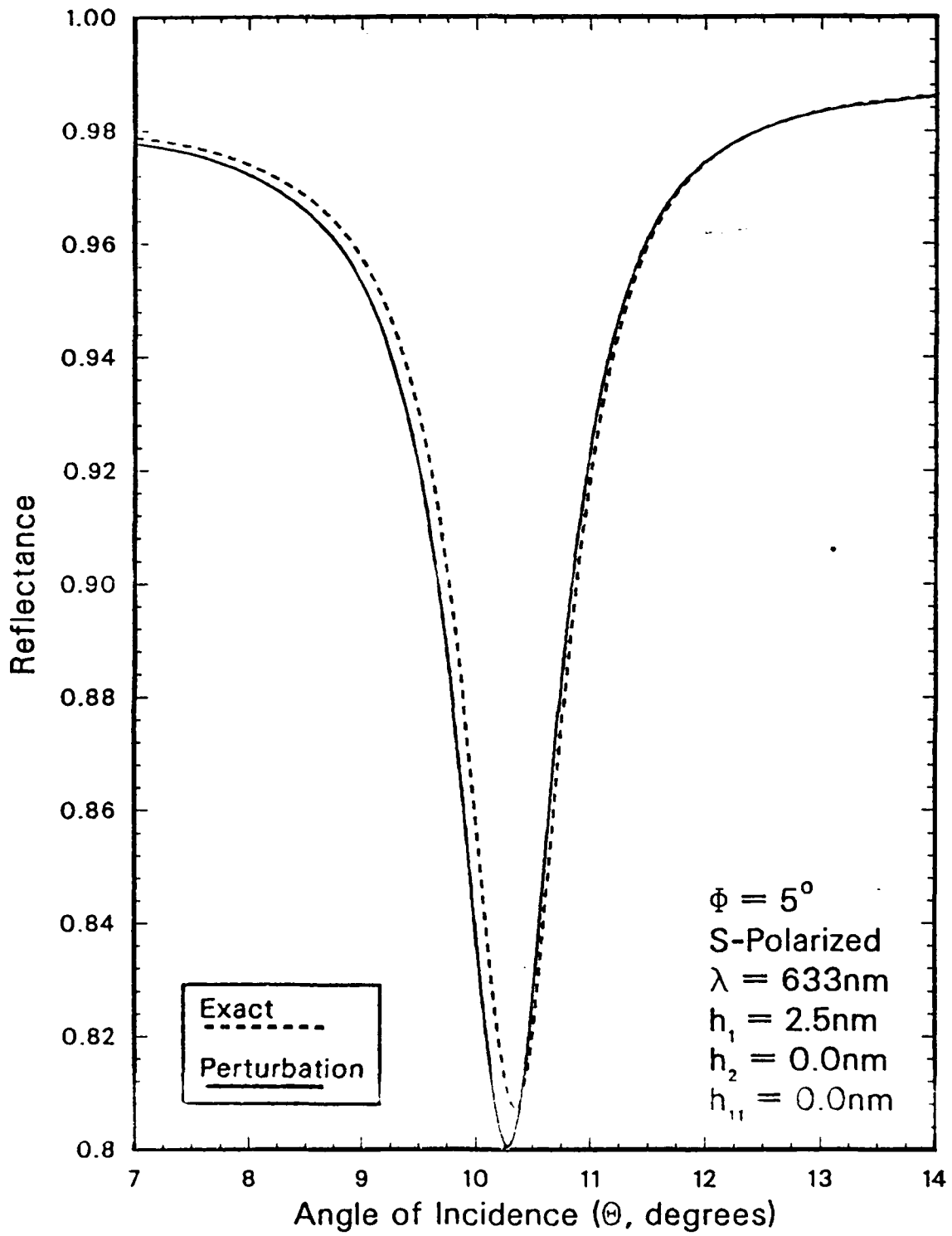


Figure 3. Reflectance Curves for 5° Azimuth with h_1 at 2.5 nm.

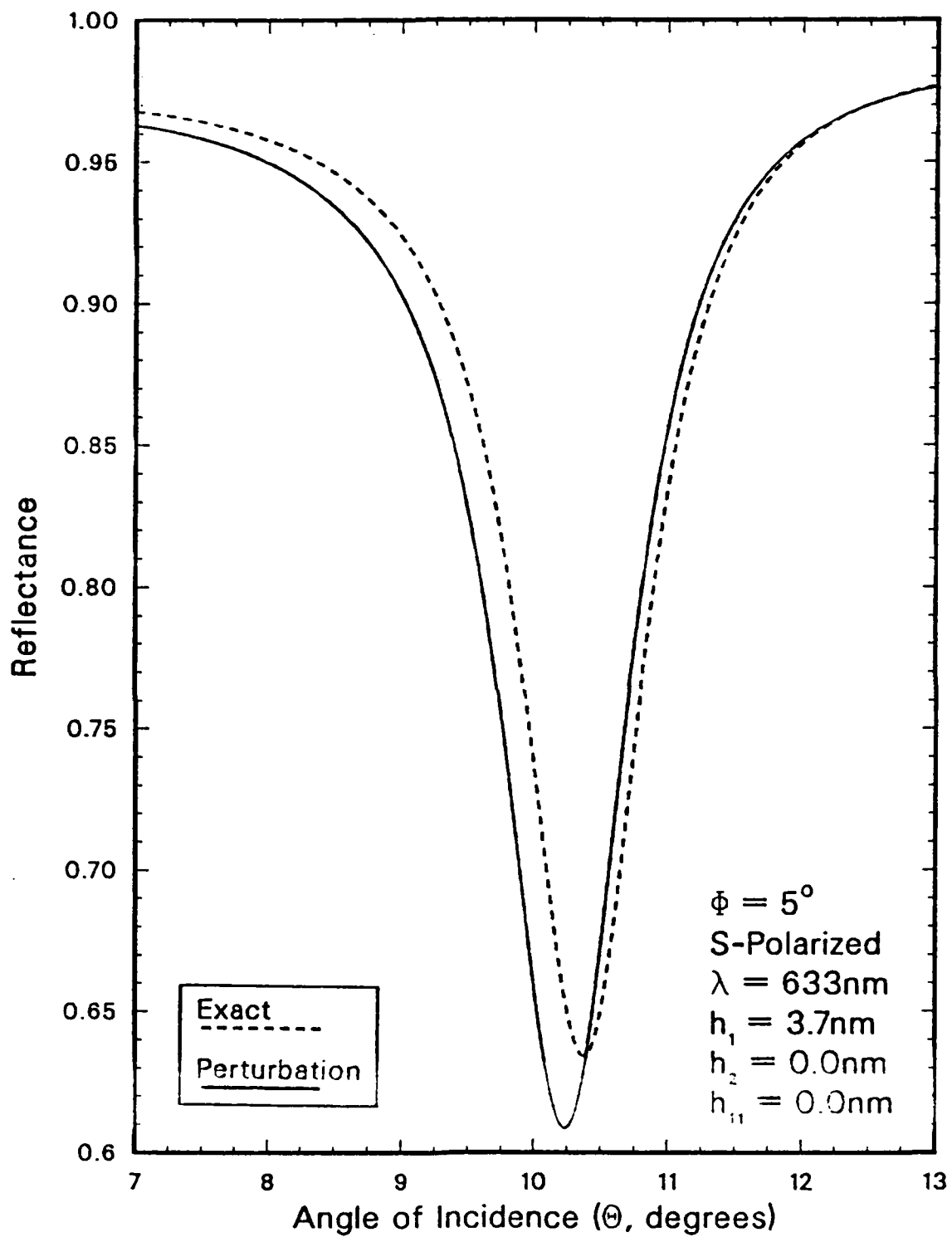


Figure 4. Reflectance Curves for 5° Azimuth with h_1 at 3.7 nm.

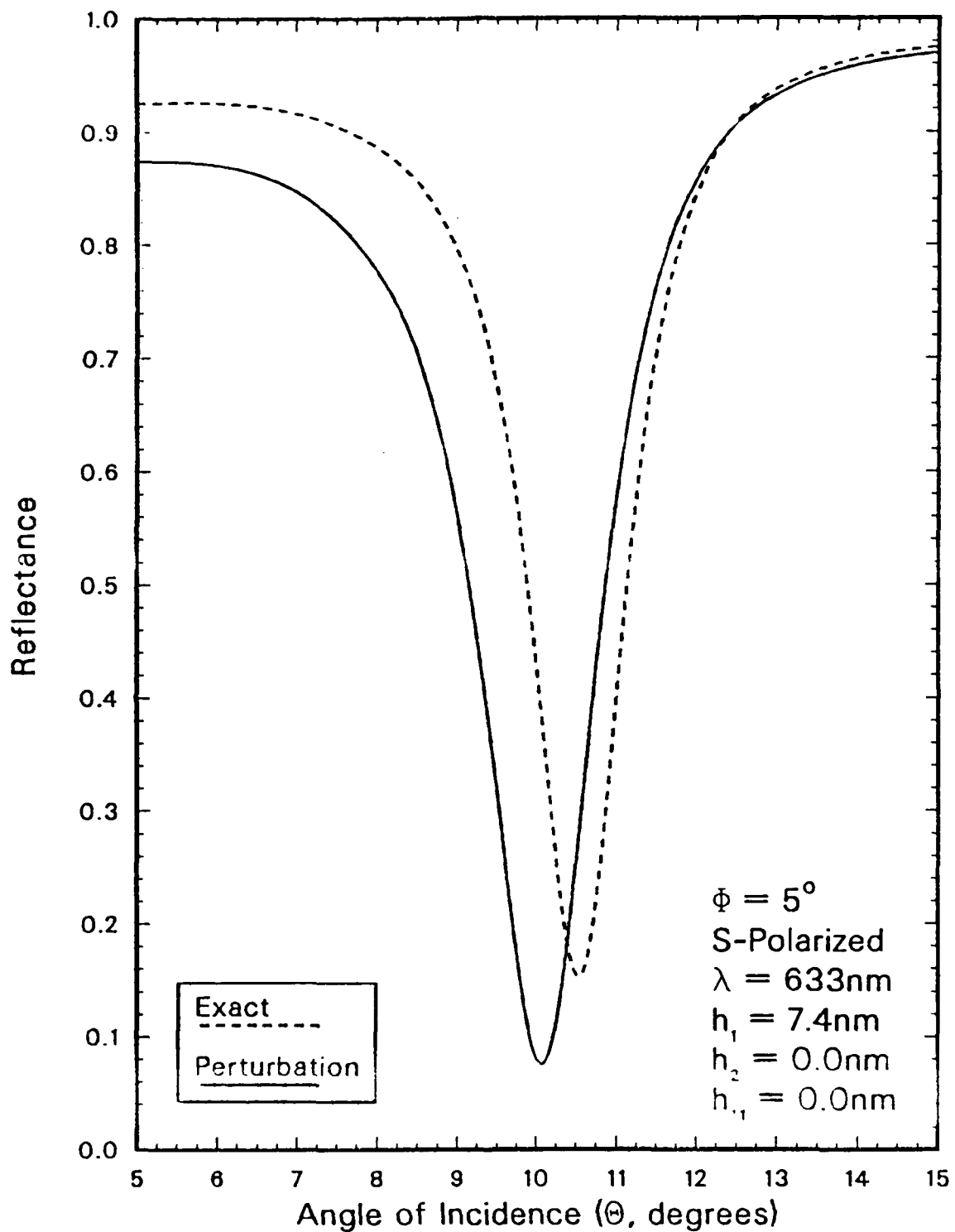


Figure 5. Reflectance Curves for S Polarized Light at 5° Azimuth and h_1 at 7.4 nm.

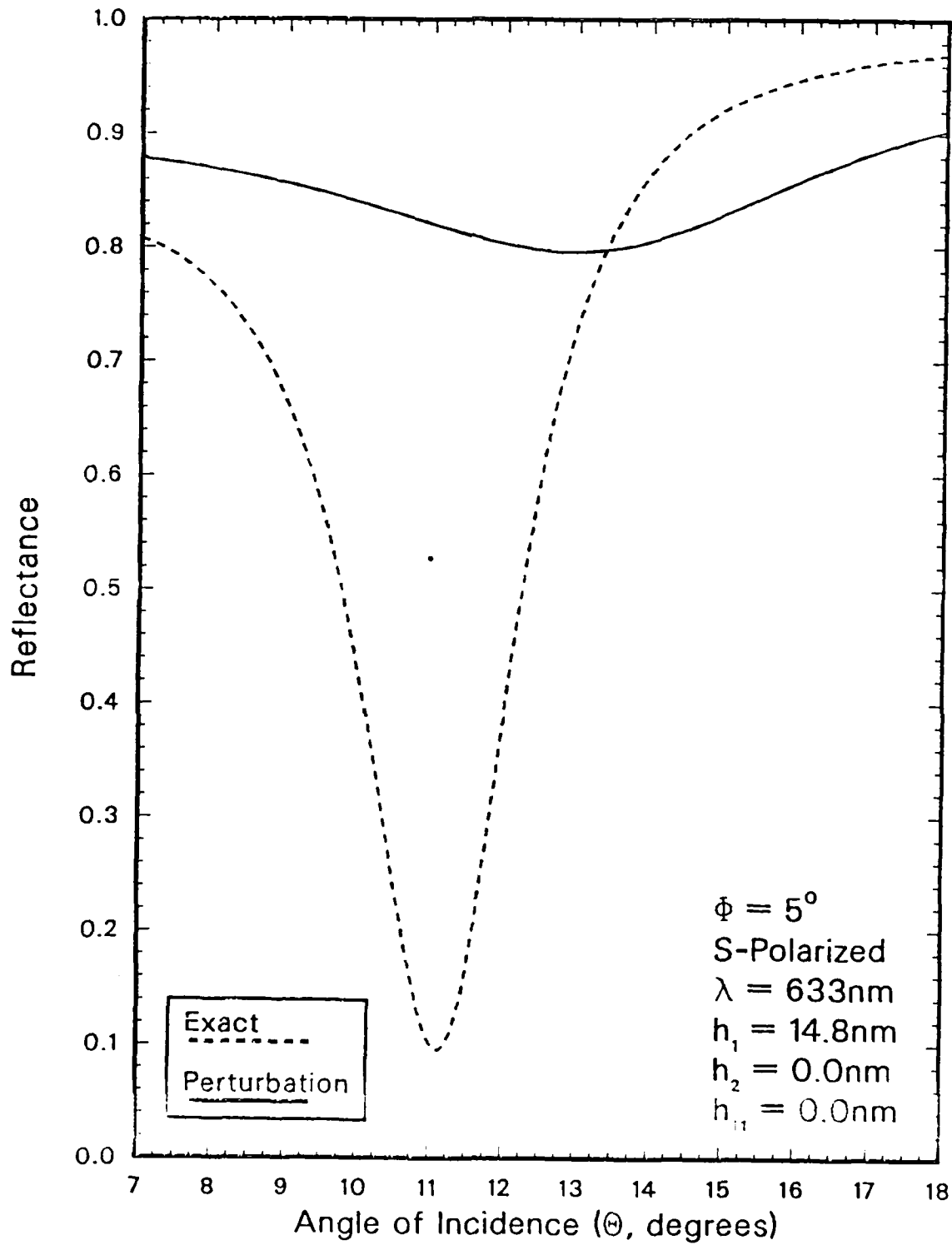


Figure 6. Reflectance Curves for 5° Azimuth with h_1 at 14.8 nm.

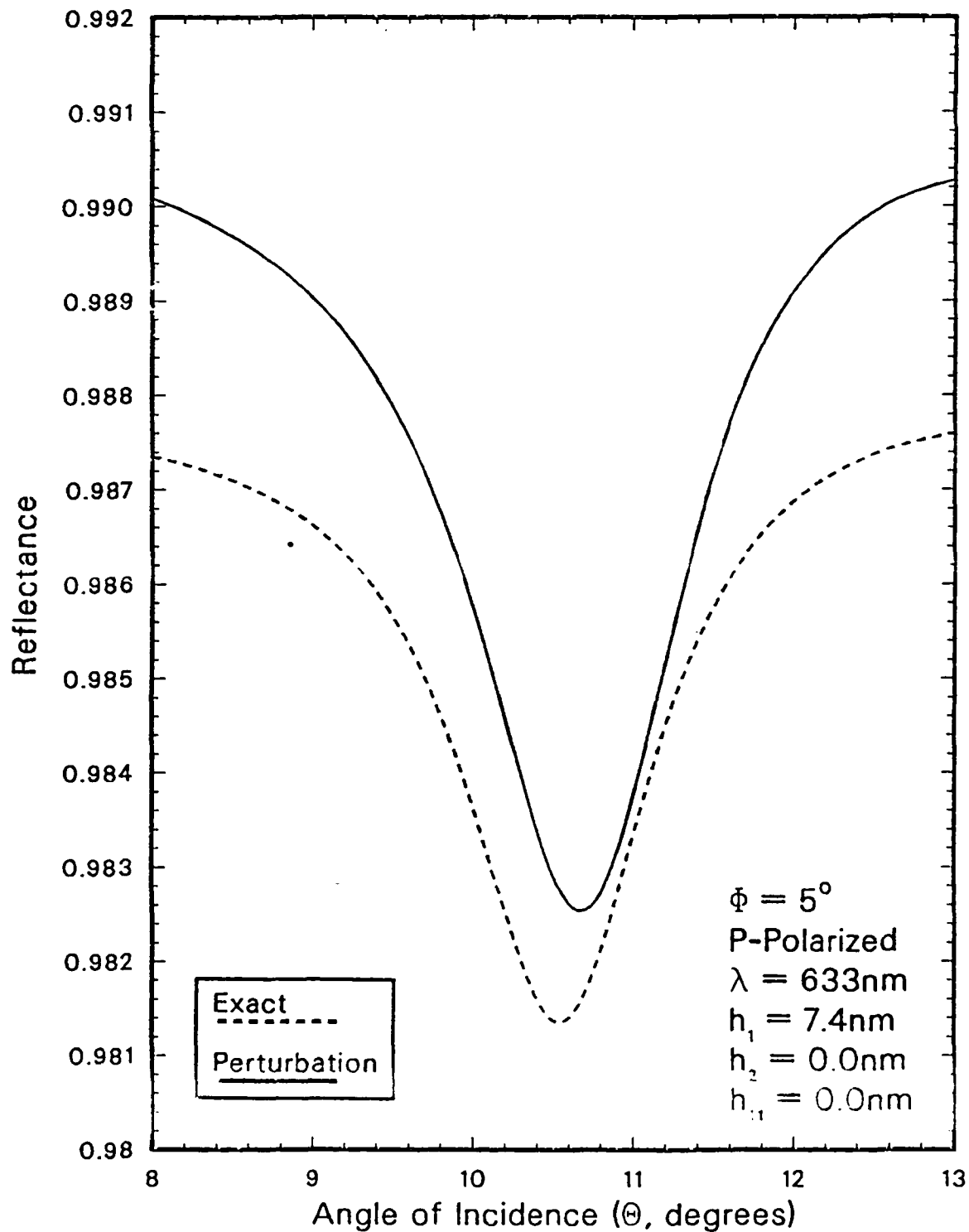


Figure 7. Reflectance Curves for P Polarized Light at 5° Azimuth and h_1 at 7.4 nm.

maximum absorptance of the exact theory results. To avoid introduction of another quantity, this error quantity will be defined in terms of reflectance minima. The reflectance minimum for the exact theory results is denoted as \mathfrak{R}_0 and for the perturbation results as \mathfrak{R}'_0 . With this notation, the difference as a percentage, $\Delta\mathfrak{R}$, is defined as

$$\Delta\mathfrak{R} \equiv \frac{|(1-\mathfrak{R}_0) - (1-\mathfrak{R}'_0)|}{1 - \mathfrak{R}_0} \times 100\% = \frac{|\mathfrak{R}_0 - \mathfrak{R}'_0|}{1 - \mathfrak{R}_0} \times 100\% . \quad (38)$$

Characterization of the difference in the θ location of the reflectance minima will be accomplished through the use of the differences in the magnitudes of the corresponding \vec{k}_{sp} wavevectors. From equations (17) and (26), it can be readily seen that this is identical to the differences in the magnitudes of the corresponding \vec{k}_{\parallel} wavevectors. This difference, ΔK_{sp} , will be normalized with the calculated value of the surface polariton wavevector magnitude. This value of K_{sp} may be taken directly from equation (34) as $2\pi/a$. It can be readily determined from equation (1) for \vec{k}_{\parallel} that

$$\Delta K_{sp} = k_{\parallel 0} - k'_{\parallel 0} = \frac{\omega}{c} (\sin\theta_0 - \sin\theta'_0), \quad (39)$$

where, as before, the subscript naughts indicate values at minimum reflectance and the prime indicates the perturbation theory value. Dividing by the normalization factor, K_{sp} , and using the relations in equations (36) and (37) to rewrite the multiplicative constant, the normalized

wavevector difference as a percentage, which will be denoted as Δk , can be defined as

$$\Delta k \equiv \frac{a}{\lambda_0} |\sin\theta_0 - \sin\theta'_0| \times 100\% , \quad (40)$$

where λ_0 is the wavelength of the incident light in the vacuum.

Similar definitions may be obtained for the differences in peak enhancement magnitudes and the peak enhancement locations. Although presentation of these curves is confined to Appendix B to promote continuity, the quantitative comparisons will be included in tabulated results within the text of the chapters for completeness. For the percentage difference in enhancement peaks, the definition employed is

$$\Delta \epsilon \equiv \frac{|\epsilon_0 - \epsilon'_0|}{\epsilon_0} \times 100\% . \quad (41)$$

The definition of the angular error, expressed as a percentage in wavevector form, is exactly analogous to equation (40) and will be denoted by Δk_g for the enhancement values.

The values for the percentage differences for the five cases at the azimuthal angle of $\phi = 5^\circ$ are given in Table 1, on the following page. Note from these results that the reflectance from exact calculations for the h_1 value of 14.8 nm is less than 0.1 with an enhancement of over 400. The perturbation theory, however, predicts a reflectance dip down to 0.800 with an enhancement of only 99.1 for this

case. The position errors are an order of magnitude greater than the others noted in Table 1 but are still less than five percent.

TABLE 1
 PERCENTAGE DIFFERENCES OF EXACT AND PERTURBATION
 RESULTS FOR $\phi = 5^\circ$ AZIMUTH

h_1 (nm)	Pol.	ξ_0	ξ_0	$\Delta\xi$	$\Delta\kappa$	$\Delta\delta$	$\Delta\kappa_g$
2.5	s	0.808	65.0	3.5%	0.10%	2.9%	0.12%
3.7	s	0.634	132.	7.0%	0.23%	5.5%	0.23%
7.4	s	0.153	342.	9.2%	0.77%	2.9%	0.84%
14.8	s	0.095	437.	77.%	3.1%	77.%	2.0%
7.4	p	0.981	3.35	6.4%	0.23%	10.%	0.17%

This breakdown supports the explanation offered by Glass [Ref. 21:p. 2654] for the limitation of his perturbation theory using two resonant polaritons. Briefly, the argument is as follows. The basis of the perturbation theory is the expansion of the quantity $\exp[-i\alpha\zeta]$. At resonance, the approximation may be made that

$$|\alpha[K(1,m)]|\zeta_{\max} \approx \left[\frac{2\pi|\epsilon|}{[|\epsilon| - 1]^{1/2}} \right] \frac{\zeta_{\max}}{\lambda_0} . \quad (42)$$

When $\alpha\zeta_{\max}$ exceeds one, the expansion series does not converge rapidly and truncation to a few terms is no longer a good approximation of its value. Thus the perturbation theory breaks down.

For the $h_1 = 14.8$ nm case, evaluation of equation (42) yields a value of 1.3 for $\alpha\zeta_{\max}$. At the 7.4 nm height, the value is $\alpha\zeta_{\max} \approx 0.65$. Thus the perturbation theory using four polariton resonance appears to follow the breakdown pattern of the two polariton theory in cases of off-normal incidence.

A comparison of the results for $h_1 = 7.4$ nm with s and p polarization of incident light illustrates an important point. Note in Table 1 that the reflectance minimum for the s polarized case is 0.15, while the minimum for the p polarized case is only down to 0.98. Figure 8 is a schematic of the wavevector coupling with an azimuth of 5° . In this schematic., unlike Figure 2, the two dimensional Brillouin zone boundary is shown, represented by the solid square surrounding the constant frequency circle. Also, this circle is pictured with the gaps which are present at the intersections with the zone boundary. The directions of the incident fields for the cases of s and p polarization are shown projected onto the $k_3 = 0$ plane. The wavevector of the resonant evanescent wave is represented by the dashed vector with the open arrowhead (not labeled).

The surface polariton has both a transverse field component normal to the surface and longitudinal field component parallel to the surface and in the direction of polariton propagation. An incident wave of s polarization has its electric field vector perpendicular to the plane of

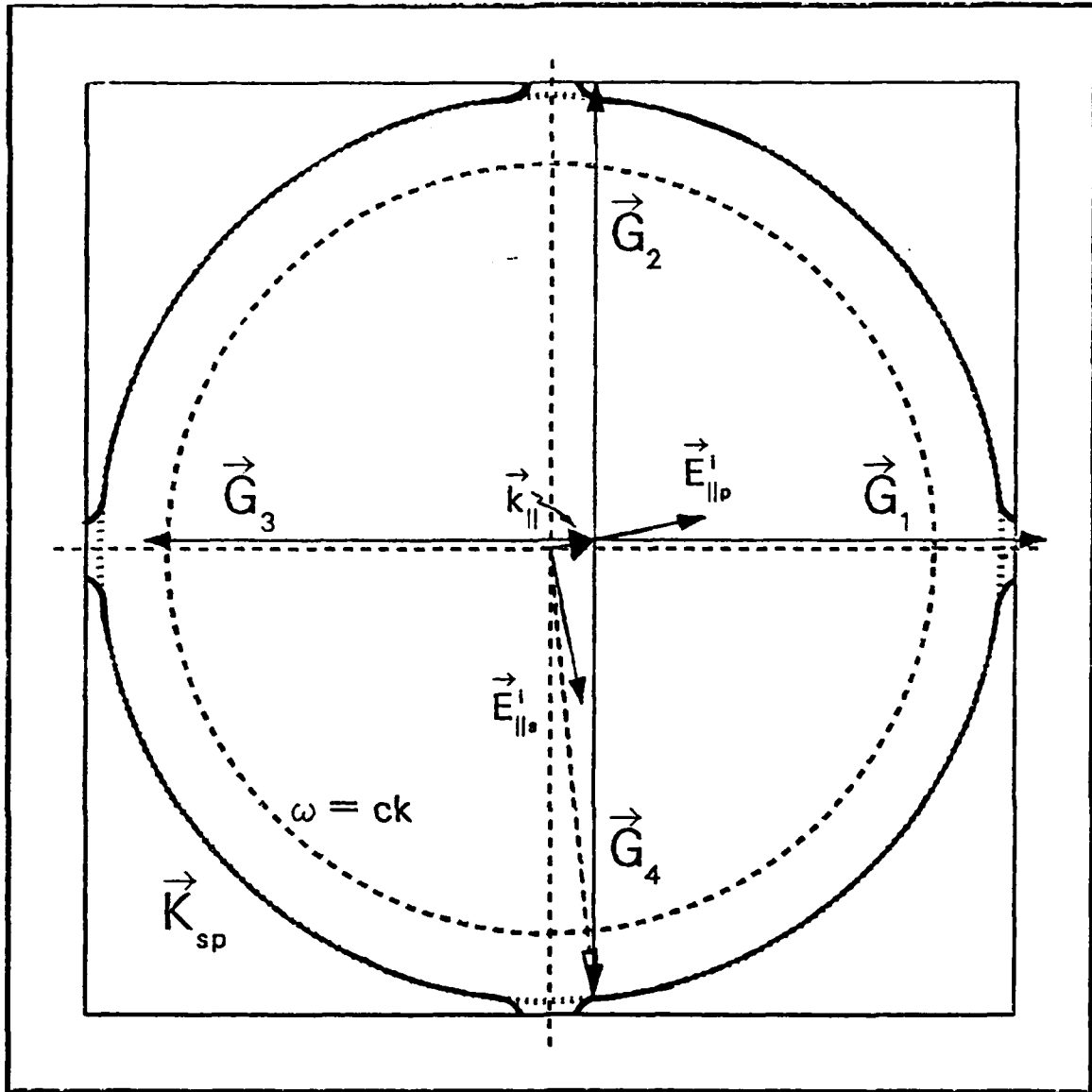


Figure 8. Schematic of Wavevector Coupling at 5° Azimuth.

incidence and, therefore, has no field component normal to the surface. An incident wave of p polarization, however, does have an electric field component normal to the surface. The magnitude of this normal component is proportional to the angle of incidence.

Referring to Figure 8, it can be seen that with s polarization, the incident field is almost collinear with the direction of propagation of the surface polariton and thus with its longitudinal field component. Whereas with p polarization, the incident field projection is nearly perpendicular to the surface polariton wavevector. Since the angle of incidence in these cases is very shallow, approximately 10 to 11°, the incident field component normal to the surface in the p polarized case is a very small fraction of the total. Thus the coupling is mainly dependent upon the collinearity of the incident field component parallel to the surface and that of the longitudinal component of the surface polariton field. As can be seen from the schematic, this collinearity is almost nonexistent with an azimuth of $\phi = 5^\circ$. Hence, the large differences in the reflectance minimums for the s and p polarizations of incident fields.

At an angle of incidence of $\theta = 90^\circ$, the projection of the incident wavevector, k_{\parallel} , would reach the light line, $\omega = ck$. This extremum cannot, of course, be reached in practicality but may only be approached. The azimuthal angle can be made large enough so that the resonant condition cannot be met at any angle of incidence. In these cases, k_{\parallel} cannot be made large enough to position any of the reciprocal lattice vectors such that the coupling produces a resonant evanescent wave.

In the geometry under investigation, this limiting case occurs at approximately 29° of azimuth. In order to validate the perturbation theory more fully, reflectance was scanned versus the angle of incidence at an angle of azimuth of 25° for the single case of $h_1 = 7.4$ nm. These calculations were performed using both s and p polarization for the incident light. The results from these calculations are presented graphically in Figures 9 and 10 on the following two pages. The numerical comparisons of the exact

TABLE 2
 PERCENTAGE DIFFERENCES OF EXACT AND PERTURBATION
 RESULTS FOR $\phi = 25^\circ$ AZIMUTH

h_1 (nm)	Pol.	ξ_0	ξ_0	$\Delta\xi$	$\Delta\kappa$	$\Delta\delta$	$\Delta\kappa_g$
7.4	s	0.739	45.7	1.3%	0.45%	2.2%	0.45%
7.4	p	0.776	41.5	9.1%	0.03%	19.%	0.05%

and perturbation results are given in Table 2. Although the percentage errors for the reflectance minimum and enhancement peak are somewhat large for the case of p polarized incidence, the perturbation predictions have angular errors that are less than 0.1%.

Figure 11 is a schematic of the wavevector coupling for the 25° azimuth geometry. The magnitude of the reflectance minima are very nearly the same for the s and p incident polarization cases. Unlike the 5° azimuth cases, the angle

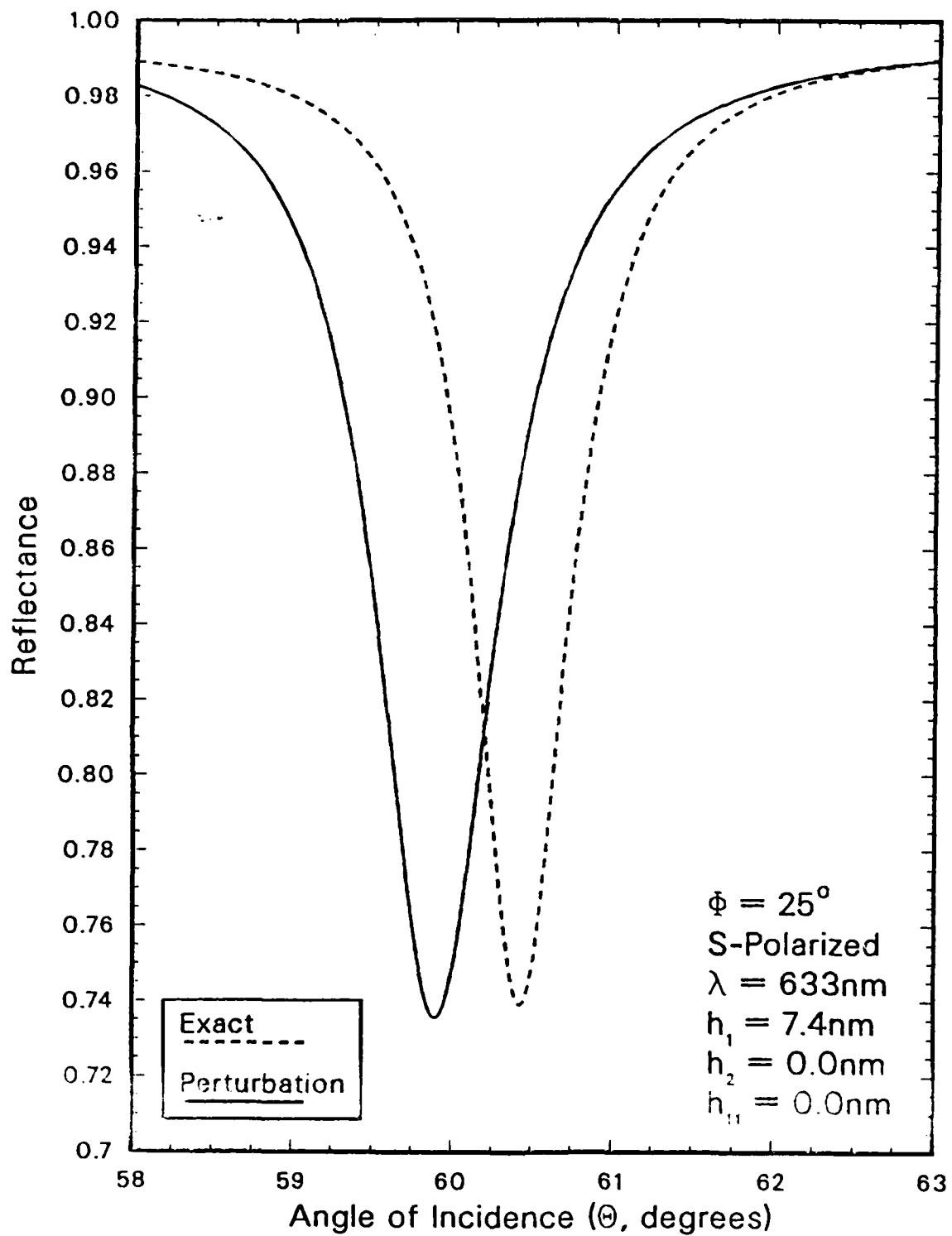


Figure 9. Reflectance Curves for S Polarized Light at 25° Azimuth and h_1 at 7.4 nm.

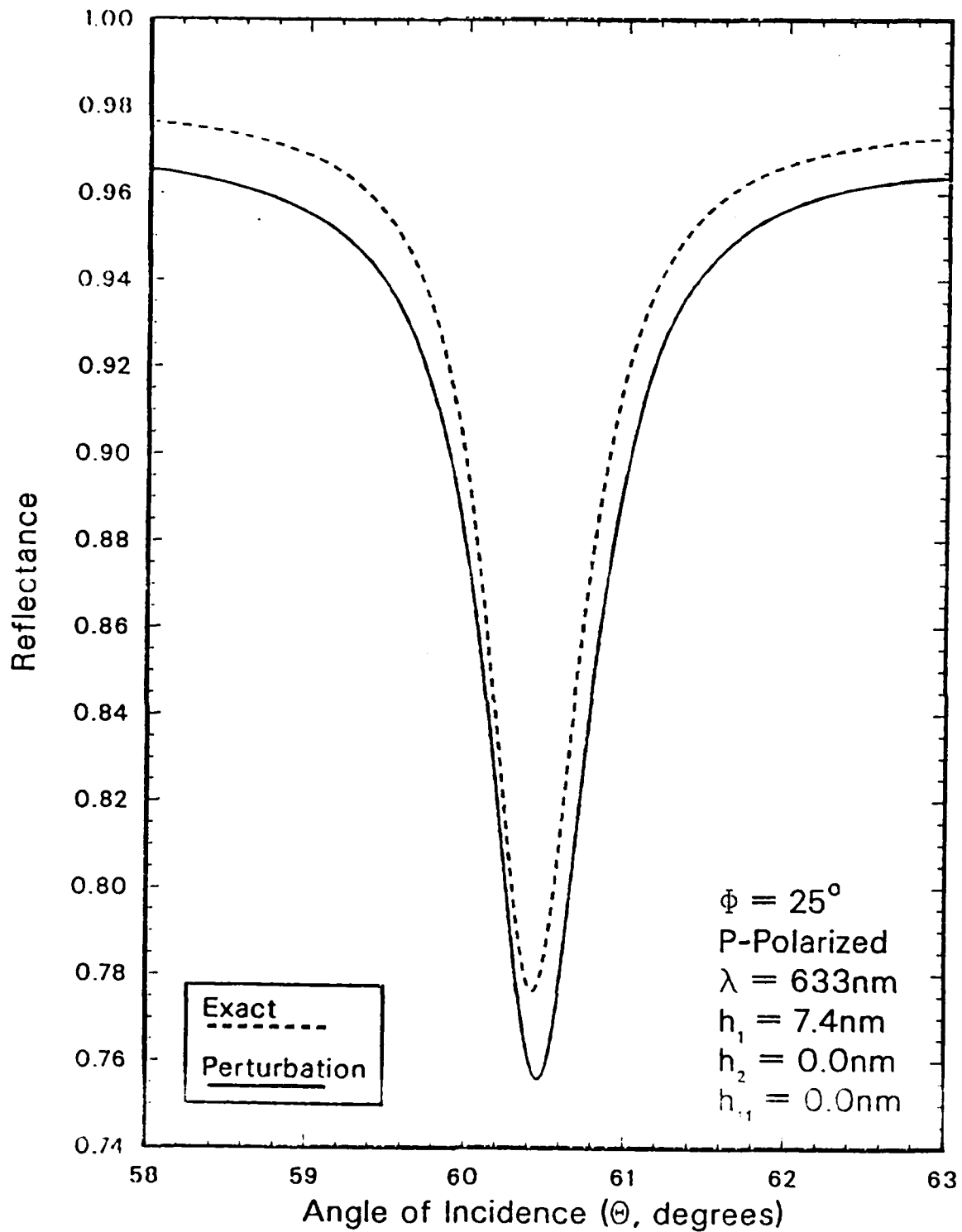


Figure 10. Reflectance Curves for P Polarized Light at 25° Azimuth and h_1 at 7.4 nm.

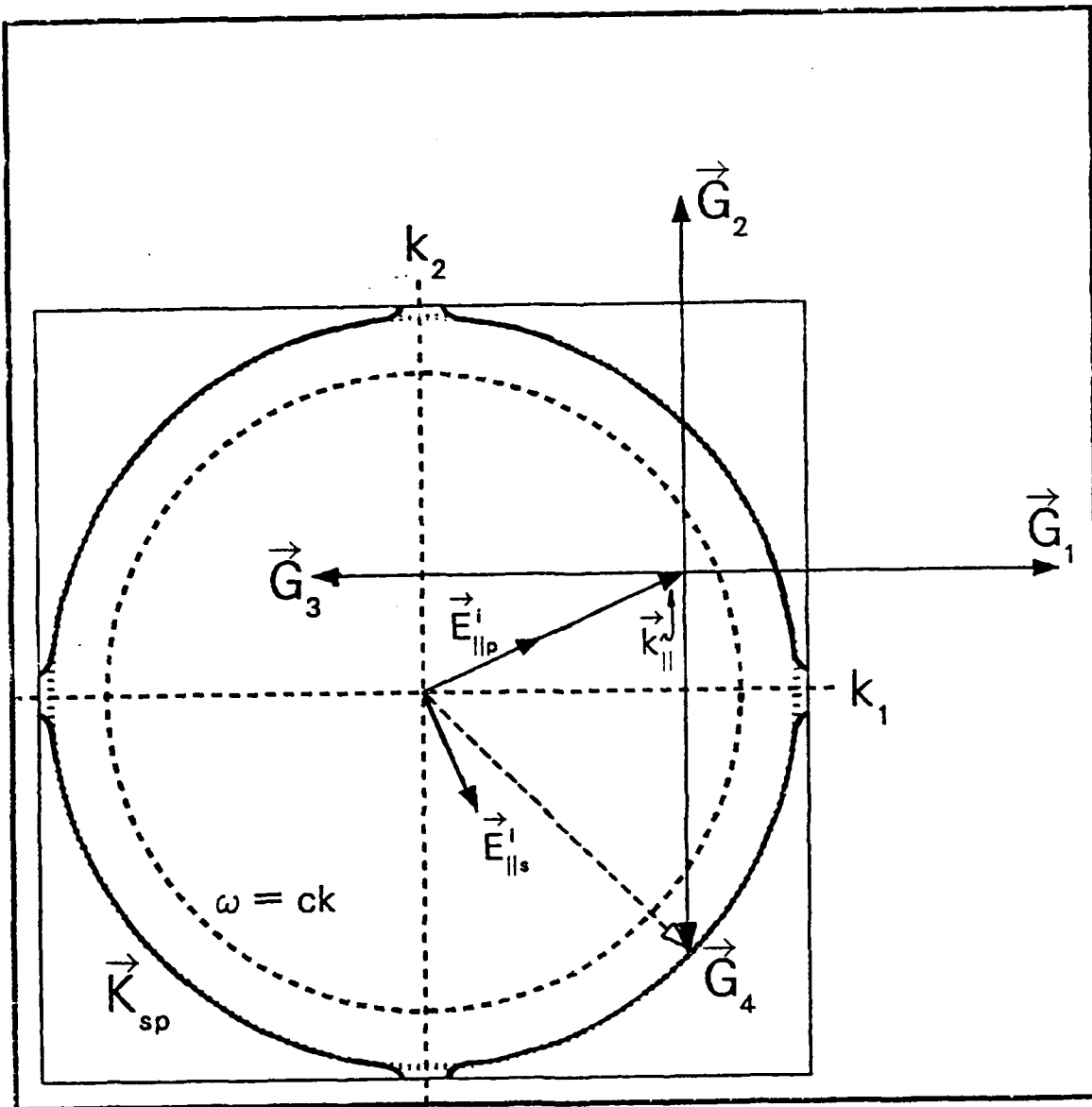


Figure 11. Schematic of Wavevector Coupling at 25° Azimuth.

of incidence in these cases is rather large, approximately 60.5°, and the p polarized incident wave has a large field component normal to the surface. This, together with the increased collinearity of its parallel component with the longitudinal surface polariton field component, accounts for

the smaller reflectance minimum with p polarized incidence at an azimuth of 25° vice 5° . The s polarized incident wave, totally dependent for resonant coupling on collinearity with the longitudinal surface polariton field component, has a significantly larger reflectance minimum at 25° azimuth than at 5° azimuth. Hence, the rather small differences in reflectance minimums for the s and p incident polarizations in the $\phi = 25^\circ$ case.

B. CONVERGENCE OF EXACT THEORY CALCULATIONS

As discussed in section B of Chapter III, the numerical implementation of the exact theory requires truncation of the infinite series of equations (9) and (29a) in calculating the values of the Rayleigh coefficients and $\rho(\alpha|\vec{G})$. If the height coefficient in the surface profile function for the cross term, h_{11} , is sufficiently small, then retention of a single term of the series in equation (29a) will suffice. In all of the cases presented within this chapter, the cross term is absent, $h_{11} = 0$, and truncation of this series was not a factor in convergence of the calculations.

Convergence of the calculations with the exact theory here, then, is solely dependent upon the validity of the Rayleigh Hypothesis for the cases treated. The validity of the Rayleigh Hypothesis is, in turn, dependent upon the corrugation strength. Convergence checks were conducted for

the maximum corrugation strengths used in each case of polarization and azimuth combination to ensure the validity of the exact calculations.

As discussed in section B of Chapter III, truncation of the doubly infinite set of linear equations from equation (9) results in elimination of reciprocal lattice vectors outside a chosen range of indices. Recalling the notational definitions from this discussion, the truncation, with the linear equations in matrix form, results in a matrix of dimensions $2N^2 \times 2N^2$ and the reciprocal lattice vectors retained have indices given by equation (30).

All results presented are for $N = 7$. Convergence checks were conducted by using N as 5, 7, 9, and 11 in successive

TABLE 3
SUMMARY OF CONVERGENCE CHECK RESULTS FOR
REFLECTANCES AT OFF-NORMAL INCIDENCE

h_1 (nm)	Pol.	ϕ	$\Delta R_{5,7}$	$\Delta R_{7,9}$	$\Delta R_{9,11}$
14.8	s	5°	4.9×10^{-3}	3.9×10^{-5}	1.0×10^{-6}
7.4	p	5°	3.5×10^{-6}	2.1×10^{-8}	0×10^{-9}
7.4	s	25°	5.2×10^{-5}	2.9×10^{-7}	1.0×10^{-9}
7.4	p	25°	5.2×10^{-5}	3.0×10^{-7}	2.0×10^{-9}

calculations of the resonant case, i. e., at the reflectance minimum. Table 3 is a summary of the differences in the minimum reflectances. The subscripts on the labels indicate

the successive values of N used in the calculations. Since the reflectance values are already normalized with respect to unity, the accuracies achieved may be read directly from the table. From the values in the table it can be seen that truncation to a matrix of dimensions 98×98 with $N = 7$ gives accuracies to at least one part in two thousand for the reflectance minimum.

TABLE 4
SUMMARY OF CONVERGENCE CHECK RESULTS FOR
ENHANCEMENTS AT OFF-NORMAL INCIDENCE

h_1 (nm)	Pol.	ϕ	$\Delta \epsilon_{5,7}$	$\Delta \epsilon_{7,9}$	$\Delta \epsilon_{9,11}$	$\epsilon_{0,11}$
14.8	s	5°	13.723	1.846	0.308	439.4
7.4	p	5°	2.4×10^{-2}	2.1×10^{-3}	1.8×10^{-4}	3.350
7.4	s	25°	0.339	2.8×10^{-2}	2.4×10^{-3}	45.65
7.4	p	25°	0.175	2.3×10^{-2}	2.0×10^{-3}	39.18

Table 4 is a summary of the differences in enhancement peaks in the convergence checks. Since these are not normalized differences, the peak enhancement value for the $N = 11$ calculation is included in the table for each case. Using this value for a normalization factor, the accuracies achieved for the enhancements with $N = 7$ are at least to one part in fifteen hundred.

V. VALIDATION NEAR NORMAL INCIDENCE

In comparing the results of perturbation theory calculations around normal incidence with those of the exact theory, several cases of incidence geometry were investigated. Scans of reflectance versus angle of incidence were performed for various surface profiles in attempting to obtain agreement between perturbation and exact results. Although the perturbation theory was unable to predict both reflectance and enhancement versus angle of incidence with an acceptable degree of accuracy for any single case, some utility in predicting bigrating efficiencies was established for limited cases of surface profile and incidence geometry. Additionally, a scan versus incident frequency was performed for a single bigrating profile.

A. RESULTS NEAR NORMAL INCIDENCE VERSUS ANGLE OF INCIDENCE

As before, the values of $\lambda = 633.00$ nm and $\alpha = 615.47$ nm were held fixed and investigations around normal incidence were commenced using the optimum coupling value of $h_1 = 7.4$ nm with h_2 and h_{11} both at zero. Since the perturbation theory gave reliable results at off-normal incidence for this geometry, it was expected that some degree of reliability could be expected near normal

incidence as a benchmark for validation. This was not found to be the case. For this reason, changes in calculation parameters for the perturbation theory which might improve agreement with exact calculations were sought.

In all previous perturbation calculations, the four Rayleigh coefficients which were taken to be the most significant evanescent wave amplitude coefficients were $A_{\parallel}(1,0)$, $A_{\parallel}(0,1)$, $A_{\parallel}(-1,0)$, and $A_{\parallel}(0,-1)$. This set of evanescent wave Rayleigh coefficients will henceforth be referred to as the canonical coefficients. These coefficients, along with the specular beam coefficients $A_{\perp}(0,0)$ and $A_{\parallel}(0,0)$, constitute the six important terms referred to in the development of the perturbation theory in subsection B.2 of Chapter II. Inspections of printouts for the Rayleigh coefficients from exact theory calculations revealed that several evanescent amplitudes other than the canonical coefficients were of significant magnitude. In order to obtain better prediction behaviour from the perturbation theory, the choice of which four evanescent wave coefficients are included in the six important terms was modified. The choices for the four terms included was dependent on the particular case of incidence geometry. The specific choices made for these terms, which will henceforth be termed the corrected choice of coefficients, will be discussed later.

Figures 12 through 15 on the following four pages are graphical representations of the reflectance versus angle of incidence for the perturbation and exact theory calculations for s and p polarization at azimuths of $\phi = 0^\circ$ and $\phi = 90^\circ$. Table 5 below is a quantitative comparison of these results using the same parameters for comparison as developed in the preceding chapter. In this table, the different choices

TABLE 5
 PERCENTAGE DIFFERENCES OF EXACT AND PERTURBATION
 RESULTS FOR $h_1 = 7.4$ nm NEAR NORMAL INCIDENCE

ϕ	Pol.	Pert.	ξ_0	ξ_0	ΔR	Δk	$\Delta \epsilon$	Δk_z
0°	s	canon.	0.003	40.4	.53%	3.4%	34.%	3.3%
0°	s	corr.	0.003	40.4	1.3%	3.1%	11.%	3.4%
0°	p	canon.	0.050	273.	11.%	0.17%	68.%	0.12%
0°	p	corr.	0.050	273.	47.%	0.02%	50.%	0.09%
90°	s	canon.	0.003	40.4	.63%	2.5%	6.4%	2.6%
90°	s	corr.	0.003	40.4	1.3%	3.1%	11.%	3.4%
90°	p	canon.	0.050	273.	12.%	0.15%	80.%	0.07%
90°	p	corr.	0.050	273.	47.%	0.02%	50.%	0.09%

for the evanescent wave Rayleigh coefficients are indicated in the column headed Pert., for perturbation, as either canonical or corrected. From this table and from Figures 12 through 15, it can be seen that the perturbation theory is unable to reliably predict results for this bigrating

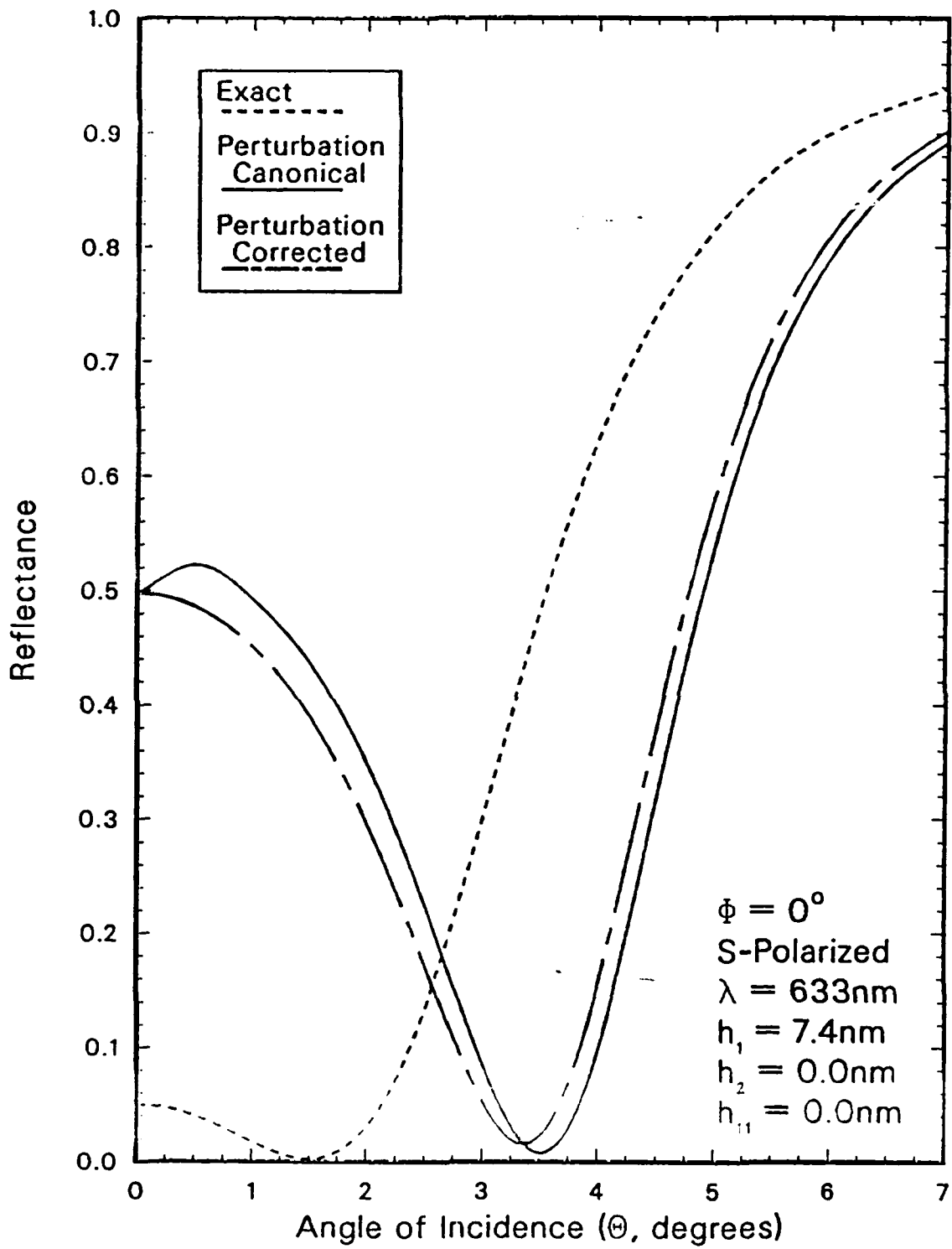


Figure 12. Reflectance Curves for $h_1 = 7.4 \text{ nm}$ Near Normal Incidence with 0° Azimuth and S Polarization.

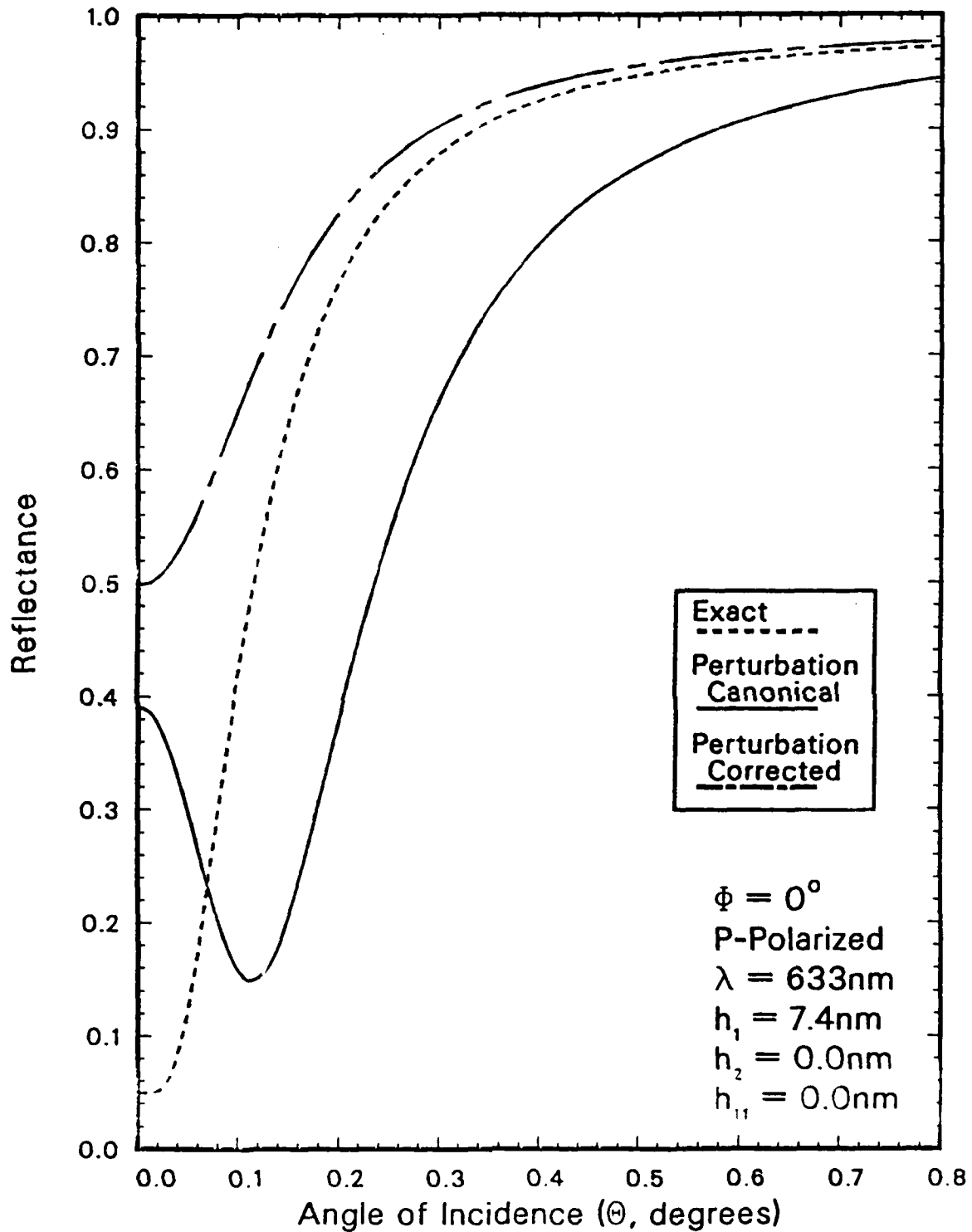


Figure 13. Reflectance Curves for $h_1 = 7.4$ nm Near Normal Incidence with 0° Azimuth and P Polarization.

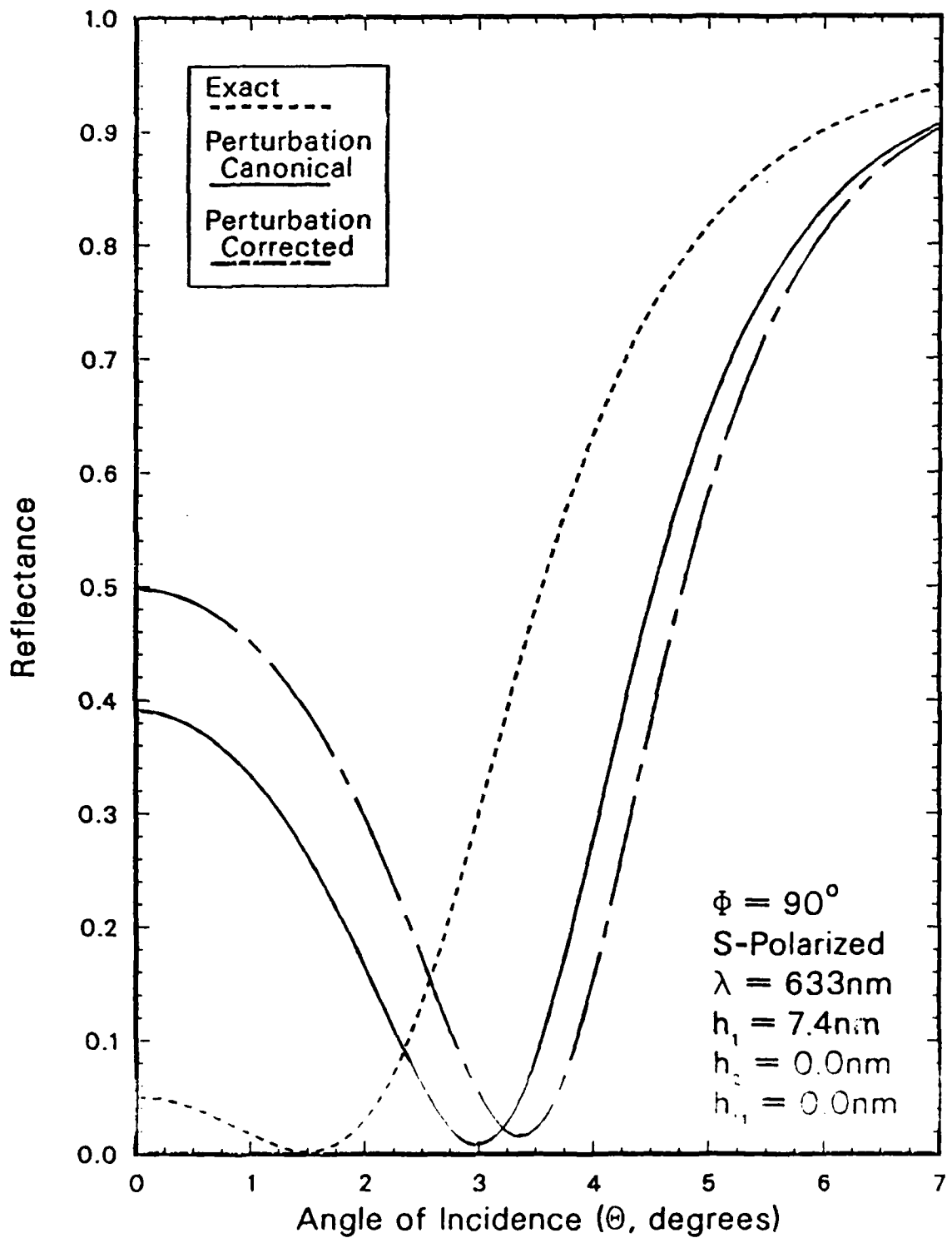


Figure 14. Reflectance Curves for $h_1 = 7.4 \text{ nm}$ Near Normal Incidence with 90° Azimuth and S Polarization.

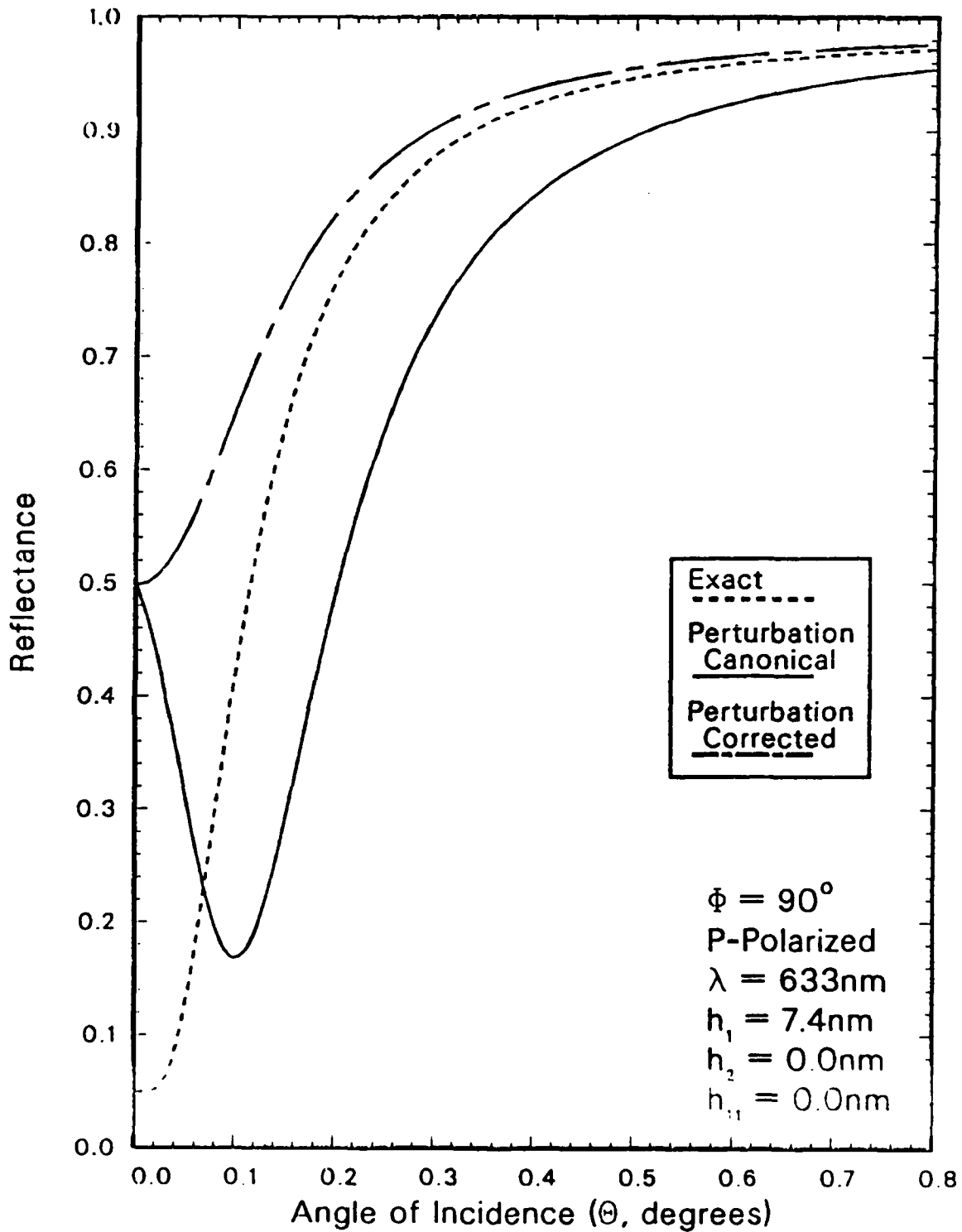


Figure 15. Reflectance Curves for $h_1 = 7.4$ nm Near Normal Incidence with 90° Azimuth and P Polarization.

geometry. In particular it should be noted in the figures that the magnitude of the reflectance dip at zero degrees ($\theta = 0.00001^\circ$) incidence is quite different in the perturbation and the exact theory curves. Although the errors in the angular location of the dip expressed in wavevector form are all less than 4%, reliance on the perturbation theory as a predictor of bigrating performance at normal incidence could lead to misconceptions of the pattern of bigrating efficiency around normal incidence.

In discussing the corrected choices of the evanescent wave Rayleigh coefficients, it is helpful to once again consider a schematic of the wavevector coupling. Figure 16 is such a schematic for the case of near normal incidence with s polarization. The wavevectors of the two resonantly stimulated evanescent waves are again depicted as dashed vectors without labels. As the angle of incidence is varied near $\theta = 0^\circ$, the wavevector $\vec{k}_\parallel + \vec{G}$ can be thought to move across the gap induced by the Brillouin zone boundary. The resonant condition is met when the reciprocal lattice vectors touch the constant frequency circle. At an azimuth of $\phi = 0^\circ$ with s polarization, there is no incident electric field component in the (1,0) and (-1,0) directions. Thus, the surface waves at \vec{G}_1 and \vec{G}_3 are not directly excited. Moreover, there is no first order coupling of the excited waves at \vec{G}_2 and \vec{G}_4 to the degenerate waves at \vec{G}_1 and \vec{G}_3 since the coupling coefficients $\tilde{\zeta}(\pm 1, \pm 1)$ (proportional to

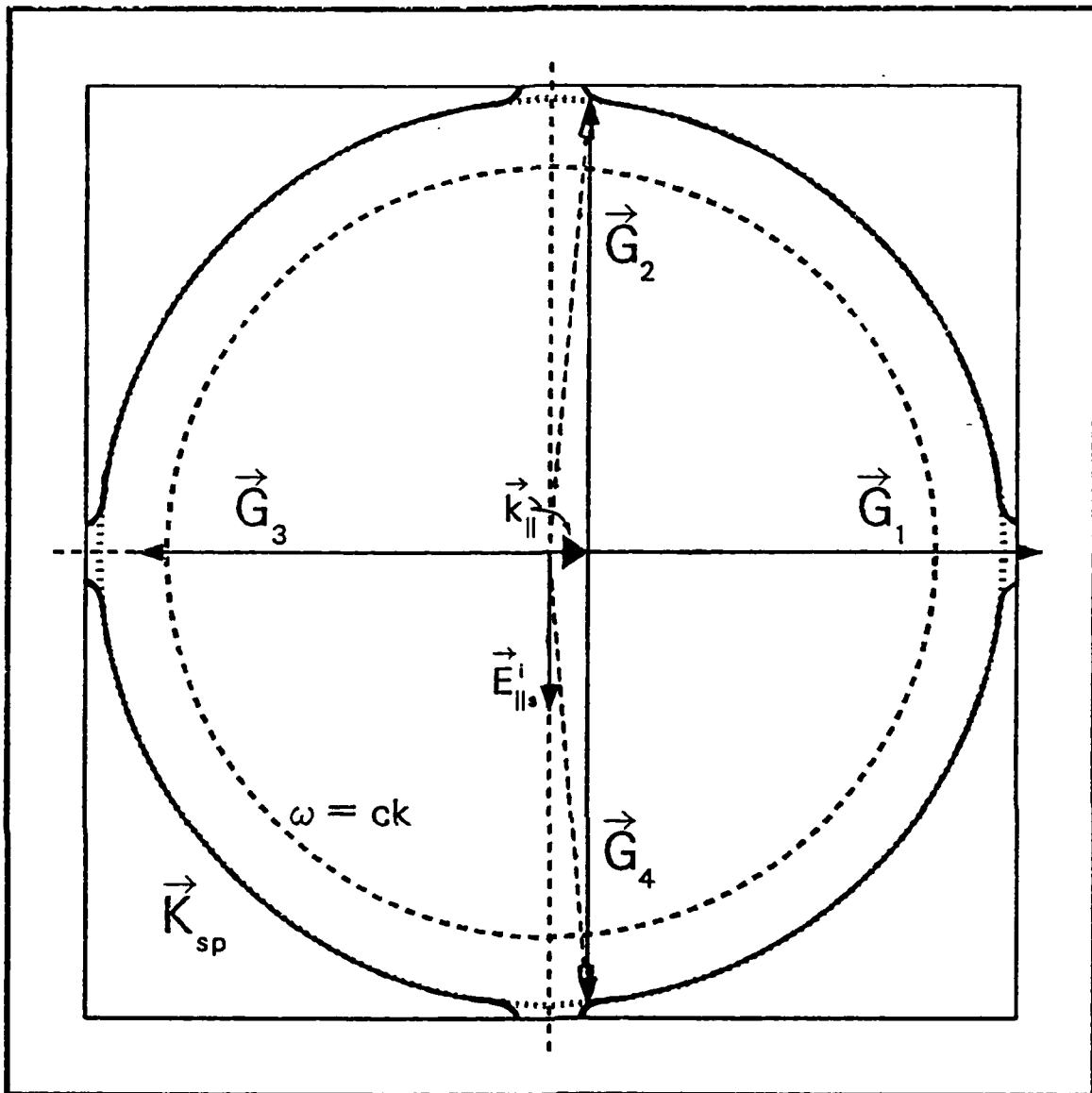


Figure 16. Schematic of Wavevector Coupling for S Polarization Near Normal Incidence.

h_{11}) are all zero for this surface profile. On the other hand, the excited waves at \vec{G}_2 and \vec{G}_4 do couple, to first order, through the reciprocal lattice vectors \vec{G}_i ($i = 1, 2, 3, 4$), to other waves not on the constant frequency circle. Thus a logical choice for the corrected set of

evanescent wave Rayleigh coefficients for this case is $A_{\parallel}(0,1)$, $A_{\parallel}(0,-1)$, $A_{\parallel}(0,2)$, and $A_{\parallel}(0,-2)$. With s polarization at an azimuth of $\phi = 90^\circ$, the incident field vector lies wholly along the $(1,0)$, $(-1,0)$ axis and the choice for the corrected coefficients in this case is $A_{\parallel}(1,0)$, $A_{\parallel}(-1,0)$, $A_{\parallel}(2,0)$, and $A_{\parallel}(-2,0)$.

It is obvious that the two cases of $\phi = 0^\circ$ and $\phi = 90^\circ$ azimuth are identical for either polarization. With s polarization, for example, the incidence geometry pictured in Figure 16 is merely rotated 90° for the latter case. Indeed, a close comparison of the exact results for the two azimuth cases for either polarization showed that the reflectance curves are identical. There are, however, slight differences in perturbation theory results for each of the two azimuth cases for both s and p polarization. It is for this reason that the two azimuth cases were examined. Validity of the exact calculations has thus been reaffirmed and a further test of the perturbation theory has been achieved.

Figure 17 on the following page is a schematic of the wavevector coupling with p polarized incidence. At this point it is necessary to note that the resonance condition is not sharp. As can be seen in all the reflectance curves, there is a degree of broadening around the theoretical matching condition. The breaks in the constant frequency circle are narrow enough in this geometry that the resonant

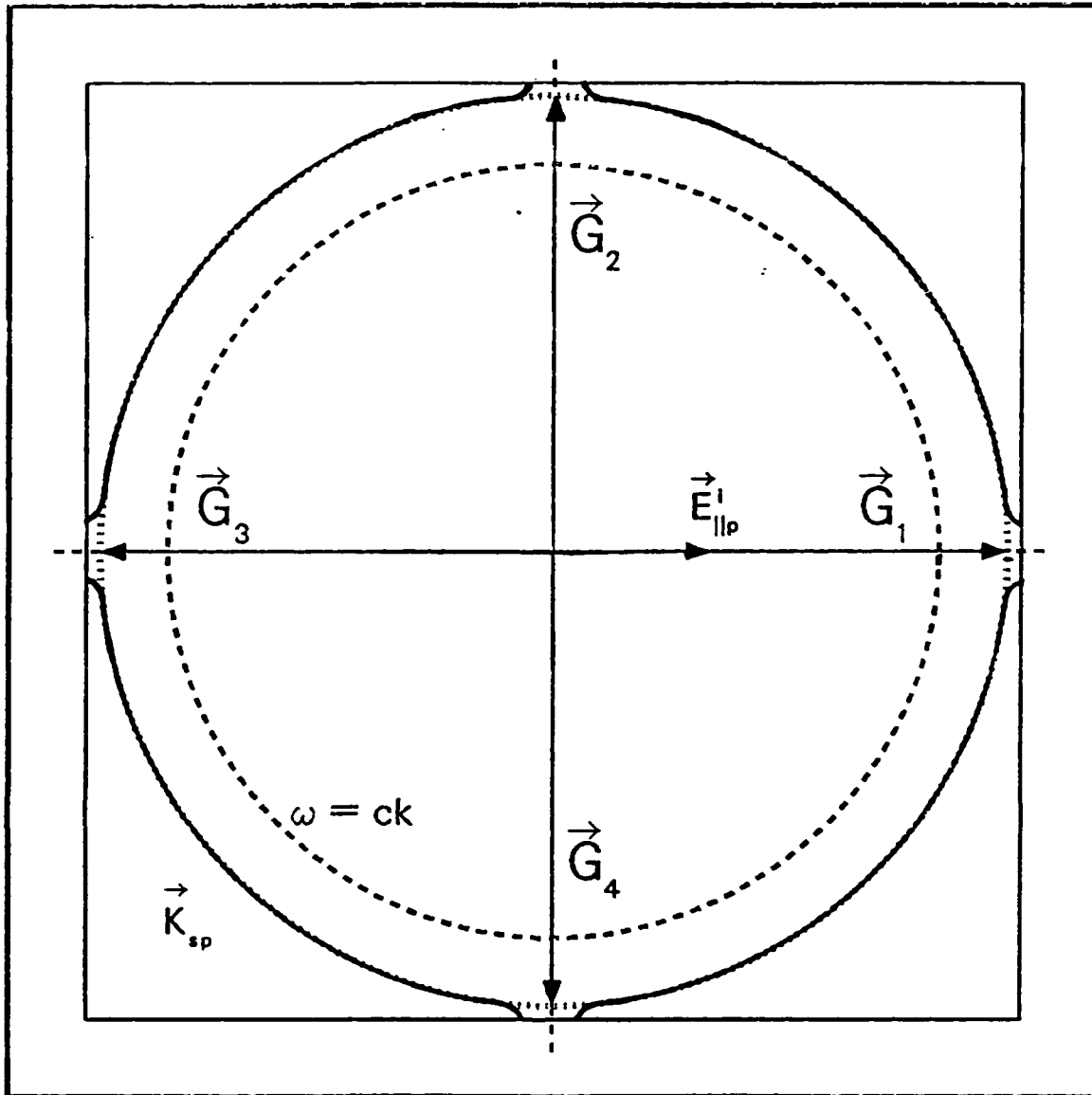


Figure 17. Schematic of Wavevector Coupling for P Polarization Near Normal Incidence.

reflectance dips overlap across the breaks⁷. It is this overlap that gives rise to the reflectance dips in the p

⁷As discussed earlier, these breaks in the constant frequency circle are caused by the birefringent lattice and occur at the intersections with the Brillouin zone boundary.

polarized geometry at normal incidence. The exact curves for the s polarized cases graphically indicate this overlap characteristic. Referring to the schematic for the s polarized case in Figure 16, as the angle of incidence is increased from zero, the Brillouin zone boundary is scanned from the center of the break in the constant frequency circle ($\theta = 0^\circ$ on Figures 12 and 14), where the tails of the polaritons strongly overlap, to the edge of the break ($\theta = 1.5^\circ$ on Figures 12 and 14), where the resonance condition is fully met. Thus, there is very low reflectance at $\theta = 0^\circ$ but the minimum reflectance occurs at $\theta = 1.5^\circ$. Returning to the schematic in Figure 17 for p polarized incidence, as the angle of incidence is increased from zero, the scan passes right through the center of the break in the constant frequency circle and thus crosses the center of the polariton tail overlap. Therefore there is a minimum reflectance condition at $\theta = 0^\circ$ in Figures 13 and 15. Note that the reflectance at $\theta = 0^\circ$ for s polarization (Figures 12 and 14) is identical to that at $\theta = 0^\circ$ for p polarization (Figures 13 and 15): both correspond to exactly the same excitation at the center of the break in the constant frequency circle.

At $\phi = 0^\circ$ azimuth with p polarization, the incident electric field vector lies along the (1,0), (-1,0) axis of the lattice. Consequently, there is no first order coupling of the incident wave into a surface polariton with the

$\vec{C}(0,1)$ and the $\vec{C}(0,-1)$ reciprocal lattice vectors. A corrected choice for the set of evanescent wave Rayleigh coefficients in this case, then, is identical to that for the $\phi = 90^\circ$, s polarized case, i. e., $A_{\parallel}(1,0)$, $A_{\parallel}(-1,0)$, $A_{\parallel}(2,0)$ and $A_{\parallel}(-2,0)$. Similarly, the corrected choice for the set of coefficients for $\phi = 90^\circ$ azimuth with p polarization is identical to that for the $\phi = 0^\circ$, s polarized case.

The preceding discussion has served to illustrate much of the physics involved in the coupling mechanisms for cases near normal incidence. However, as can be seen from the reflectance curve comparisons and from Table 5, there is very little improvement in the perturbation theory predictions with the corrected choice of coefficients over those with the canonical coefficients.

There are three basic assumptions in the foundation of the perturbation theory. The first is the validity of the Rayleigh hypothesis in the particular cases being investigated. This assumption is also inherent in the exact theory and is taken to be valid on the strength of the rapid convergence of the exact calculations. The second assumption is that a first order truncation of the expansion for $\exp[-i\alpha\zeta]$ yields a valid approximation for the expansion. As discussed in the previous chapter, this assumption is taken to be valid for values of $\alpha\zeta_{\max} < 1$, as evidenced by the results for calculations at off-normal

incidence. The third assumption of the first order perturbation theory is that the most important evanescent waves in the Bloch sum for the surface polariton are the four which are, on the flat surface, degenerate and whose wavevectors are connected by reciprocal lattice vectors; i. e., those evanescent terms whose wavevectors are at the intersection of two Brillouin zone boundaries. In the bigrating profiles considered up to this point, the values for h_2 and h_{11} have been held at zero. The reason for the poor performance of the perturbation theory near normal incidence with such a surface profile, even when $\alpha\zeta_{\max}$ is less than one, is due to the fact that these terms are not present in the surface profile. For these cases, the third premise of the perturbation theory is not valid, since the coupling coefficients actually vanish among the four evanescent waves considered as important. Thus, there are other terms in the Bloch sum that are of the same order of magnitude as these four. In these cases, the gaps in the dispersion curves, at the Brillouin zone boundaries at $\vec{k} = \vec{G}_1, \vec{G}_2, \vec{G}_3,$ and $\vec{G}_4,$ and the breaks in the constant frequency circle are due to second order coupling of the four zone boundary waves³. Thus, the use of a first order

³The breaks in the constant frequency circle, depicted schematically in the wavevector coupling figures, are responsible for the shift of the reflectance minimum from $\theta = 0^\circ$ to $\theta = 1.5^\circ$ in Figures 12 and 14.

approximation for treating the resonant excitation of modes near the gap at \vec{G}_1 , \vec{G}_2 , \vec{G}_3 , and \vec{G}_4 in such cases is inappropriate. An increase in the h_{11} cross term, then, would allow first order coupling between these four terms. In this manner, the magnitudes of the four evanescent waves considered as important in the perturbation theory, and which are retained in all portions of the perturbation calculations, could be increased over those of all the other terms in the Bloch wave sum. Furthermore, the gaps at \vec{G}_1 , \vec{G}_2 , \vec{G}_3 , and \vec{G}_4 could become first order effects. Thus, by increasing the cross term, the basic premises of the perturbation theory might once again be valid.

Cases of surface profiles with the h_{11} cross term increased from zero to 2.5 nm were investigated for comparisons between exact and perturbation results. The h_1 term was decreased to 6.0 nm to avoid making $\alpha\zeta_{\max}$ greater than one, and calculations for s and p polarized incidence with $\phi = 0^\circ$ azimuth were executed. The reflectance curves for these calculations are presented in Figures 18 through 23 on the following six pages. Table 6 on the seventh page following is a listing of the quantitative comparisons of the perturbation and exact results for these cases.

A definite trend of improvement for the perturbation theory predictions can be noted in these results. Particularly in a comparison of the results for the surface profiles of $h_1 = 4.5$ nm with and without the cross term

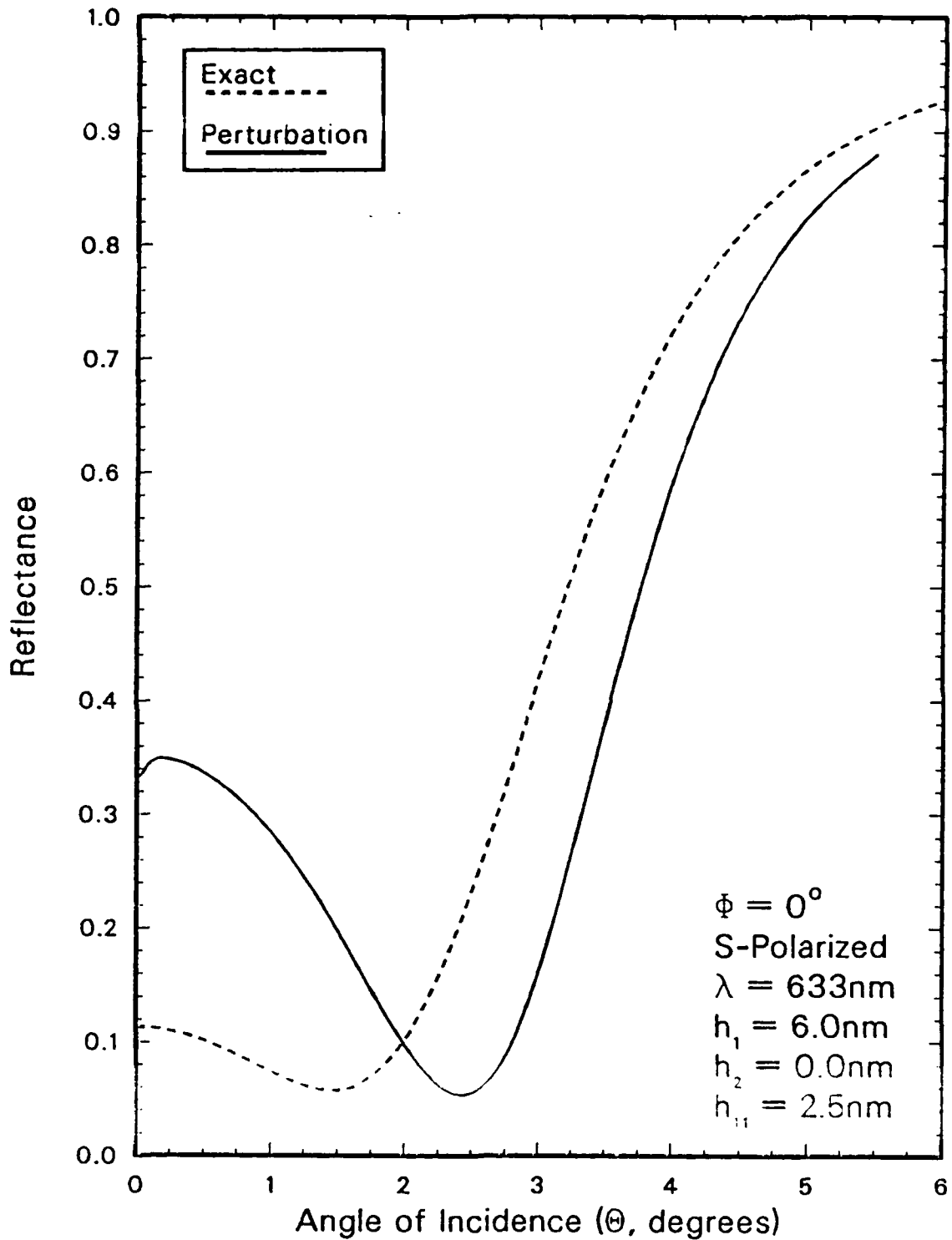


Figure 18. Reflectance Curves for $h_1 = 6.0$ nm and $h_{11} = 2.5$ nm with S Polarization.

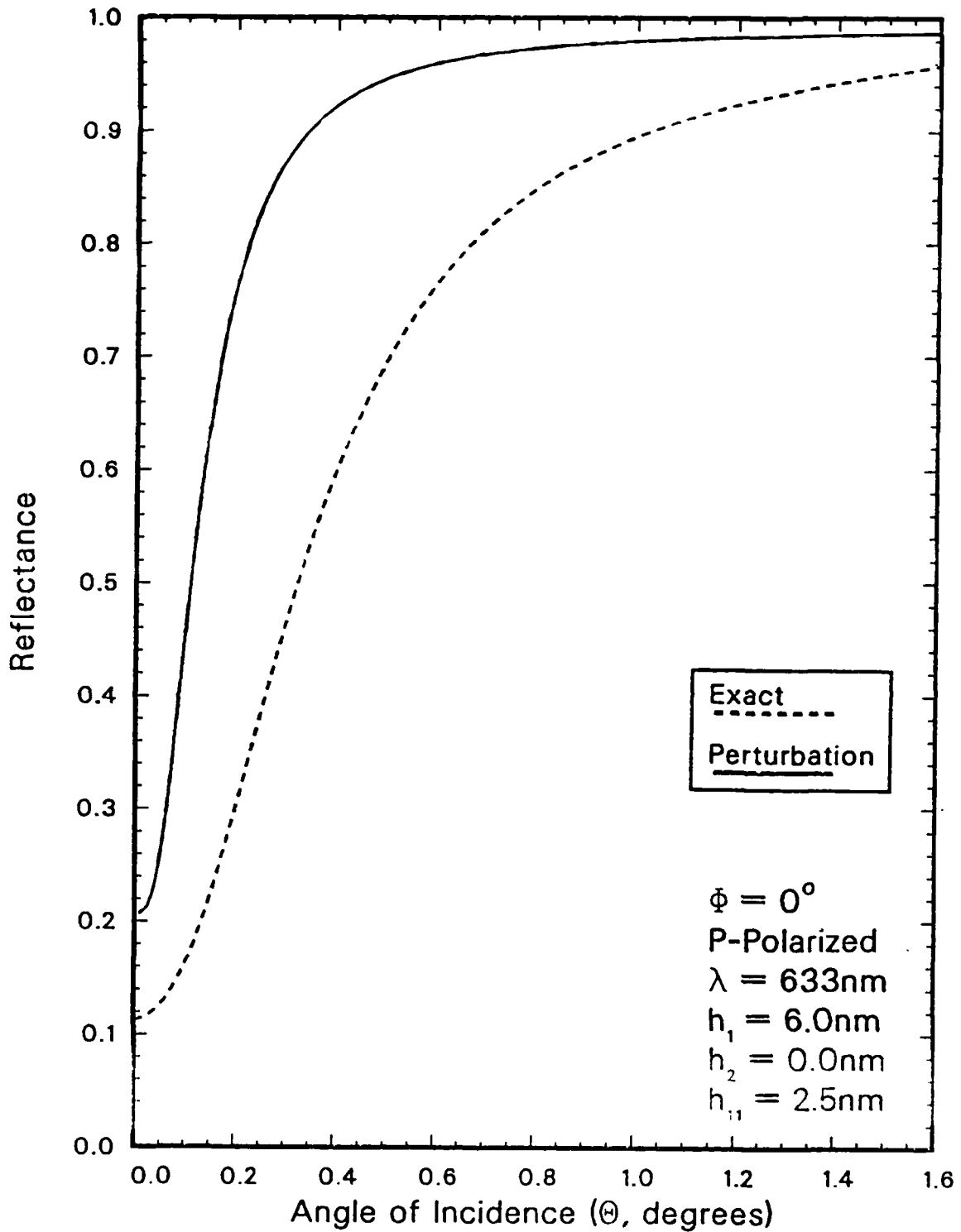


Figure 19. Reflectance Curves for $h_1 = 6.0 \text{ nm}$ and $h_{11} = 2.5 \text{ nm}$ with P Polarization.

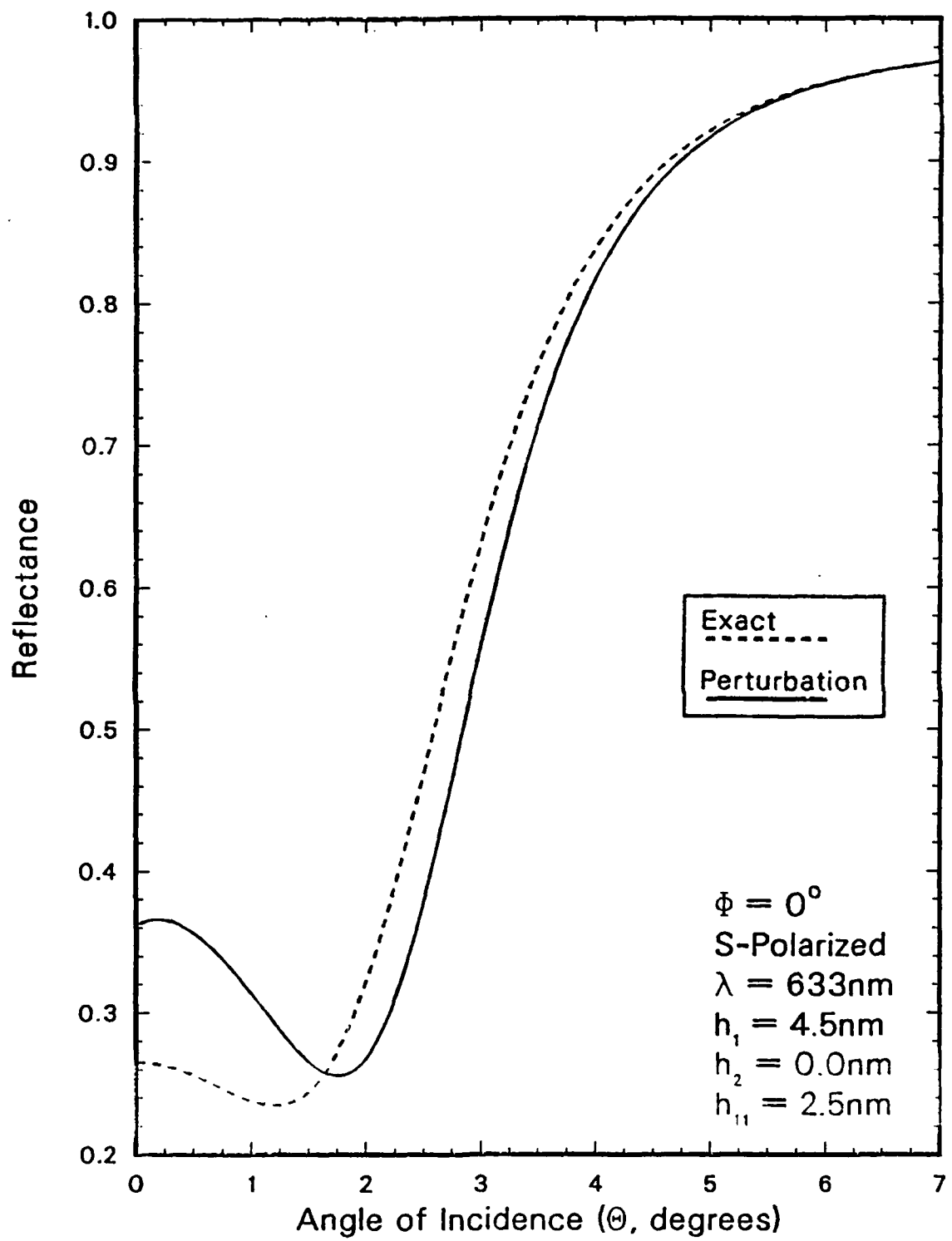


Figure 20. Reflectance Curves for $h_1 = 4.5 \text{ nm}$ and $h_{11} = 2.5 \text{ nm}$ with S Polarization.

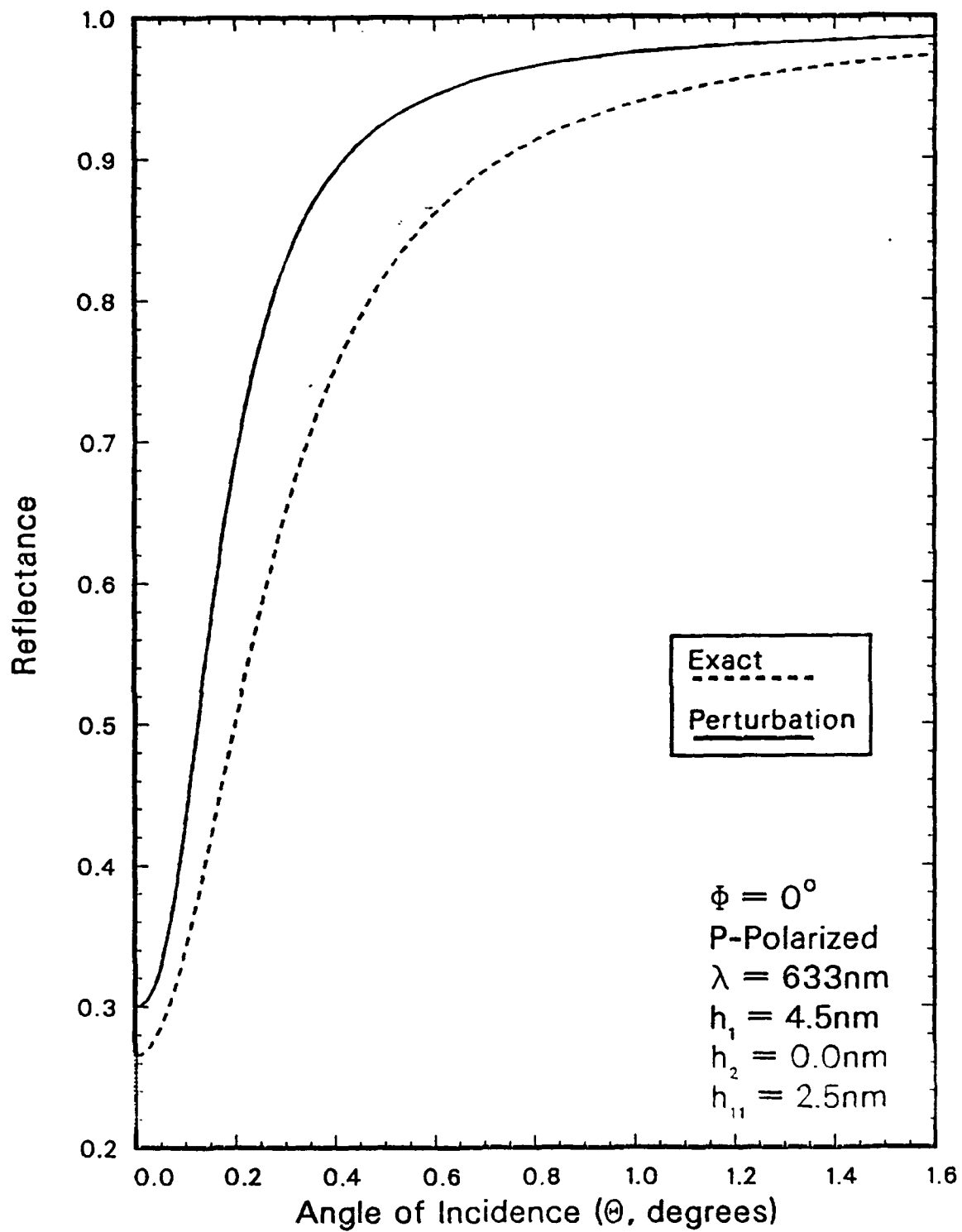


Figure 21. Reflectance Curves for $h_1 = 4.5 \text{ nm}$ and $h_{11} = 2.5 \text{ nm}$ with P Polarization.

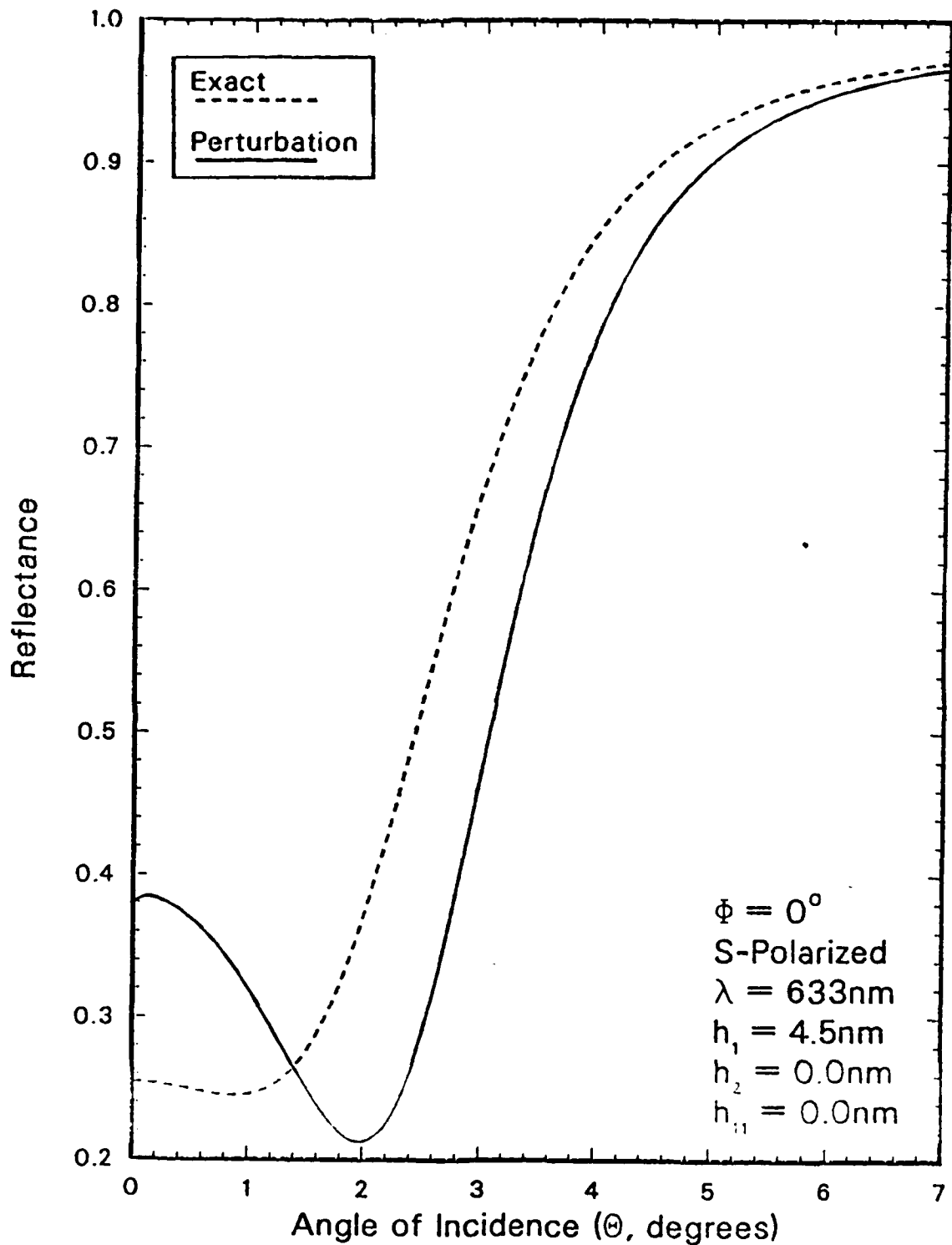


Figure 22. Reflectance Curves for $h_1 = 4.5 \text{ nm}$ and $h_{11} = 0 \text{ nm}$ with S Polarization.

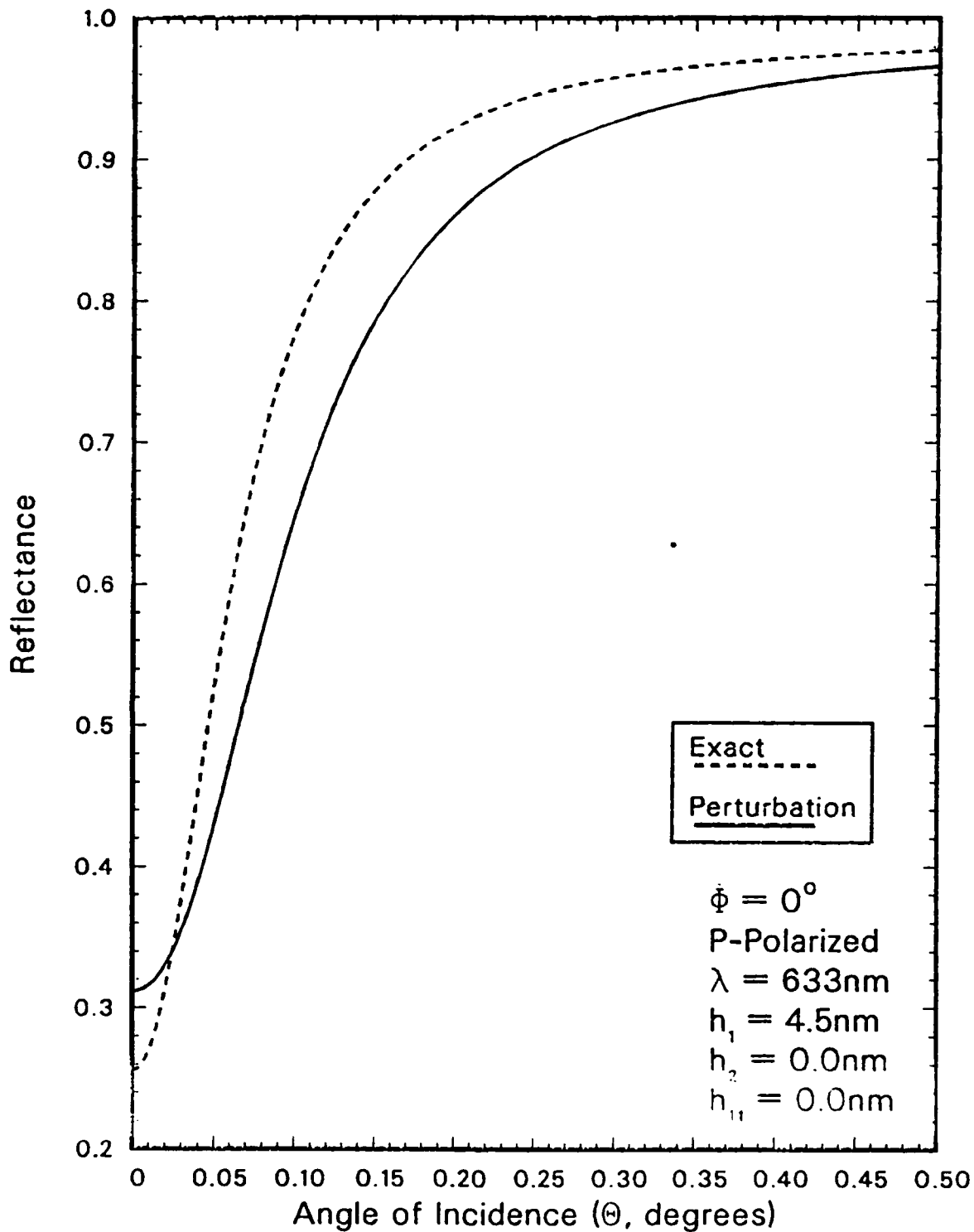


Figure 23. Reflectance Curves for $h_1 = 4.5 \text{ nm}$ and $h_{11} = 0 \text{ nm}$ with P Polarization.

TABLE 6

PERCENTAGE DIFFERENCES OF EXACT AND PERTURBATION
RESULTS FOR CROSS TERM RUNS AT $\phi = 0^\circ$ AZIMUTH

h_1	h_{11}	Pol.	ξ_0	ξ_0	$\Delta\xi$	$\Delta\kappa$	$\Delta\epsilon$	$\Delta\kappa_\epsilon$
6.0nm	2.5nm	s	0.057	37.6	.40%	1.6%	146.%	2.1%
6.0nm	2.5nm	p	0.113	276.	11.%	.00%	104.%	.31%
4.5nm	2.5nm	s	0.235	29.7	2.7%	.92%	28.%	.56%
4.5nm	2.5nm	p	0.265	192.	4.8%	.00%	42.%	.17%
4.5nm	0.0nm	s	0.245	28.9	4.3%	1.8%	31.%	1.9%
4.5nm	0.0nm	p	0.254	179.	7.6%	.00%	56.%	.03%

present. Though further investigations were not carried out in this area, one may surmise that the perturbation theory would yield more accurate predictions for surface profiles in which the cross term was an increasingly important factor.

B. RESULTS AT NORMAL INCIDENCE VERSUS FREQUENCY

The surface profile for which the reflectance versus angle of incidence near normal incidence were predicted most reliably by the perturbation theory, i. e., $h_1 = 4.5$ nm, $h_2 = 0$ nm, and $h_{11} = 2.5$ nm, was used to test the perturbation theory predictions for reflectance and enhancement versus incident frequency. Equivalently, this is a scan of the reflectance and enhancement versus incident photon energy, $\hbar\omega$. The reflectance curves for these

calculations are presented in Figures 24 and 25 on the following two pages. Table 7 is a listing of the quantitative comparisons of the perturbation and exact theory results. The quantities used here for the reflectance

TABLE 7
PERCENTAGE DIFFERENCES OF EXACT AND PERTURBATION
RESULTS VERSUS INCIDENT PHOTON ENERGY

h_1	h_{11}	Pol.	ϵ_0	ϵ_0	$\Delta\epsilon$	ΔE	$\Delta\epsilon$	ΔE_g
4.5nm	2.5nm	s	0.234	29.8	2.0%	.02%	31.%	.04%
4.5nm	2.5nm	p	0.234	29.8	1.4%	.01%	14.%	.01%

and enhancement percentage differences are the same as those used in comparisons of the results versus angle of incidence. The differences for the incident photon energies at which minimum reflectance and maximum enhancement occur are expressed as simple percentage errors. The percentage error in the energies for the reflectance minima are denoted by ΔE and for the enhancement peaks by ΔE_g . From this table and from Figures 24 and 25, it can be seen that the perturbation theory results versus incident photon energy are appreciably better than those versus angle of incidence for the normal incidence cases.

The results versus incident photon energy are somewhat surprising in that the dispersion curve gap does not appear.

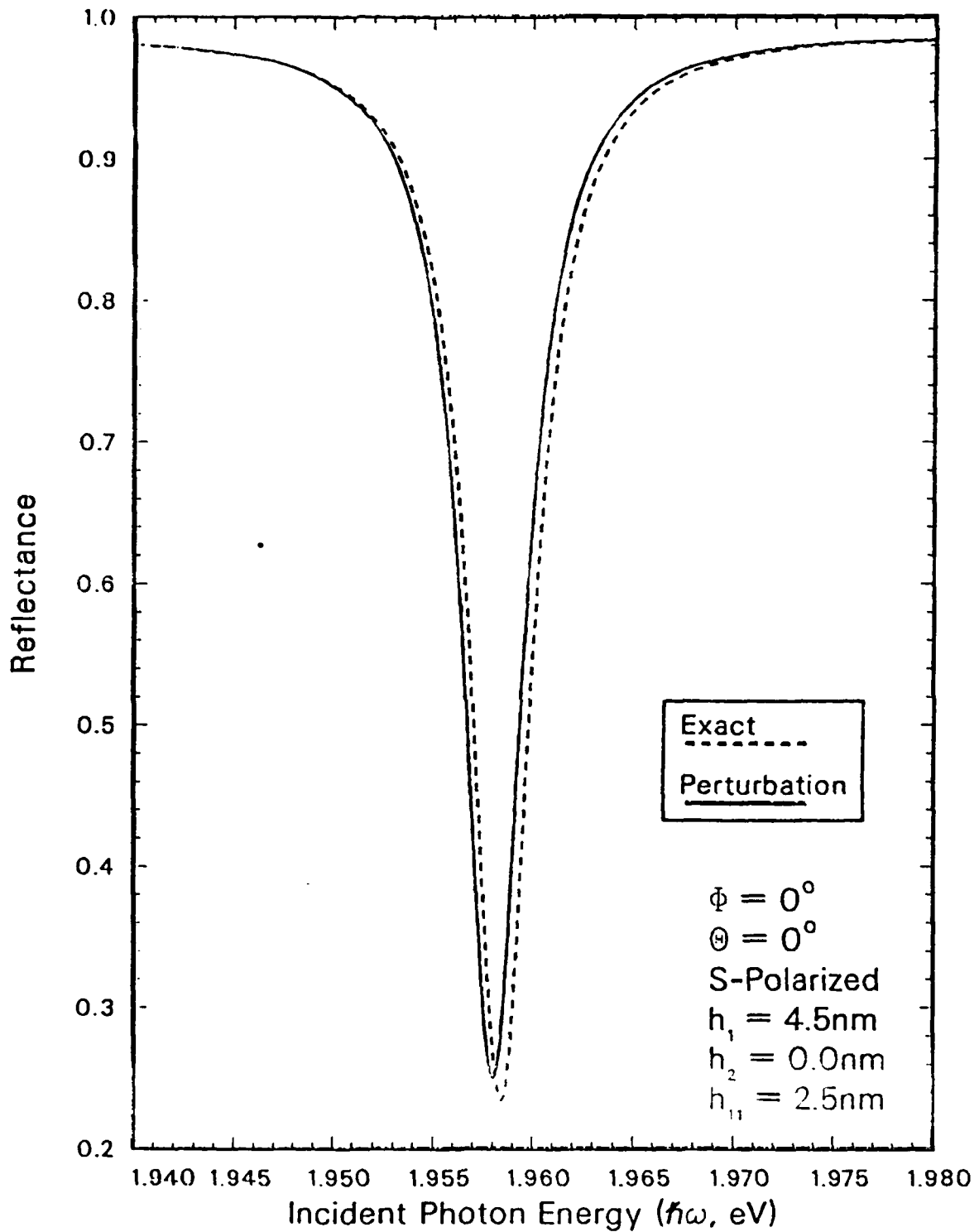


Figure 24. Reflectance Curves Versus Incident Photon Frequency for S Polarization.

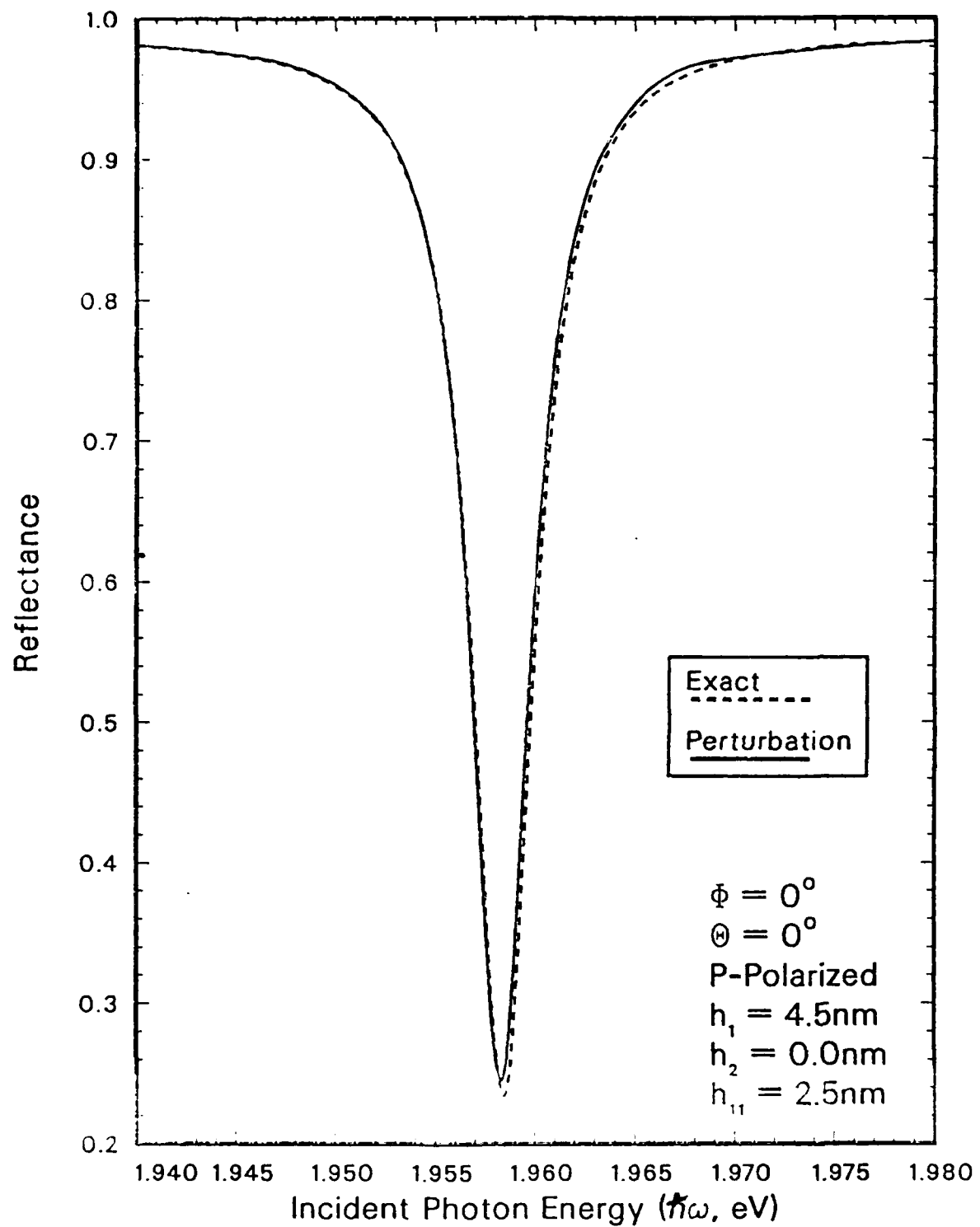


Figure 25. Reflectance Curves Versus Incident Photon Frequency for P Polarization.

Since there are gaps in the dispersion curve at the Bragg zone boundaries of the grating lattice, *i. e.* at $k = n\pi/a$, $n = \pm 1, \pm 2, \dots$, one would expect to see a pair of dips in the reflectance at such a boundary rather than the single dip in evidence in Figures 24 and 25. In the cases investigated here, $n = 2$ and the gap concerned lies at the second Bragg zone boundary. The reason for this apparent single dip in reflectance at the second Bragg zone boundary is that the energy gap in the cases investigated is narrower than the width of the states on either side of the gap; *i. e.*, the overlap of the neighboring states has completely bridged the gap.

C. CONVERGENCE OF EXACT THEORY CALCULATIONS

For the cases treated here, the maximum value of the cross term was $h_{11} = 2.5$ nm and this value is sufficiently small that the use of a single term in equation (29a) was effective in obtaining accurate results.

The truncation of the infinite series of equation (9) to the value of $N = 7$ was all that was required for excellent degrees of accuracy⁹. Convergence checks were performed for the maximum corrugation strengths for each polarization. Although the profile with $h_1 = 6.0$ nm and $h_{11} = 2.5$ nm has a

⁹See section IV.B on convergence in off-normal calculations for a detailed discussion of the truncations implied here and their effect on accuracy of calculations.

slightly smaller corrugation strength than the $h_1 = 7.4$ nm, $h_{11} = 0$ nm profile, convergence checks were conducted for the s and p polarizations of the profile with the non-zero cross term to ensure validity of the calculations.

Table 8, below, is a summary of the differences in the reflectance minima for the convergence checks. As with the off-normal convergence checks, the differences are subscripted with the two N values used in the calculations.

TABLE 8
SUMMARY OF CONVERGENCE CHECK RESULTS FOR
REFLECTANCES NEAR NORMAL INCIDENCE

h_1 (nm)	h_{11} (nm)	Pol.	$\Delta R_{5,7}$	$\Delta R_{7,9}$	$\Delta R_{9,11}$
7.4	0.0	s	5.5×10^{-5}	2.1×10^{-8}	2.5×10^{-10}
7.4	0.0	p	3.0×10^{-3}	2.1×10^{-5}	1.3×10^{-7}
6.0	2.5	s	9.3×10^{-5}	4.8×10^{-7}	3.4×10^{-9}
6.0	2.5	p	2.4×10^{-3}	1.6×10^{-5}	1.0×10^{-7}

From the values listed in the table, it can be seen that the use of the 98 x 98 matrix in exact calculations resulted in accuracies to at least one part in forty-five hundred and in one case to better than one part in 10^7 .

Table 9, on the following page, is a summary of the differences in enhancements for the convergence checks. As with the off-normal convergence checks, the accuracy figure is obtained by normalizing the differences using the

TABLE 9
 SUMMARY OF CONVERGENCE CHECK RESULTS FOR
 ENHANCEMENTS NEAR NORMAL INCIDENCE

h_1	h_{11}	Pol.	$\Delta \epsilon_{5,7}$	$\Delta \epsilon_{7,9}$	$\Delta \epsilon_{9,11}$	ϵ_{11}
7.4nm	0.0nm	s	1.105	9.5×10^{-2}	8.5×10^{-3}	40.241
7.4nm	0.0nm	p	0.945	9.3×10^{-2}	8.2×10^{-3}	39.610
6.0nm	2.5nm	s	1.170	9.7×10^{-2}	8.0×10^{-3}	37.517
6.0nm	2.5nm	p	1.020	9.4×10^{-2}	7.7×10^{-3}	36.683

enhancement value obtained in the $N = 11$ calculation. The accuracies achieved here are at least to one part in three hundred fifty.

AD-A184 663

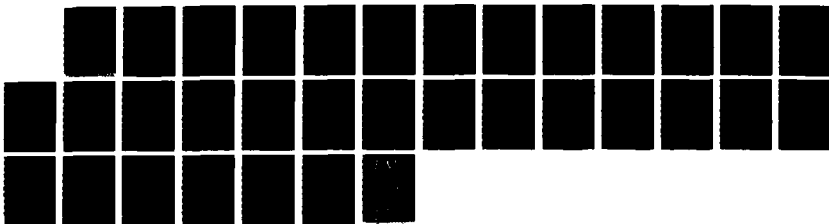
SURFACE POLARITON RESONANCES AND REFLECTANCE ON A
BIRGRATING(U) NAVAL POSTGRADUATE SCHOOL MONTEREY CA
G J MELENDEZ JUN 87

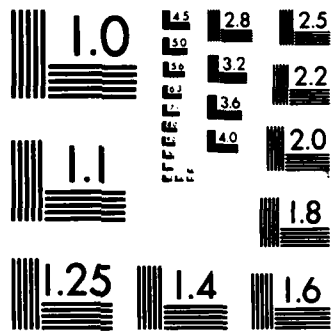
2/2

UNCLASSIFIED

F/G 28/3

NL





MICROCOPY RESOLUTION TEST CHART
NATIONAL BUREAU OF STANDARDS-1963-A

VI. CONCLUSIONS AND RECOMMENDATIONS

The perturbation theory has been validated to yield reliable results at off-normal incidence for corrugation strengths of 0.024 and less. Its performance in predicting bigrating absorptance efficiencies and enhancement capabilities is limited by the quantity $\alpha\zeta_{\max}$ which must be less than one. Thus, Glass's modification to his perturbation theory to include simultaneous excitation of four resonant surface polaritons, rather than only two, has not altered its performance in cases of off-normal incidence. This may be verified by comparison of the results contained in this work with those presented by Glass [Ref. 21] for the two resonant surface polariton perturbation theory.

Use of the perturbation theory at normal incidence will yield results for reflectance and enhancement versus angle of incidence to at least within an order of magnitude of the exact theory values. The degree of accuracy achieved is dependent upon the amount of cross coupling present for the particular surface profile being investigated. From the results presented here, the perturbation theory appears to perform best when the surface profile induces appreciable degrees of coupling through cross terms. It is recommended that further investigations be conducted in this area by

performing comparison calculations using the perturbative and nonperturbative analysis techniques with surface profile functions of more evenly distributed values for the height coefficients. Based on the results obtained in this work, it is believed that a marked improvement in the performance of the perturbation theory would be achieved for such surface profiles. There has been considerable work using sawtooth type diffraction grating profiles [Ref. 28]. A bigrating with this type of surface profile may well be treated using the perturbation theory with much greater accuracy near normal incidence than has been found with the surface profiles dealt with here.

In frequency scans at normal incidence the perturbation theory may be employed with considerably more confidence. Reflectance magnitudes may be relied upon to be within approximately 5% of the exact theory values and the predictions for optimum coupling frequency can be taken as accurate to within approximately 2%. The enhancement magnitudes in such scans, however, may still only be taken as accurate to within an order of magnitude.

A final observation is made here that the reflectance value for a given surface profile at exactly normal incidence on a bigrating is independent of the incident polarization. Figures 26 and 27, on the following two pages, illustrate this fact graphically for the surface profile of $h_1 = 4.5$ nm and $h_{11} = 2.5$ nm. Note in Figure 26

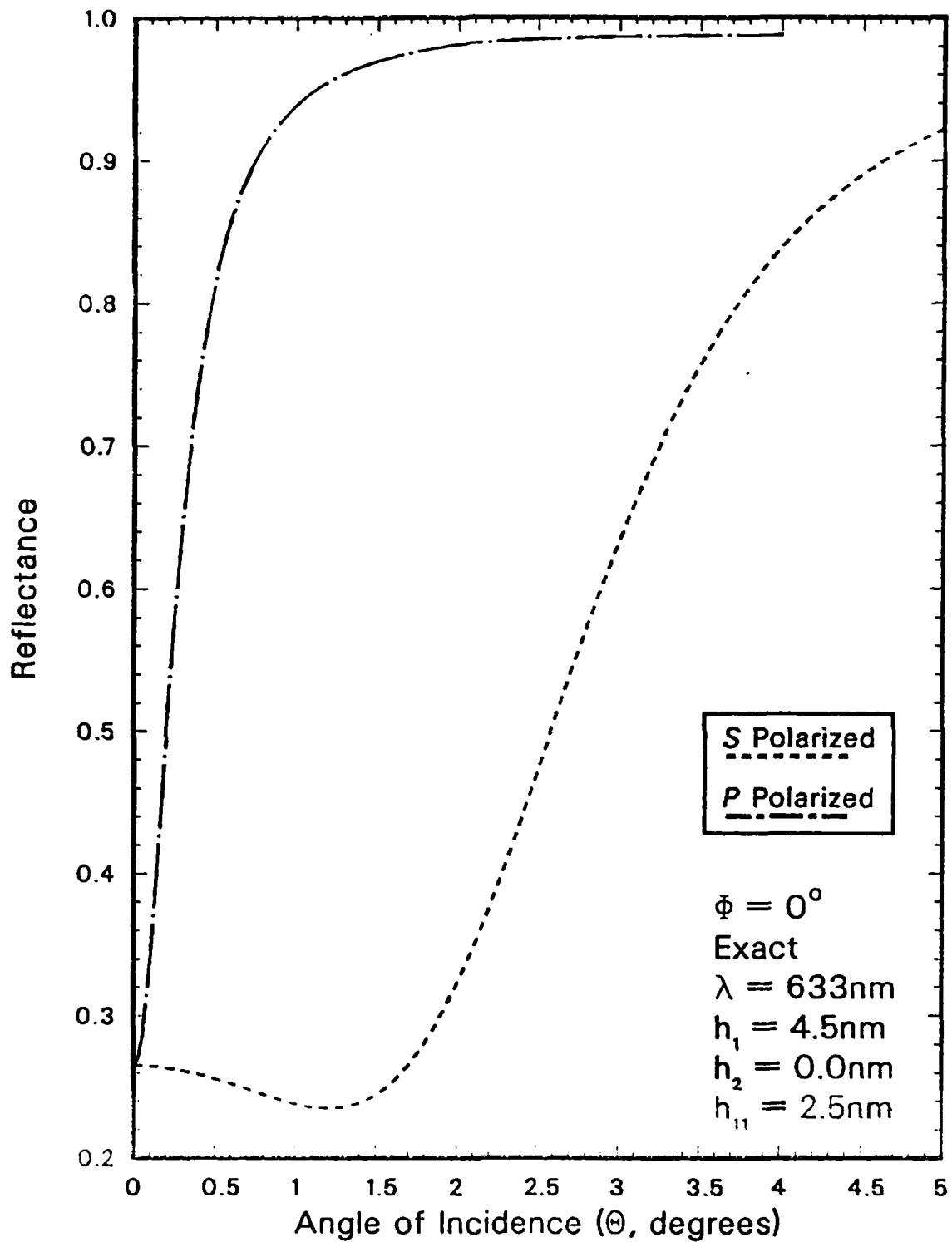


Figure 26. Reflectance Curve Comparisons for S and P Polarizations Versus Angle of Incidence.

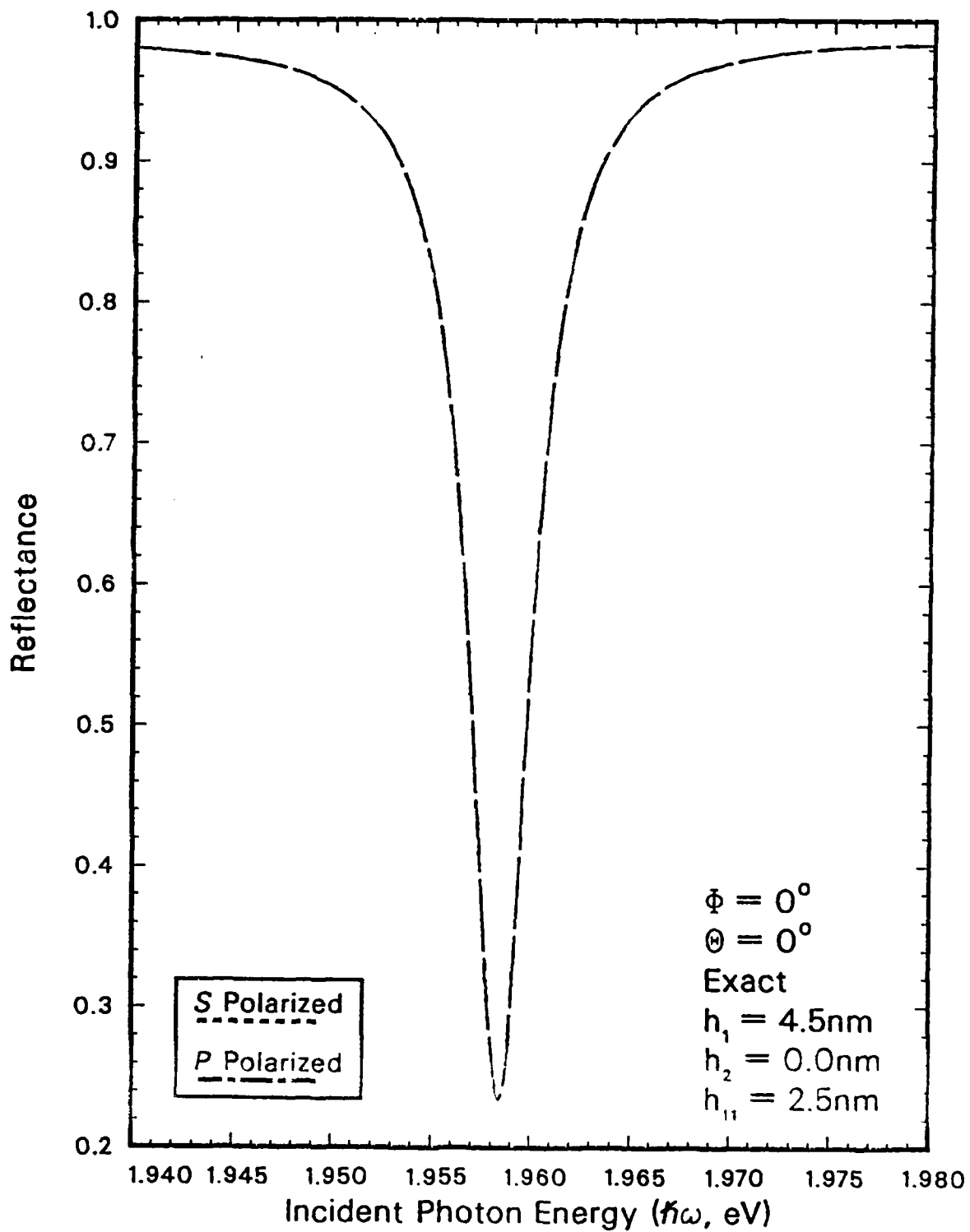


Figure 27. Reflectance Curve Comparisons for S and P Polarizations Versus Incident Photon Energy.

that the magnitude of the reflectance curves for s and p polarization are identical at $\theta = 0^\circ$. The curves for the reflectance of the two incident polarizations in Figure 27 are identical for all incident photon energies. The data from other calculations also show that the magnitudes of the reflectance minima for exactly normal incidence are numerically identical for s and p polarizations to the full accuracies of the exact calculations.

APPENDIX A

DEFINITIONS OF PERTURBATION MATRIX ELEMENTS

Equation (21), which is stated as the final result of the perturbation theory (subsection II.B.2), contains several elements whose definitions are not given in the text. The equations which define these terms are quoted here (taken from Glass [Ref. 9]). The prime on the summations indicate the specified sum is taken over all j except the specular ($j = 0$) and resonant wave ($j = 1, 2, 3,$ and 4) terms.

$$\tilde{\omega}_r^2 \equiv \omega_r^2 \left\{ 1 - \frac{c^2 \alpha_{rr} \gamma_r}{(1+\epsilon) \omega^2 k_r^2} \left[\sum_{p=1}^4 (1-\delta_{rp}) \tilde{\zeta}(r-p) \alpha_{pp} a_{rp}^2 \right] + \sum_j' \tilde{\zeta}(r-j) \tilde{\zeta}(j-r) \alpha_{jj} \left[\frac{c_{rj} c_{jr}}{c_{jj}} + a_{rj}^2 \right] \right\}, \quad (\text{A.1})$$

where

$$\gamma_r \equiv \alpha(r) \alpha_0(r) \left[\alpha(r) \alpha_0(r) - k_r^2 \right]. \quad (\text{A.2})$$

$$L_{rp} \equiv h_r \left[i \tilde{\zeta}(r-p) c_{rp} - \sum_j' \tilde{\zeta}(r-j) \tilde{\zeta}(j-p) (f_{rj} c_{jp} - a_{rj} a_{jp}) \alpha_{jj} \right], \quad (\text{A.3})$$

where

$$h_r \equiv - \frac{\gamma_r \alpha_{rr} c^4}{\epsilon \omega^2} \left[\frac{a}{2\pi c} \right]^2, \quad (\text{A.4})$$

and

$$f_{rj} \equiv \frac{c_{rj}}{c_{jj}} . \quad (\text{A.5})$$

$$M_r \equiv h_r \left[i \tilde{\zeta}(r) c_{r0} + \sum_{p=1}^4 (1-\delta_{rp}) \tilde{\zeta}(r-p) \tilde{\zeta}(p) \alpha_{pp} a_{rp} a_{p0} \right. \\ \left. - \sum_j' \tilde{\zeta}(r-j) \tilde{\zeta}(j) (f_{rj} c_{j0} - a_{rj} a_{j0}) \alpha_{jj} \right]. \quad (\text{A.6})$$

$$N_r \equiv -h_r \left[i \tilde{\zeta}(r) a_{r0} - \sum_{p=1}^4 (1-\delta_{rp}) \tilde{\zeta}(r-p) \tilde{\zeta}(p) \alpha_{pp} a_{rp} b_{p0} \right. \\ \left. - \sum_j' \tilde{\zeta}(r-j) \tilde{\zeta}(j) (f_{rj} a_{j0} + a_{rj} b_{j0}) \alpha_{jj} \right]. \quad (\text{A.7})$$

$$O_r \equiv -\frac{\alpha_{00}}{c_{00}} \left[i \tilde{\zeta}(-r) c_{0r} + \sum_{p=1}^4 (1-\delta_{rp}) \tilde{\zeta}(p-r) \tilde{\zeta}(-p) \alpha_{pp} a_{pr} a_{0p} \right. \\ \left. - \sum_j' \tilde{\zeta}(j-r) \tilde{\zeta}(-j) (f_{0j} c_{jr} - a_{rj} a_{j0}) \alpha_{jj} \right]. \quad (\text{A.8})$$

$$P \equiv \frac{\alpha_{00}}{c_{00}} \left[\sum_{p=1}^4 \tilde{\zeta}(p) \tilde{\zeta}(-p) \alpha_{pp} a_{0p}^2 \right. \\ \left. + \sum_j' \tilde{\zeta}(j) \tilde{\zeta}(-j) (f_{0j} c_{j0} + a_{0j}^2) \alpha_{jj} \right]. \quad (\text{A.9})$$

$$Q \equiv -\frac{\alpha_{00}}{c_{00}} \left[\sum_{p=1}^4 \tilde{\zeta}(p) \tilde{\zeta}(-p) \alpha_{pp} a_{0p} b_{p0} \right. \\ \left. + \sum_j' \tilde{\zeta}(j) \tilde{\zeta}(-j) (f_{0j} - b_{j0}) a_{j0} \alpha_{jj} \right]. \quad (\text{A.10})$$

$$R_r \equiv -\alpha_{00} \left[t \tilde{\zeta}(-r) a_{0r} - \sum_{p=1}^4 (1-\delta_{rp}) \tilde{\zeta}(p-r) \tilde{\zeta}(-p) \alpha_{pp} a_{pr} b_{p0} \right. \\ \left. - \sum_j' \tilde{\zeta}(j-r) \tilde{\zeta}(-j) (f_{jr} a_{0j} + a_{jr} b_{j0}) \alpha_{jj} \right]. \quad (\text{A.11})$$

$$S \equiv \alpha_{00} \left[\sum_{p=1}^4 \tilde{\zeta}(p) \tilde{\zeta}(-p) \alpha_{pp} a_{p0} b_{p0} \right. \\ \left. + \sum_j' \tilde{\zeta}(j) \tilde{\zeta}(-j) (f_{j0} - b_{j0}) a_{0j} \alpha_{jj} \right]. \quad (\text{A.12})$$

$$T \equiv \alpha_{00} \left[\sum_{p=1}^4 \tilde{\zeta}(p) \tilde{\zeta}(-p) \alpha_{pp} b_{p0}^2 \right. \\ \left. + \sum_j' \tilde{\zeta}(j) \tilde{\zeta}(-j) \left\{ \frac{a_{0j}^2}{c_{jj}} + b_{j0}^2 \right\} \alpha_{jj} \right]. \quad (\text{A.13})$$

$$U_r \equiv h_r \left[t \tilde{\zeta}(r) (c_{r0} - e_r) - \sum_j' \tilde{\zeta}(r-j) \tilde{\zeta}(j) \tau_j c_{rj} \right], \quad (\text{A.14})$$

where

$$\tau_j \equiv \frac{\alpha_{jj}}{c_{jj}} [c_{j0} - e_j]. \quad (\text{A.15})$$

$$v \equiv \frac{\alpha_{00}}{c_{00}} \left[\sum_j' \tilde{\zeta}(j) \tilde{\zeta}(-j) \tau_j c_{0j} \right]. \quad (\text{A.16})$$

$$w \equiv - \frac{\alpha_{00} e_j}{c_{00} \beta_0}. \quad (\text{A.17})$$

$$x = \alpha_{00} \sum_j' \tilde{\zeta}(j) \tilde{\zeta}(-j) \tau_j a_{0j}. \quad (\text{A.18})$$

APPENDIX B

ENHANCEMENT CURVES FOR CASES INVESTIGATED

This appendix is a collection of the curves for enhancement versus angle of incidence and versus incident photon energy. The figures are presented here in the same order in which the corresponding reflectance curves appear within the text of Chapters IV and V.

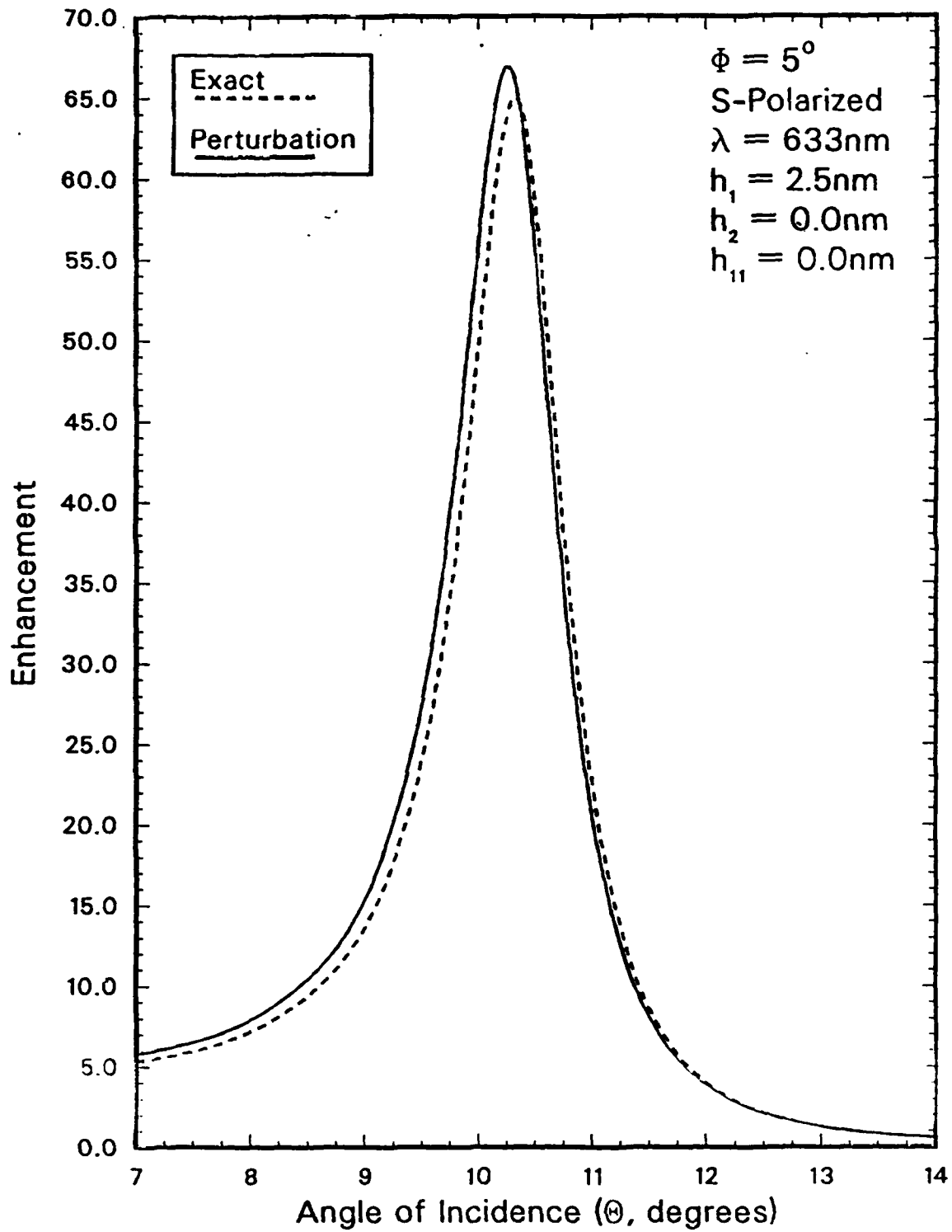


Figure 28. Enhancement Curves for 5° Azimuth with h_1 at 2.5 nm.

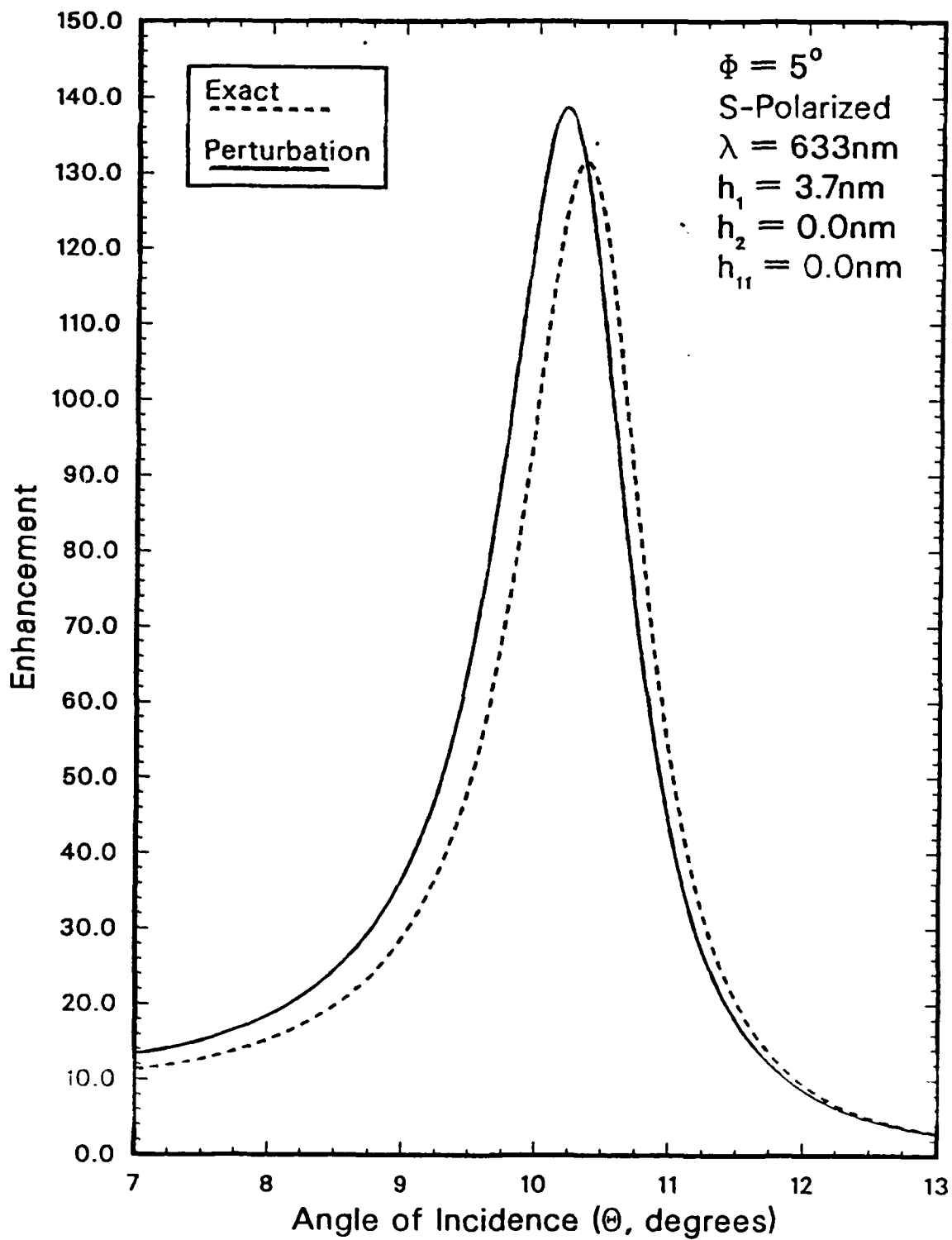


Figure 29. Enhancement Curves for 5° Azimuth with h_1 at 3.7 nm.

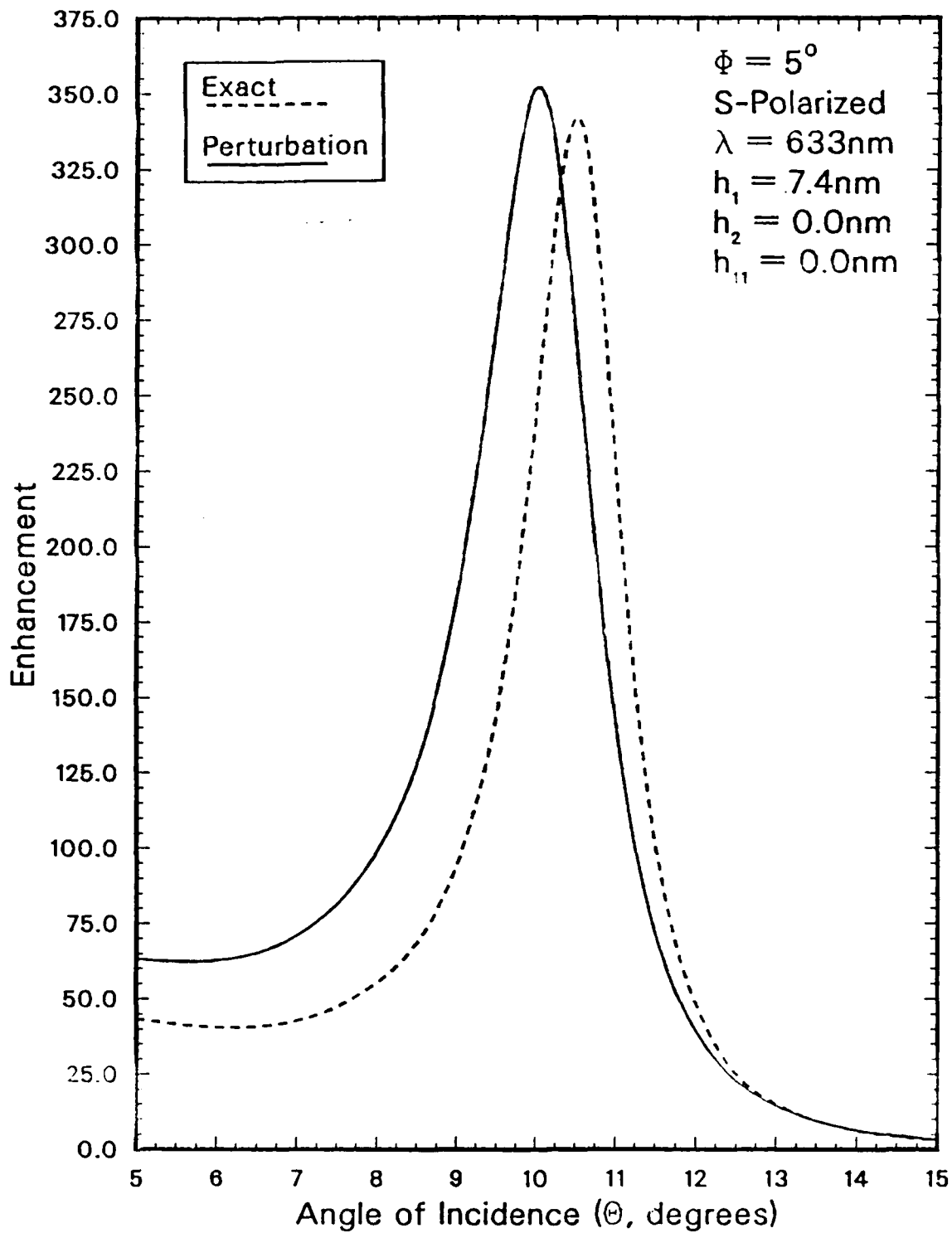


Figure 30. Enhancement Curves for S Polarized Light at 5° Azimuth and h_1 at 7.4 nm.

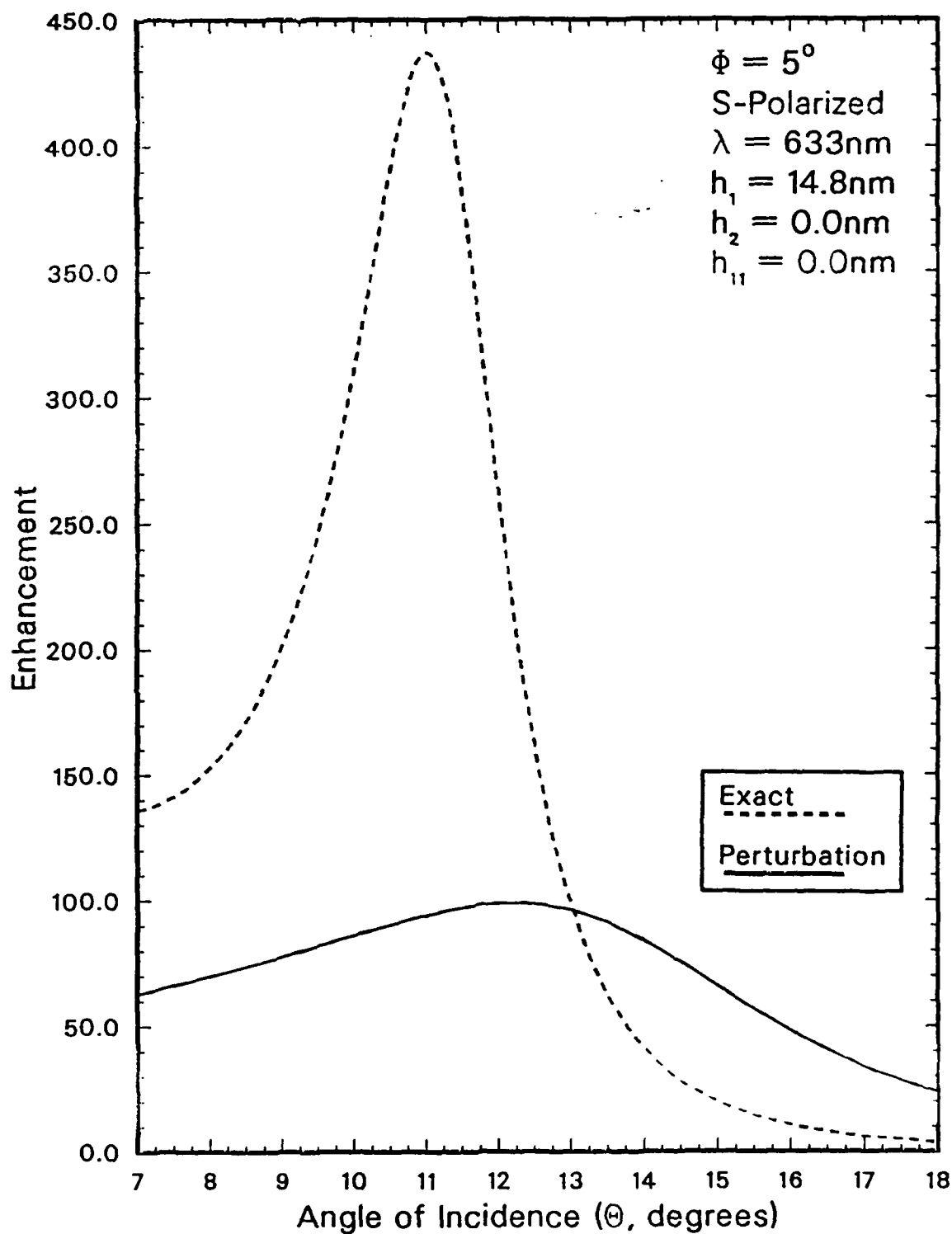


Figure 31. Enhancement Curves for 5° Azimuth with h_1 at 14.8 nm.

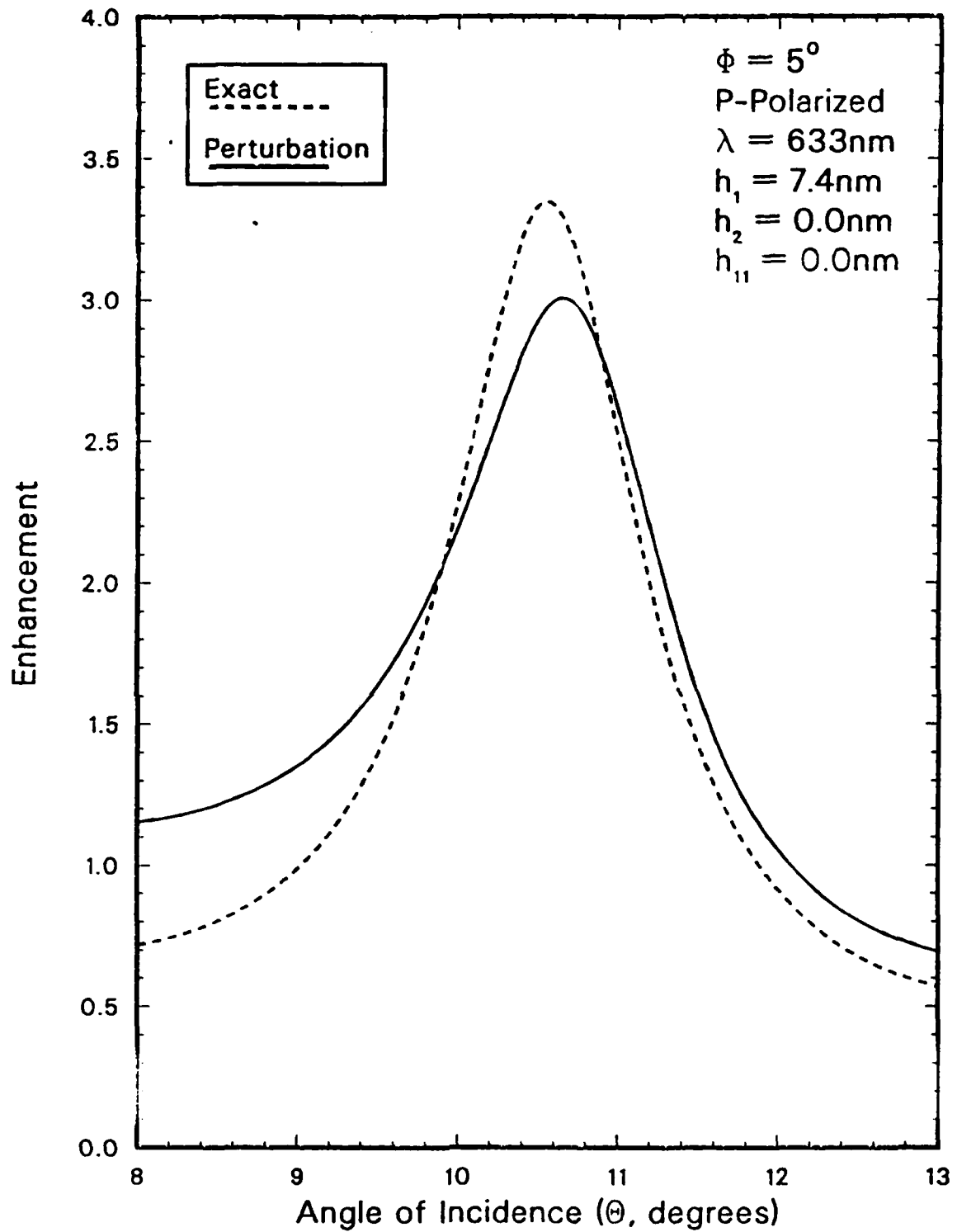


Figure 32. Enhancement Curves for P Polarized Light at 5° Azimuth and h_1 at 7.4 nm.

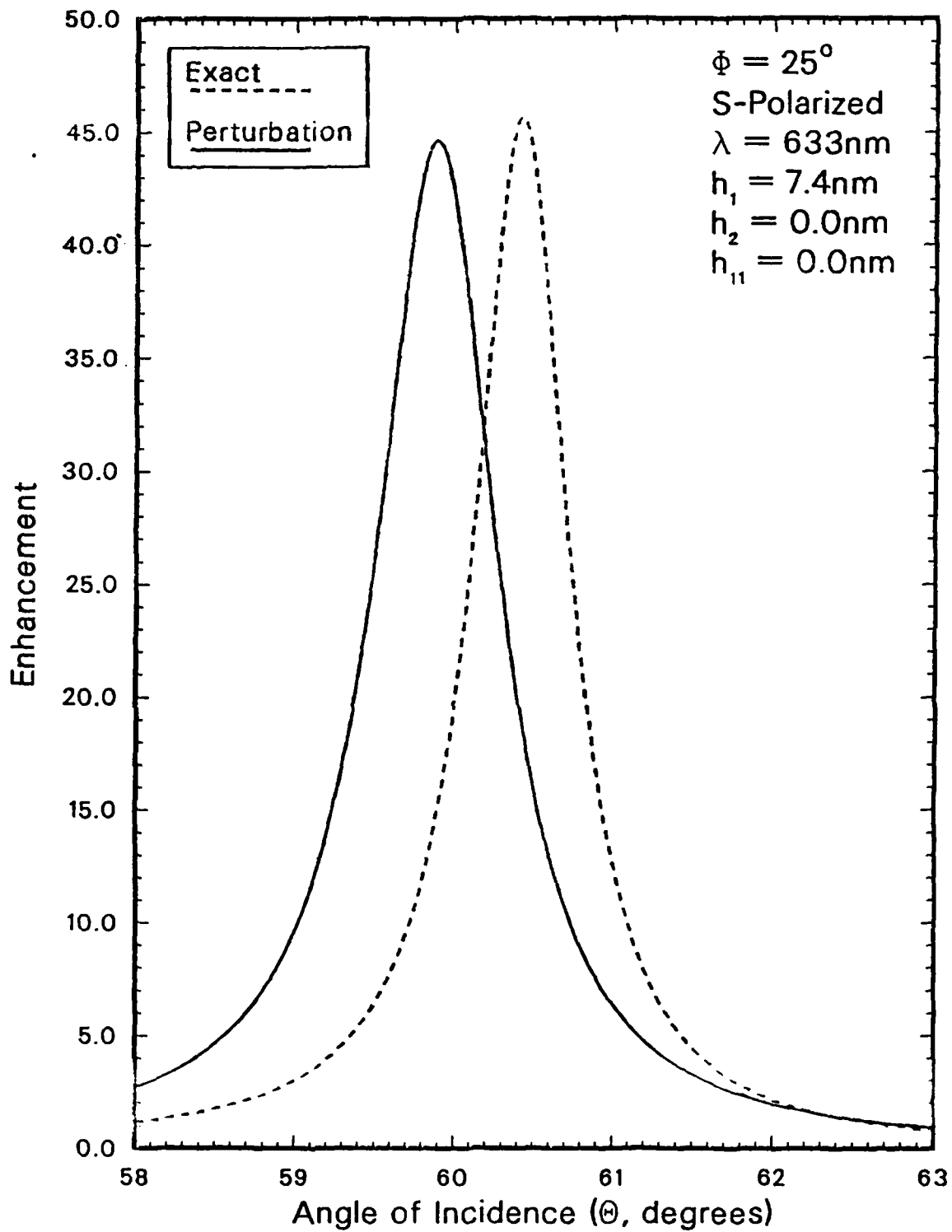


Figure 33. Enhancement Curves for S Polarized Light at 25° Azimuth and h_1 at 7.4 nm.

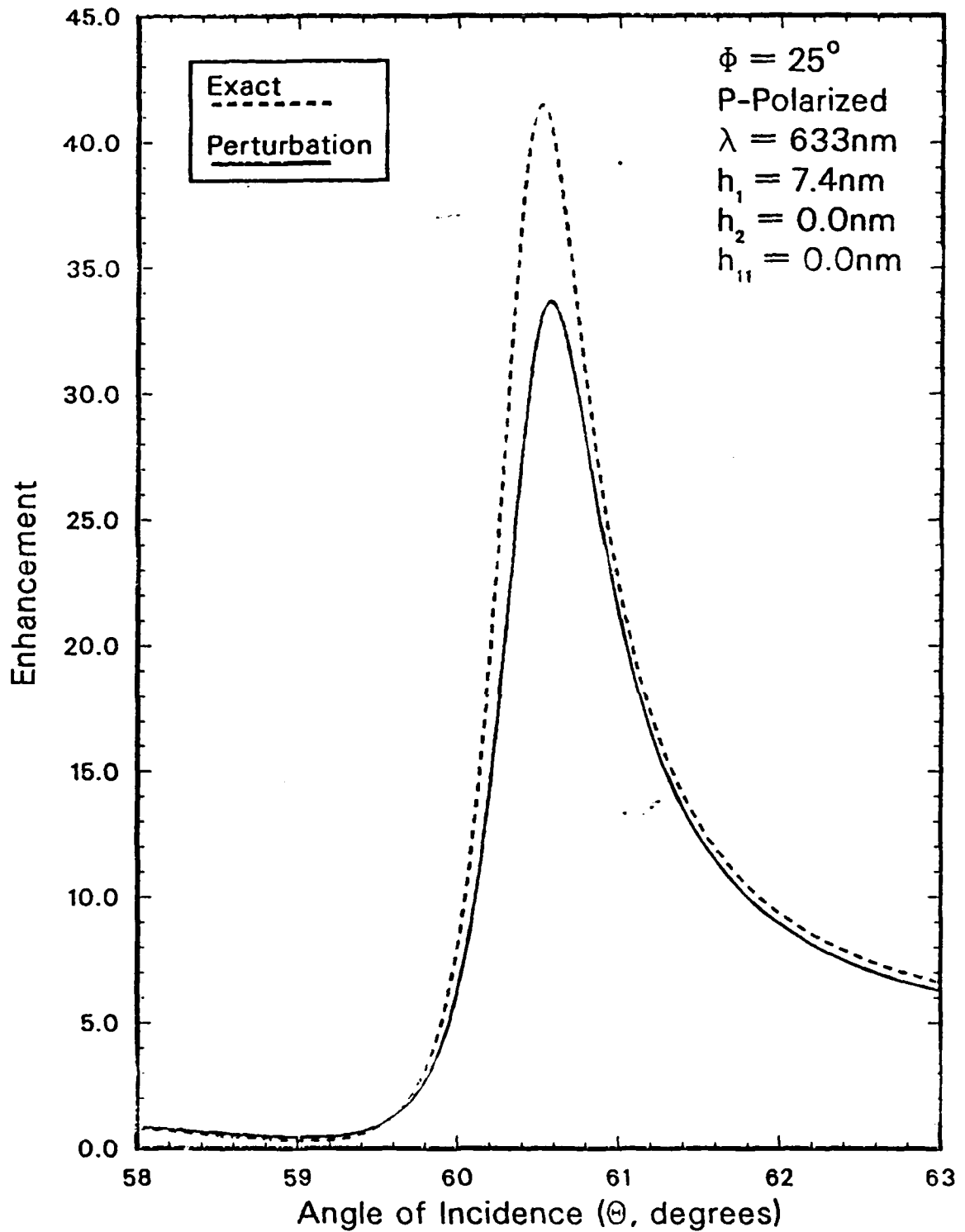


Figure 34. Enhancement Curves for P Polarized Light at 25° Azimuth and h_1 at 7.4 nm.

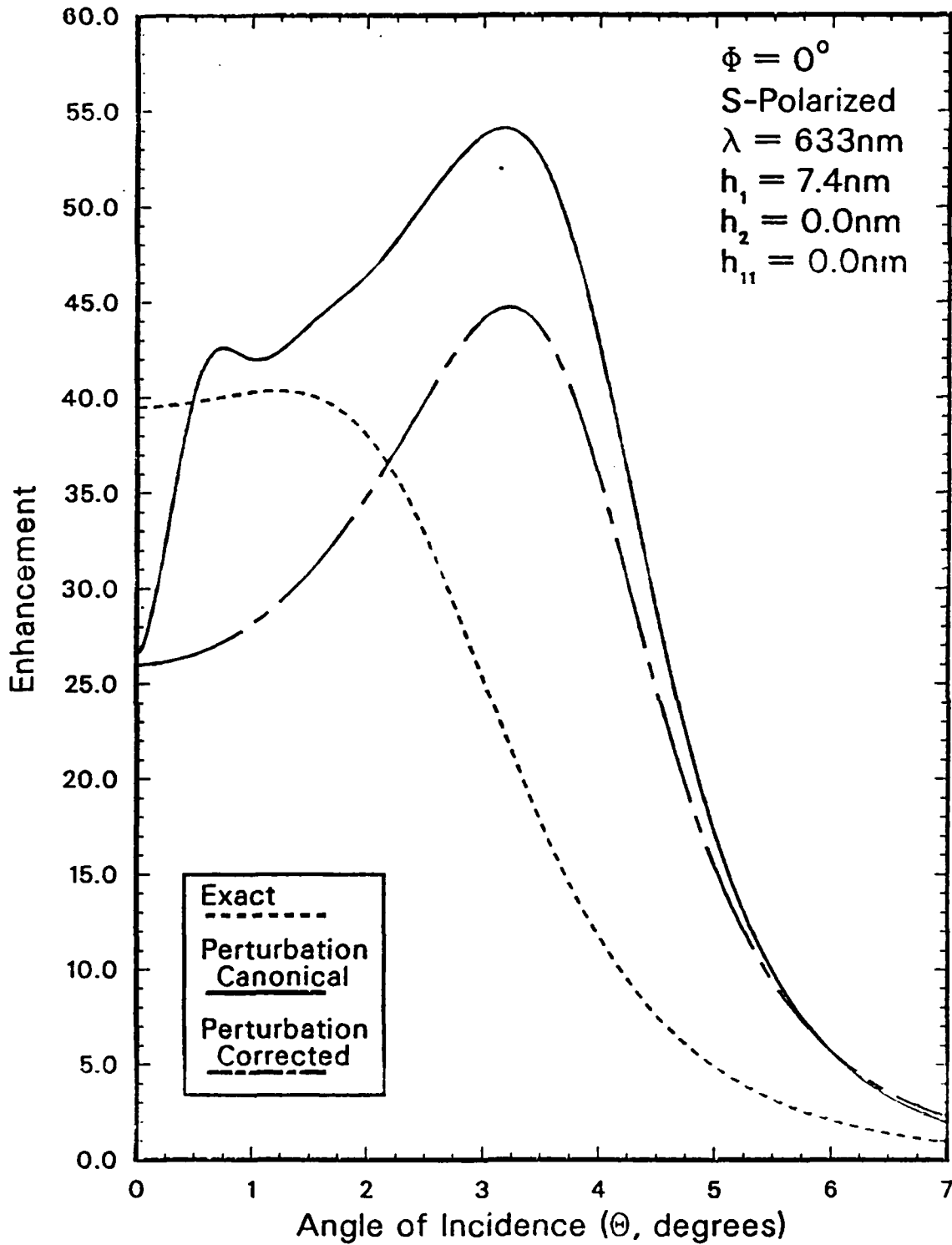


Figure 35. Enhancement Curves for $h_1 = 7.4$ nm Near Normal Incidence with 0° Azimuth and S Polarization.

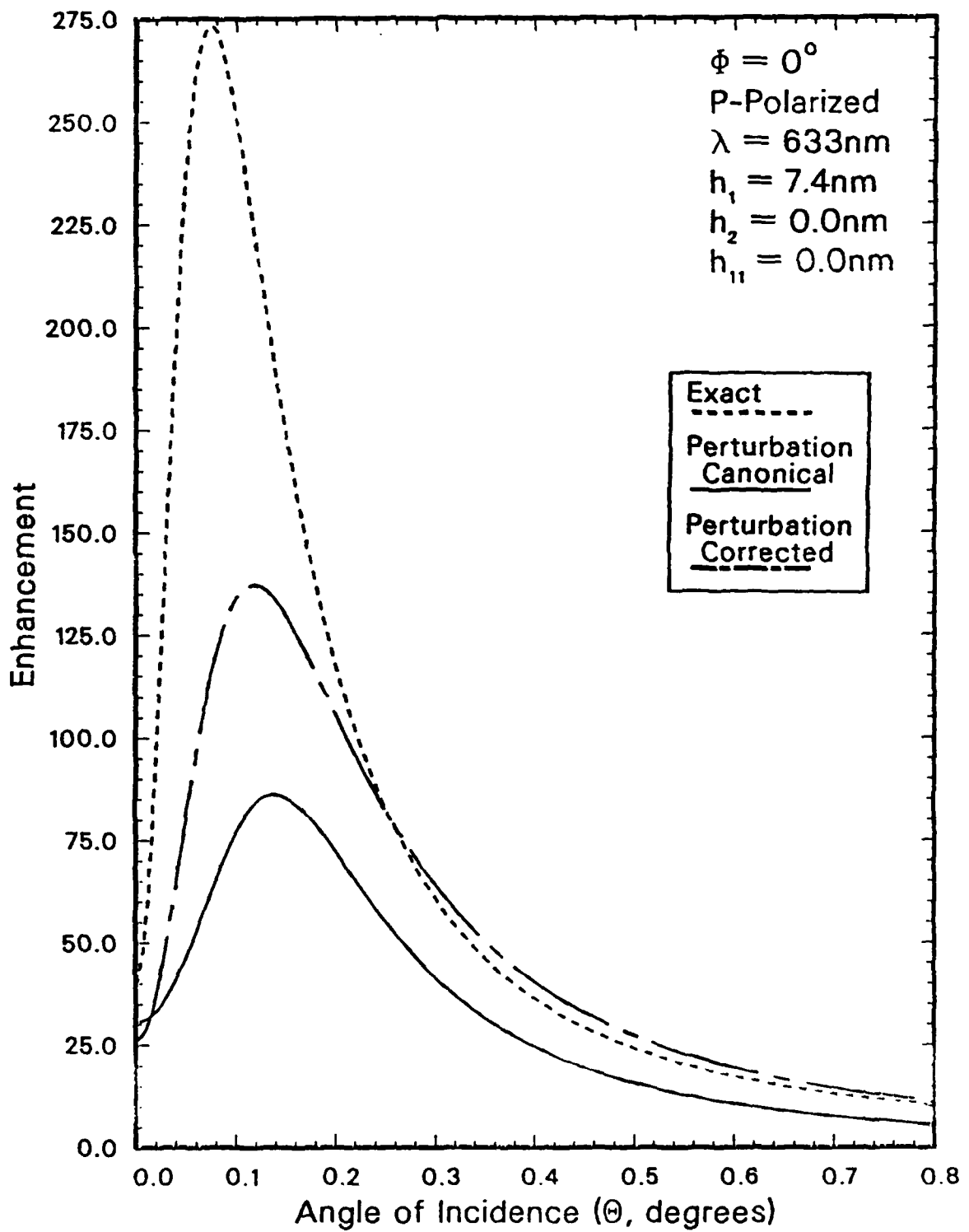


Figure 36. Enhancement Curves for $h_1 = 7.4$ nm Near Normal Incidence with 0° Azimuth and P Polarization.

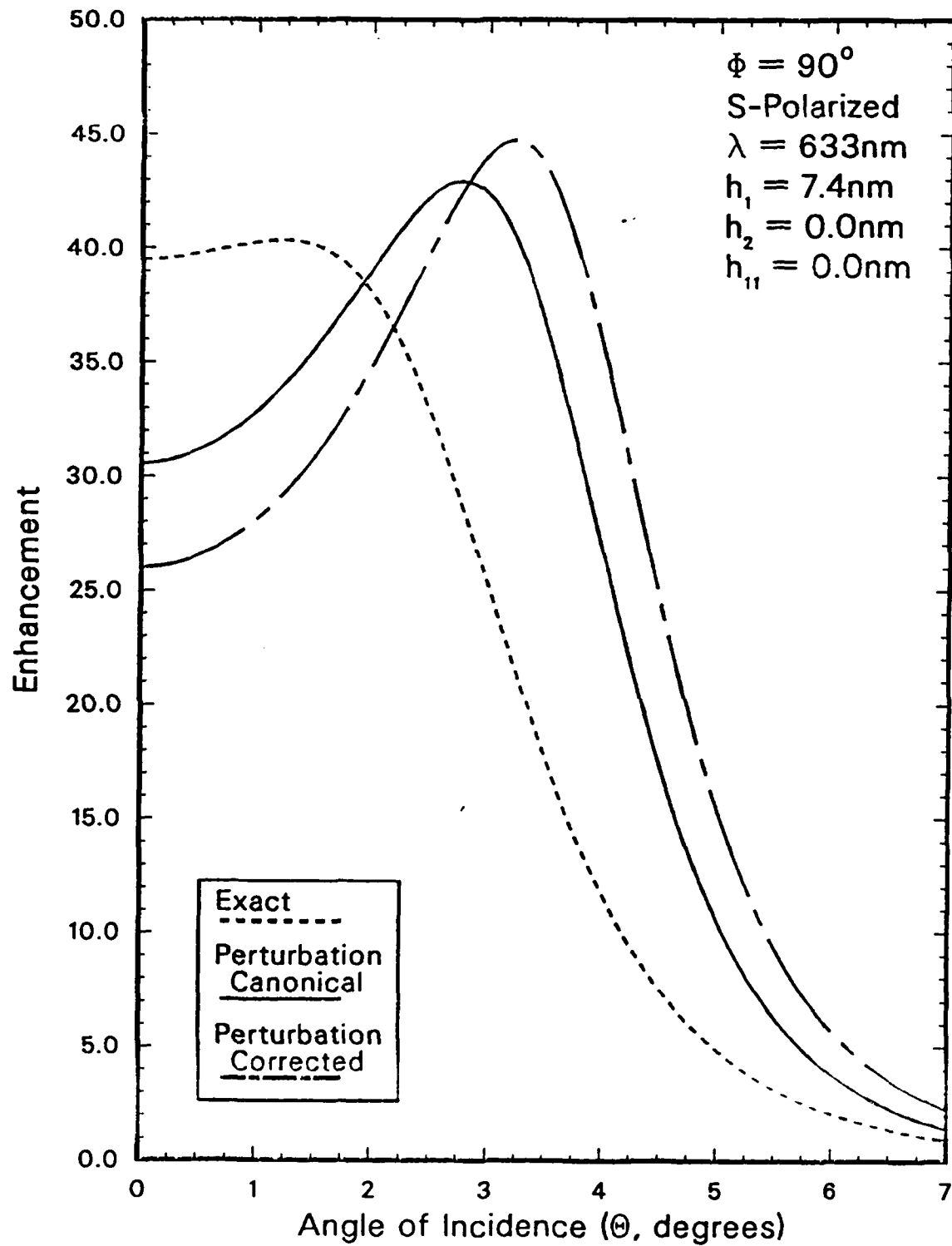


Figure 37. Enhancement Curves for $h_1 = 7.4$ nm Near Normal Incidence with 90° Azimuth and S Polarization.

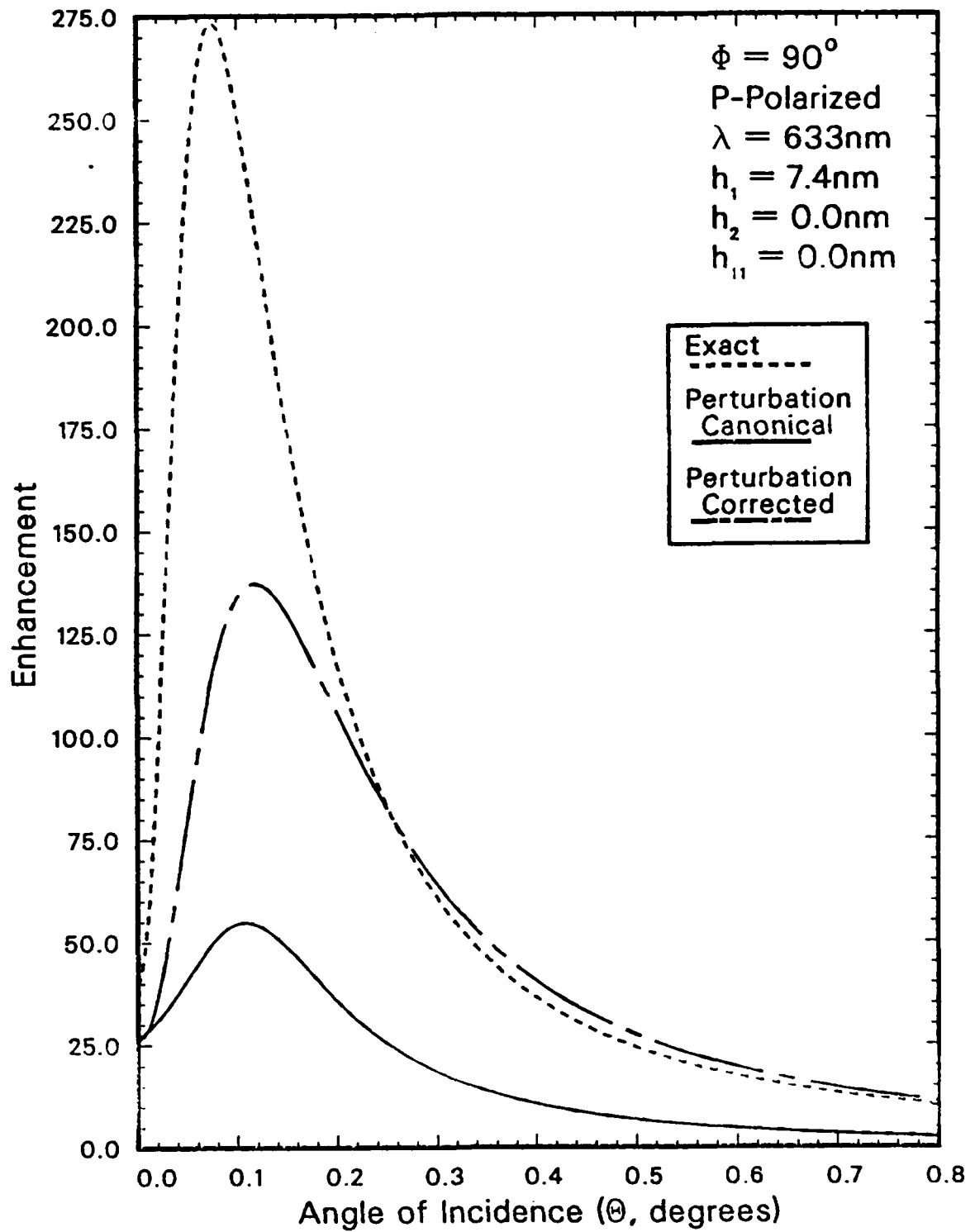


Figure 38. Enhancement Curves for $h_1 = 7.4$ nm Near Normal Incidence with 90° Azimuth and P Polarization.

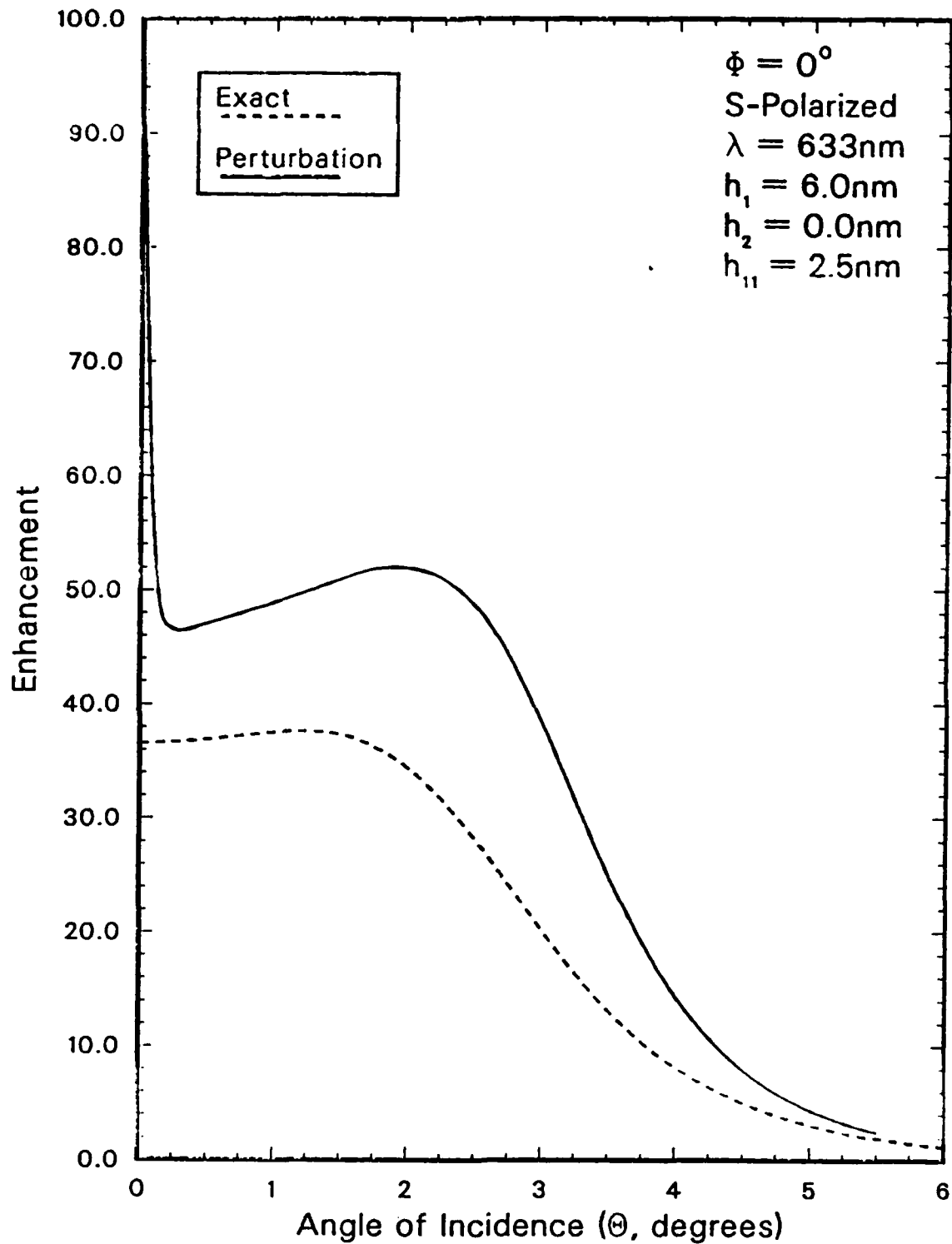


Figure 39. Enhancement Curves for $h_1 = 6.0 \text{ nm}$ and $h_{11} = 2.5 \text{ nm}$ with S Polarization.

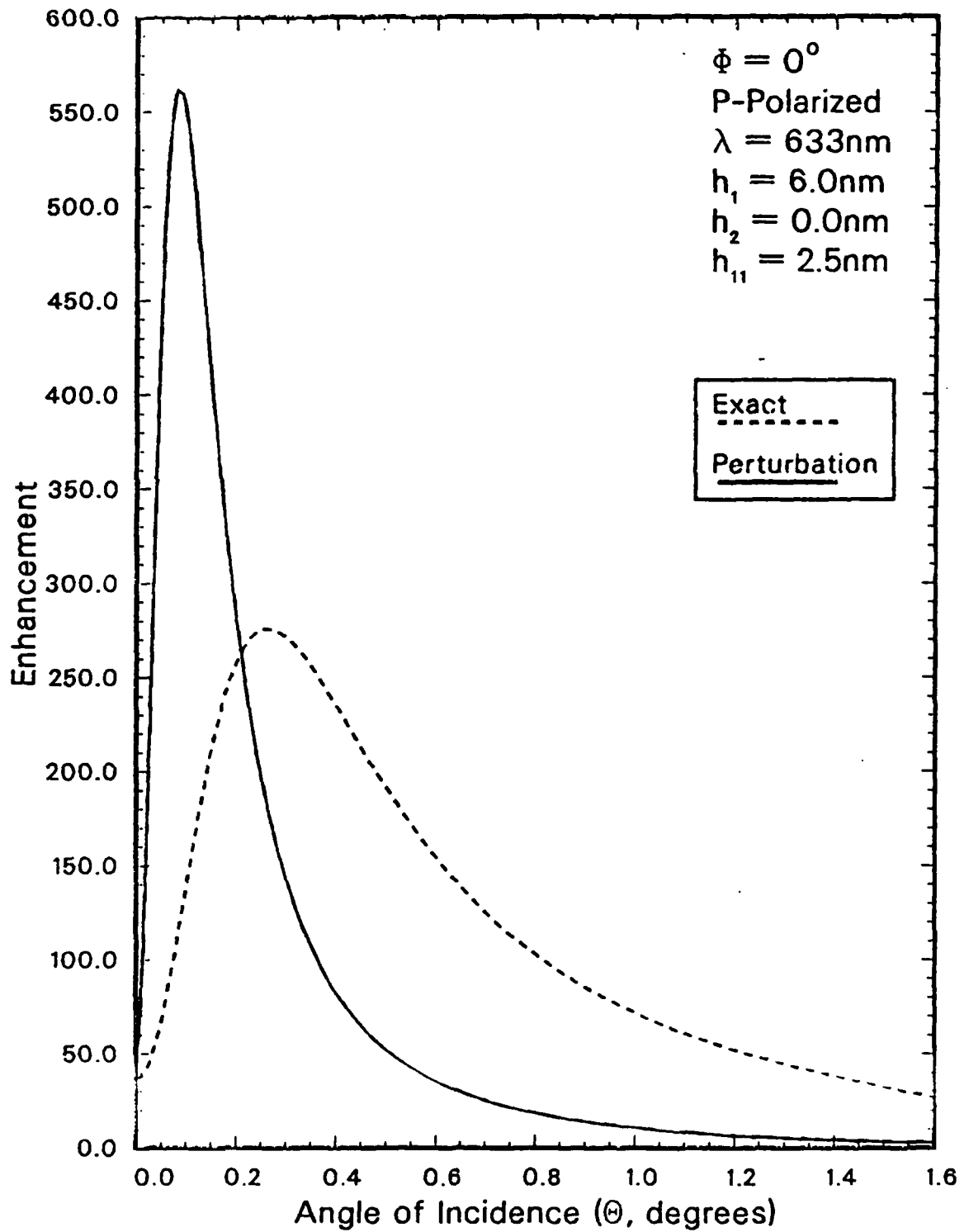


Figure 40. Enhancement Curves for $h_1 = 6.0 \text{ nm}$ and $h_{11} = 2.5 \text{ nm}$ with P Polarization.

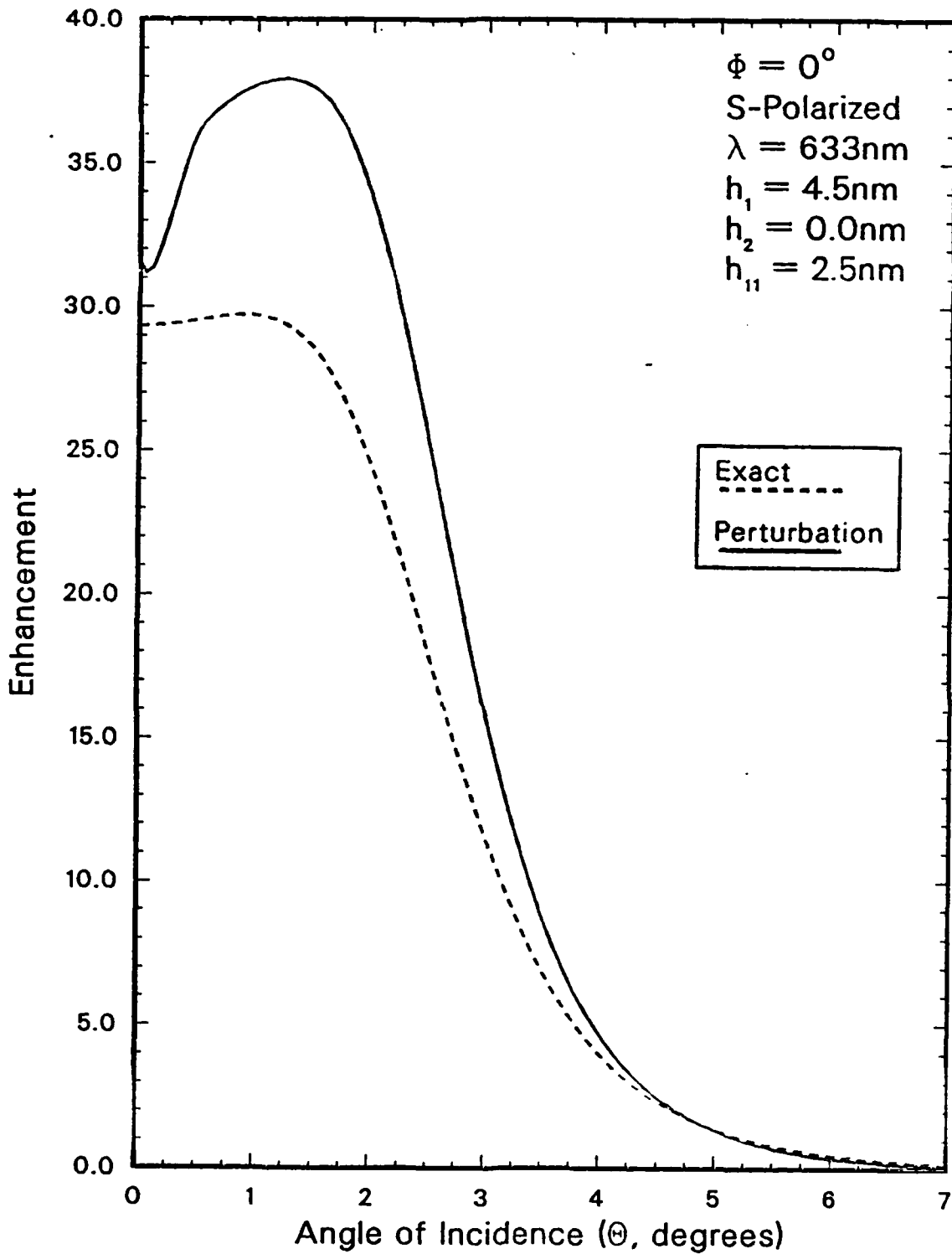


Figure 41. Enhancement Curves for $h_1 = 4.5$ nm and $h_{11} = 2.5$ nm with S Polarization.

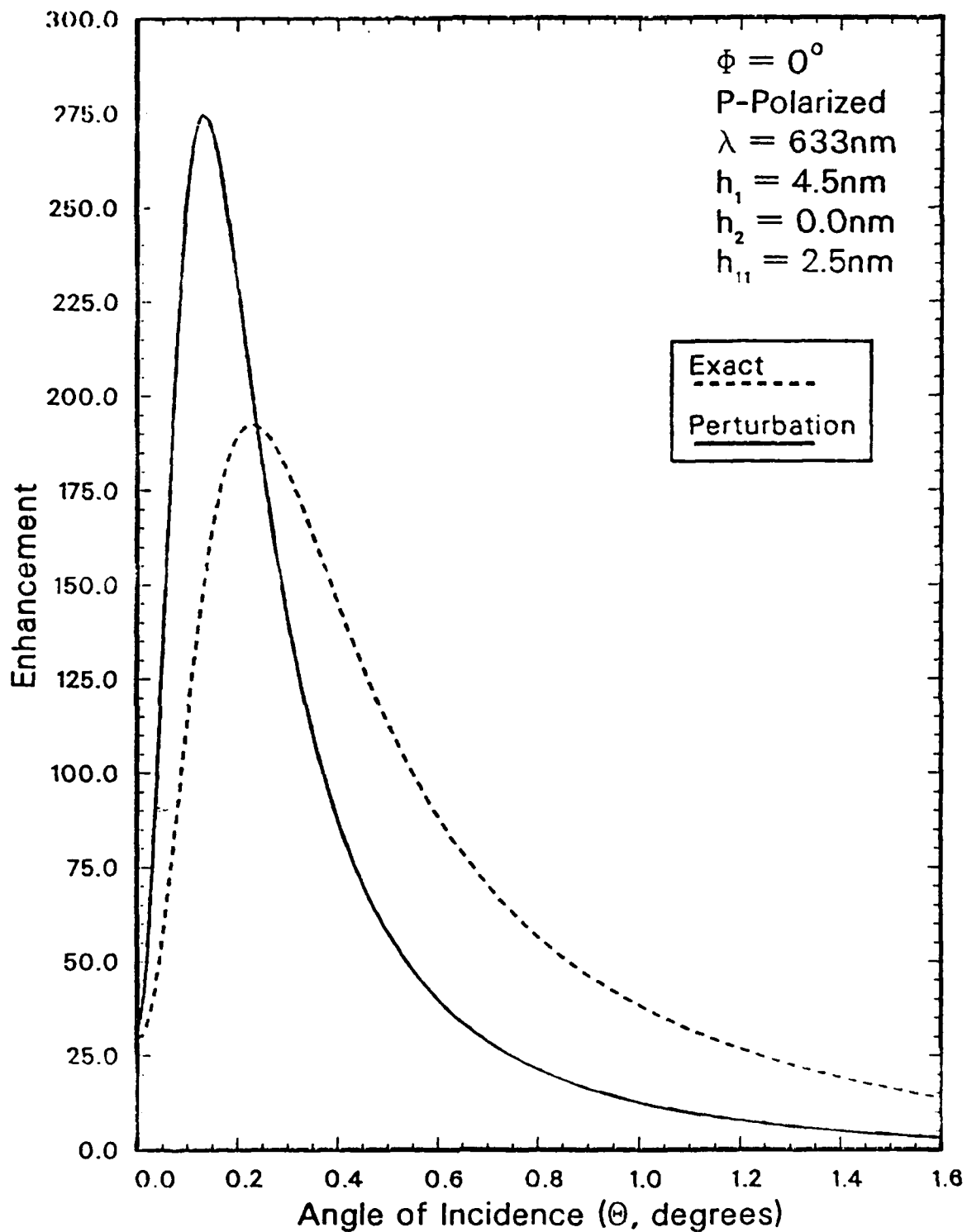


Figure 42. Enhancement Curves for $h_1 = 4.5 \text{ nm}$ and $h_{11} = 2.5 \text{ nm}$ with P Polarization.

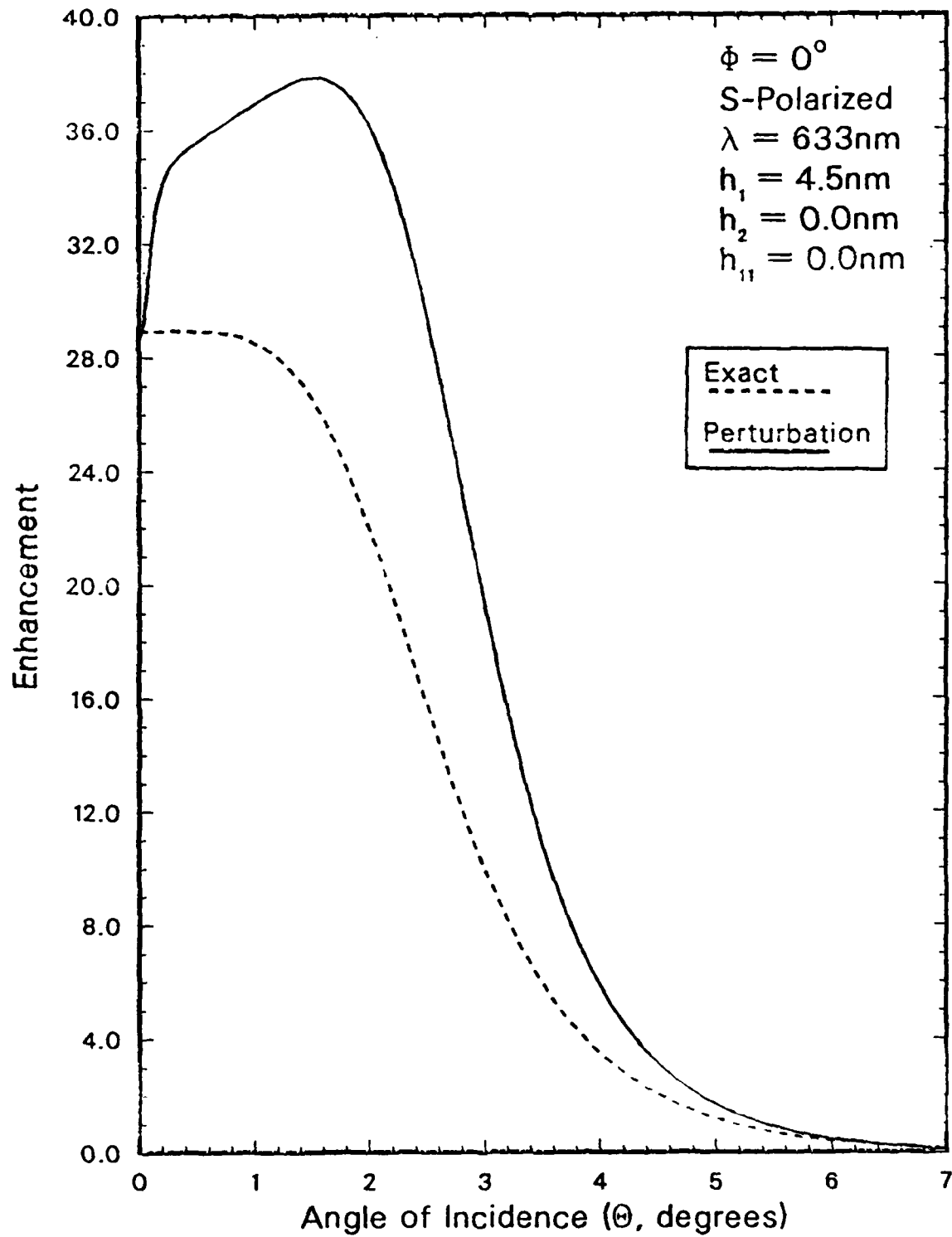


Figure 43. Enhancement Curves for $h_1 = 4.5 \text{ nm}$ and $h_{11} = 0 \text{ nm}$ with S Polarization.

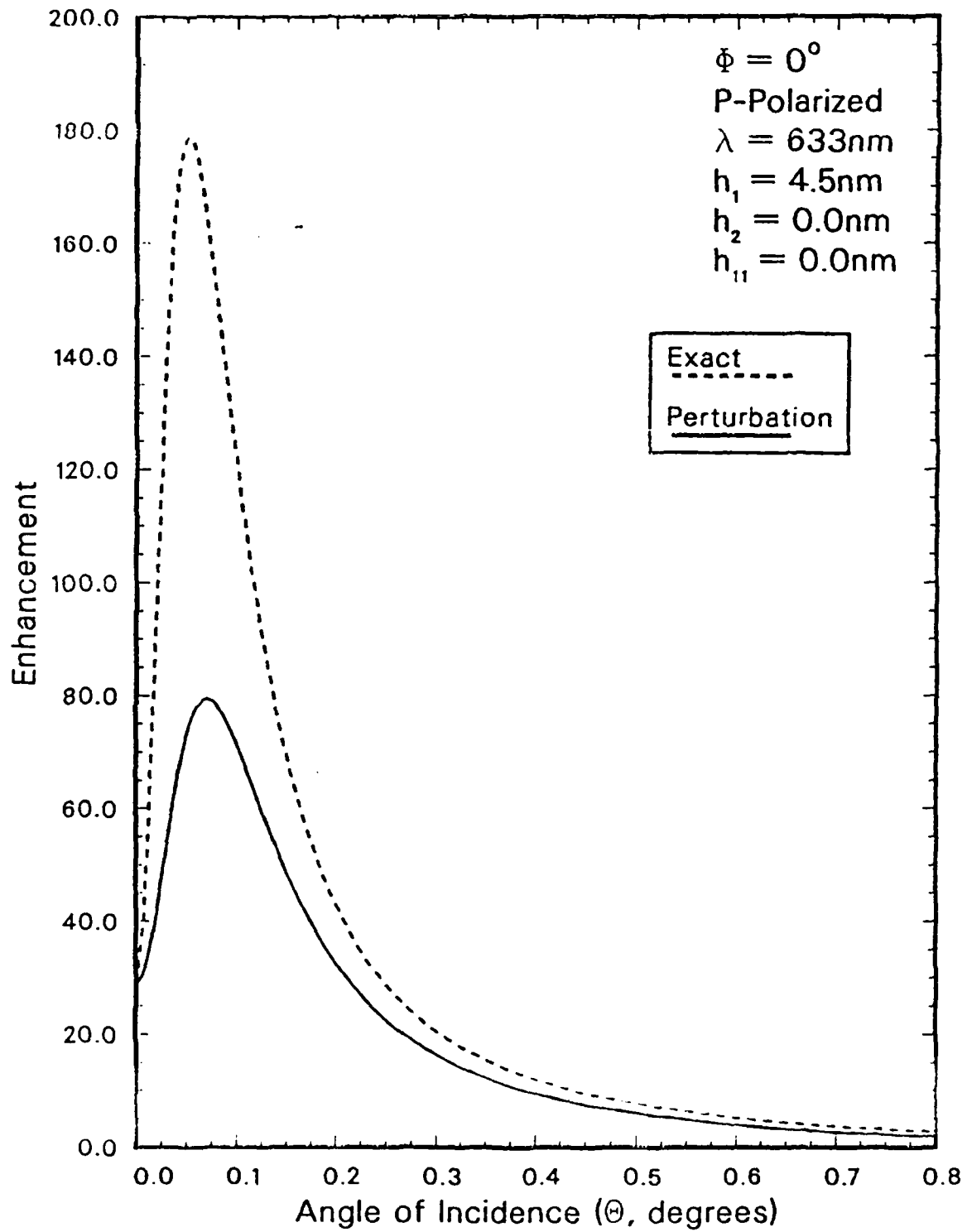


Figure 44. Enhancement Curves for $h_1 = 4.5$ nm and $h_{11} = 0$ nm with P Polarization.

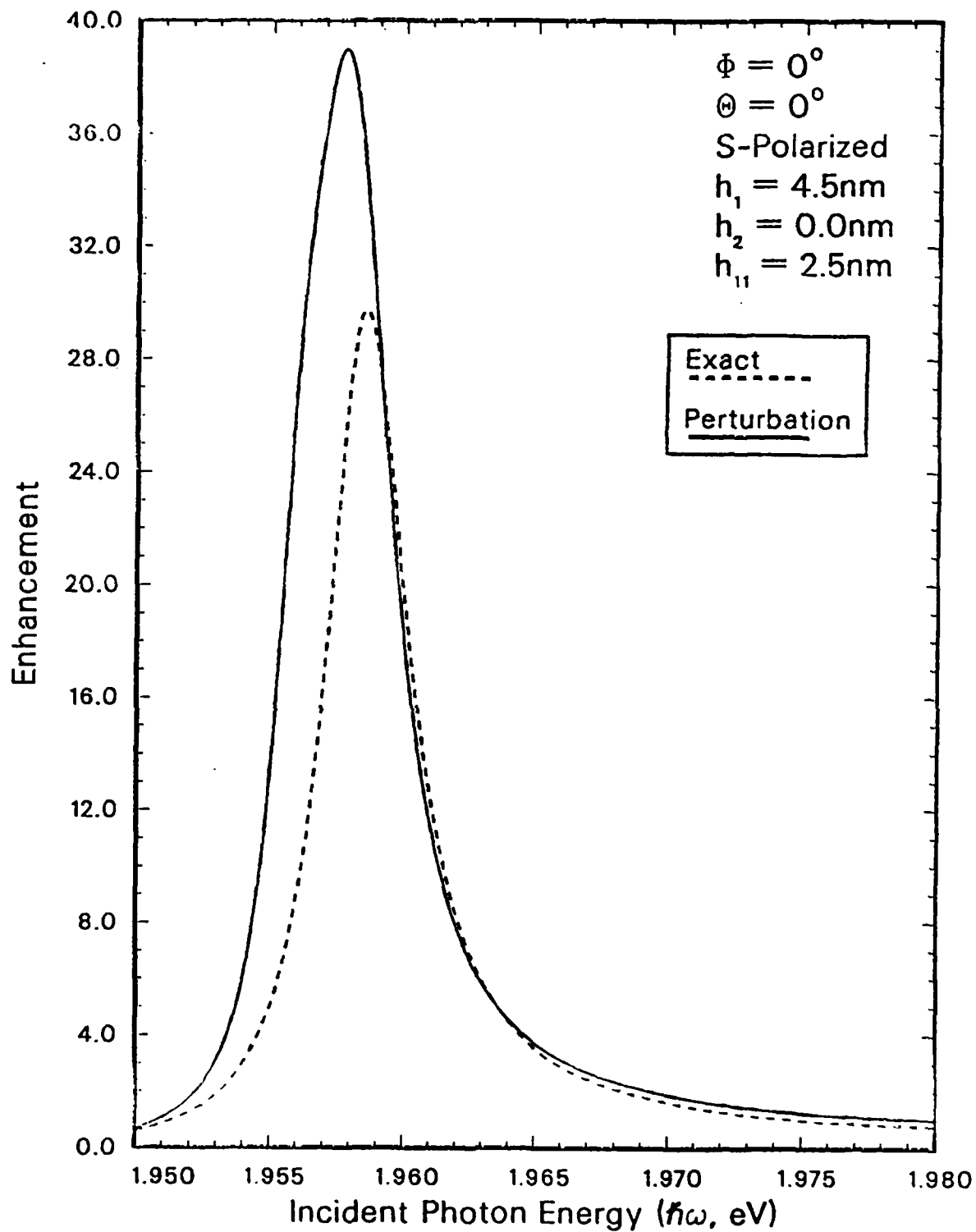


Figure 45. Enhancement Curves Versus Incident Photon Energy for S Polarization.

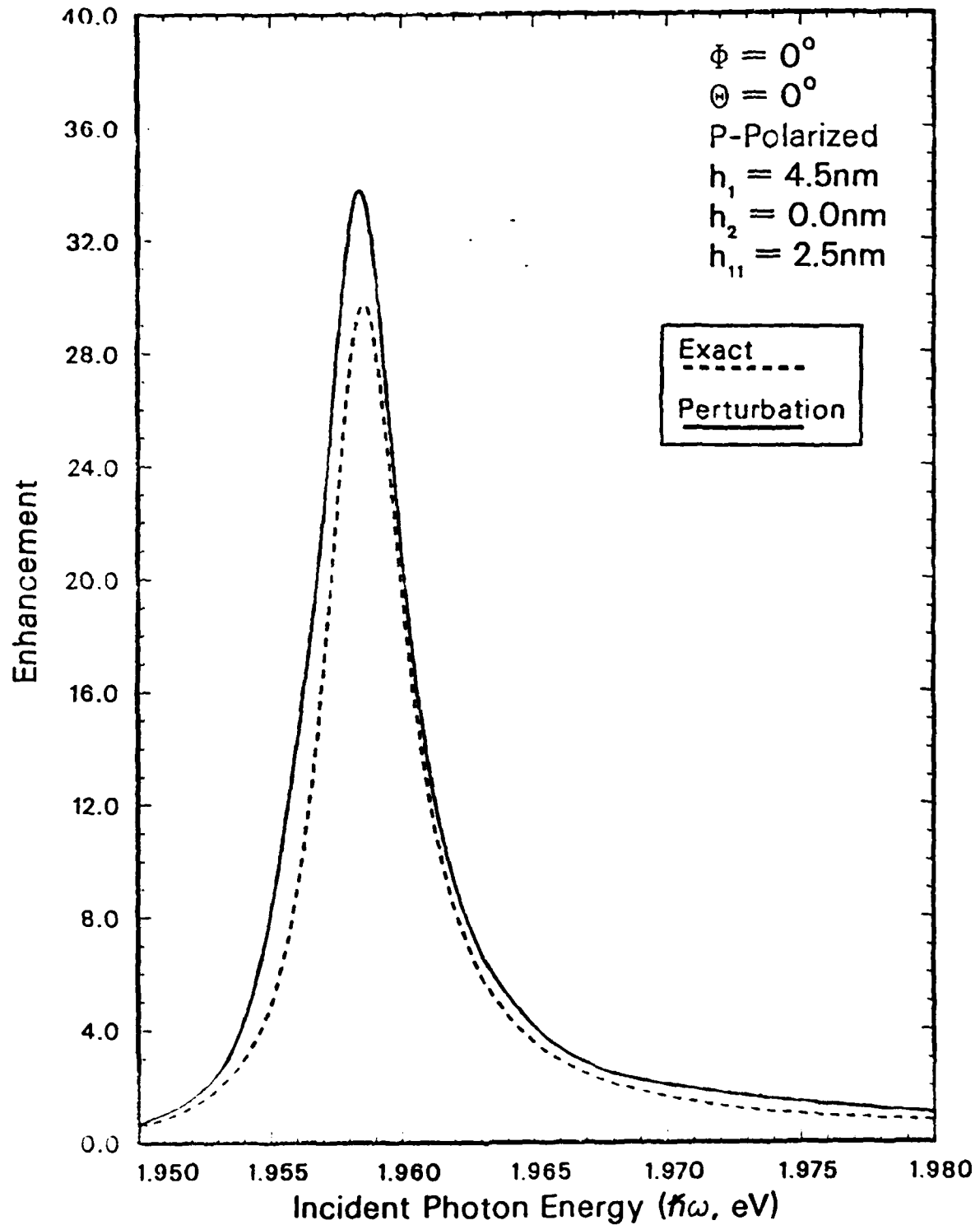


Figure 46. Enhancement Curves Versus Incident Photon Energy for P Polarization.

LIST OF REFERENCES

1. Maystre, D., "General Study of Grating Anomalies From Electromagnetic Surface Modes," in *Electromagnetic Surface Modes*, edited by A. D. Boardman, pp. 661-724, John Wiley and Sons Ltd., 1982.
2. Fano, U., "The Theory of Anomalous Diffraction Gratings and of Quasi-Stationary Waves on Metallic Surfaces (Sommerfeld's Waves)," *Journal of the Optical Society of America*, 31, pp. 213-222, March 1941.
3. Maystre, D. and Petit, R., "Brewster Incidence For Metallic Gratings," *Optics Communications*, 17.2, pp. 196-200, May 1976.
4. Hutley, M. C. and Maystre, D., "The Total Absorption Of Light By A Diffraction Grating," *Optics Communications*, 19.3, pp. 431-436, December 1976.
5. Glass, N. E., Maradudin, A. A. and Celli, V., "Theory of Surface Polariton Resonances and Field Enhancements in Light Scattering from Bigratings," *Journal of the Optical Society of America*, 73, pp. 1240-1248, October 1983.
6. Raether, H., "Surface Plasmons and Roughness," in *Surface Polaritons*, edited by V. M. Agranovich and D. L. Mills, pp. 331-403, North-Holland Publishing Co., 1982.
7. Boardman, A. D., "Hydrodynamic Theory of Plasmon Polaritons on Plane Surfaces," in *Electromagnetic Surface Modes*, edited by A. D. Boardman, pp. 1-76, John Wiley and Sons Ltd., 1982.
8. Maradudin, A. A., "Surface Waves," in *Festkörperprobleme XXI: Advances in Solid State Physics*, edited by J. Treusch, pp. 25-116, Friedrich Viewig und Sohn Verlagsgesellschaft, 1981.

9. Naval Postgraduate School Report NPS-61-87-003, A *Perturbation Theory for Light Diffraction from a Grating with Multiple Surface Polariton Excitation*, by N. E. Glass, 17 December 1986.
10. Smith, S. J. and Purcell, E. M., "Visible Light from Localized Surface Charges Moving Across a Grating," *Physical Review*, 92.4, p. 1069, 15 November 1953.
11. Kaplan, A. E. and Datta, S., "Extreme Ultraviolet and X-ray Emission and Amplification by Nonrelativistic Electron Beams Traversing a Superlattice," *Applied Physics Letters*, 44.7, pp. 661-663, 1 April 1984.
12. McPhedran, R. C., Derrick, G. H. and Botten, L. C., "Theory of Crossed Gratings," in *Electromagnetic Theory of Gratings*, edited by R. Petit, pp. 227-279, Springer-Verlag, 1980.
13. Petit, R., "A Tutorial Introduction," in *Electromagnetic Theory of Gratings*, edited by R. Petit, pp. 1-50, Springer-Verlag, 1980.
14. Kröger, E. and Kretschmann, E., "Surface Plasmon and Polariton Dispersion at Rough Boundaries," *Physica Status Solidi*, B76.2, pp. 515-532, 1 August 1976.
15. Toigo, F., Marvin, A., Celli, V., and Hill, N. R., "Optical Properties of Rough Surfaces: General Theory and the Small Roughness Limit," *Physical Review*, B15.12, pp. 5618-5626, 15 June 1977.
16. Mills, D. L., "Interaction of Surface Polaritons with Periodic Surface Structures; Rayleigh Waves and Gratings," *Physical Review*, B27, pp. 3097-3118, 15 March 1983.
17. Elson, J. M. and Sung, C. C., "Intrinsic and Roughness Induced Absorption of Electromagnetic Radiation Incident on Optical Surfaces," *Applied Optics*, 21.8, pp. 1496-1501, 15 April 1982.
18. Glass, N. E., Weber, M. and Mills, D. L., "Attenuation and Dispersion of Surface Polaritons on Gratings," *Physical Review*, B29.12, pp. 6548-6559, 15 June 1984.

19. Glass, N. E. and Maradudin, A. A., "Polariton Resonant Absorption in a Bigrating: Exact Theory Compared to Recent Experiments and to Perturbation Theory," *Optics Communications*, 56.5, pp. 339-344, 1 January 1986.
20. Inagaki, T., Goudonet, J. P., Little, J. W. and Arakawa, E. T., "Photoacoustic Study of Plasmon Resonance Absorption in a Bigrating," *Journal of the Optical Society of America*, B2.3, pp. 413-419, March 1985.
21. Glass, N. E., "Perturbation Theory for Light Diffraction with Surface Polariton Resonances on a Bigrating," *Physical Review*, B35.6, pp. 2647-2659, 15 February 1987.
22. Kittel, C., *Introduction to Solid State Physics*, 6th ed., John Wiley and Sons, Inc., 1986.
23. Nakajima, S., Toyozawa, Y. and Abe, R., *The Physics of Elementary Excitations*, Springer-Verlag, 1980.
24. Cracknell, A. P. and Wong, K. C., *The Fermi Surface*, Oxford University Press, 1973.
25. Maradudin, A. A., "Interaction of Surface Polaritons and Plasmons with Surface Roughness," in *Surface Polaritons*, edited by V. M. Agranovich and D. L. Mills, pp. 405-510, North-Holland Publishing Co., 1982.
26. Johnson, P. B. and Christy, R. W., "Optical Constants of the Noble Metals," *Physical Review*, B6.12, pp. 4370-4379, 15 December 1972.
27. Weber, M. G. and Mills, D. L., "Determination of Surface Polariton Minigaps on Grating Structures: A Comparison Between Constant Frequency and Constant Angle Scans," *Physical Review*, B34.4, pp. 2893-2894, 15 August 1986.
28. Vincent, P., "A Finite Difference Method for Dielectric and Conducting Crossed Gratings," *Optics Communications*, 26.3, pp. 293-296, September 1978.

INITIAL DISTRIBUTION LIST

	No. Copies
1. Defense Technical Information Center Cameron Station Alexandria, Virginia 22304-6145	2
2. Library, Code 0142 Naval Postgraduate School Monterey, California 93943-5002	2
3. Department Chairman, Code 61 Department of Physics Naval Postgraduate School Monterey, California 93943-5004	1
4. Prof. N. E. Glass, Code 61Gc Department of Physics Naval Postgraduate School Monterey, California 93943-5004	3
5. Prof. J. R. Neighbours, Code 61Nb Department of Physics Naval Postgraduate School Monterey, California 93943-5004	2
6. Officer in Charge White Oak Laboratory, Code U43 Naval Surface Weapons Center Detachment 10901 New Hampshire Avenue Silver Spring, Maryland 20903-5000	3

END

10-87

DTIC